



THE UNIVERSITY OF  
**WAIKATO**  
*Te Whare Wānanga o Waikato*

Research Commons

<http://waikato.researchgateway.ac.nz/>

## Research Commons at the University of Waikato

### Copyright Statement:

The digital copy of this thesis is protected by the Copyright Act 1994 (New Zealand).

The thesis may be consulted by you, provided you comply with the provisions of the Act and the following conditions of use:

- Any use you make of these documents or images must be for research or private study purposes only, and you may not make them available to any other person.
- Authors control the copyright of their thesis. You will recognise the author's right to be identified as the author of the thesis, and due acknowledgement will be made to the author where appropriate.
- You will obtain the author's permission before publishing any material from the thesis.









# CKNOWLEDGEMENTS

When this topic was first suggested to me it sounded great. Sunny summer days spent leisurely walking with nature. The thrill of knowing you are possibly the only person for miles all directions. Relaxing and enjoying the grand view from atop of the volcano. The locals even gave me tips on how best to access the slopes - how can you compete with that? Just collect some rocks, bring them back to the university and test them in the lab I thought, no problem. Then started the field work, along with surprising observations such as the incredibly dense native bush with which I was meant to 'leisurely' walk through, and understanding that the locals were not joking when they told me to run very fast and get up high when eluding wild pigs.

While my initial perceptions of the tasks at hand may have been a little misguided, my perceptions of the time and effort spent by others in assisting me with my project are definitely not. There are many people who have assisted and supported me during the course of this project and I would like to take this opportunity to try and thank them all.

Firstly, I would like to give my thanks to Graham Kahu Te Rire, Tom Cass, and the rest of the team at Maori Investments Limited for granting me permission to access Putauaki and carry out research. Without your assistance, this study would not have been possible. Putauaki is a truly wonderful mountain in a splendid environment and I hope dearly to return in the near future and continue my explorations of the volcano.

I would also like to thank my chief supervisor, Dr. Vicki Moon. Thank you for providing an endless supply of your expert knowledge, advice and time during this project. Your assistance and encouragement has been greatly appreciated. Also, thank you to Dr. Richard Smith, not only for your interpretations of volcanic facies, but also for your advice when I was initially deciding upon a research topic.

To the rest of the academic staff of the Department of earth and ocean sciences who have guided me in getting to this stage, I say thank you for putting up with me. Your knowledge and advice was given generously when I required it. To the Technical and administrative staff of the Department of Earth and Ocean Sciences, you always seemed to rapidly find the right solution to my numerous technical problems.

Financial assistance was gratefully received through a University of Waikato Masters Research Scholarship. Without its support, my research definitely could not have run as smoothly as it did.

Thank you to my family for all your support, and thank you for listening to my very long winded geological explanations for things, even if you were only being polite. Thank you also to all my friends and fellow students. It has been a memorable journey and cannot think of a better group of people with whom I would have wanted to travel it with.

Finally I would like to show my appreciation to you Lauren, for your words of support and your understanding of the time I spent on this project. I hope that I can be as supportive for you as you have been for me in your upcoming year of study. I wish you good luck.

# *TABLE OF CONTENTS*

---

Abstract	ii
Preface	iv
Acknowledgements	v
Table of contents	vii
List of figures	xiii
List of tables	xvii

## **CHAPTER ONE - INTRODUCTION**

1.1	Introduction	1
1.2	Thesis aims and objectives	1
1.3	Geological setting of Putauaki	2
1.4	Study area	3
1.5	Study outline	4

## **CHAPTER TWO - LITERATURE REVIEW**

2.1	Introduction	6
2.2	Landslides in volcanic settings	6
2.2.1	Terminology	6
2.2.2	Event frequency	7
2.2.3	Source areas	7
2.2.4	Deposit morphology	8
2.3	Factors contributing to volcanic landslides	9
2.3.1	Overview	9
2.3.2	Hydrothermal alteration	9
2.3.3	Magmatic intrusions	10
2.3.4	Elevated pore-water pressures	10
2.3.5	Destabilising layers	11
2.3.6	Cone morphology	11
2.3.7	Multiple factors	13
2.4	Geotechnical classification of volcanoes	14

2.4.1	Rock mass classification	14
2.4.1.1	Rock Quality Designation	15
2.4.1.2	Rock Mass Rating	16
2.4.1.3	Geological Strength Index	16
2.4.2	Organising data for stability modelling	19
2.4.2.1	Hoek-Brown strength parameters	19
2.4.3	Stability modelling	21
2.5	Summary	23

### CHAPTER THREE - METHODOLOGY

3.1	Introduction	24
3.2	Geomorphology	24
3.2.1	Geographical information systems (GIS)	24
3.2.2	Topographical profiles	25
3.2.3	Geomorphic description	25
3.3	Rock mass description	26
3.3.1	Rock mass strength of hard rocks	27
3.3.1.1	Schmidt hammer	28
3.3.1.2	Discontinuities	28
3.3.1.2.1	Scanline surveys	29
3.3.1.2.2	Discontinuity spacing	29
3.3.1.2.3	Discontinuity orientation	30
3.3.1.2.4	Discontinuity infill	30
3.3.1.2.5	Discontinuity persistence	31
3.3.1.2.6	Discontinuity roughness	32
3.3.1.2.7	Discontinuity seepage	32
3.3.1.3	Sampling	33
3.3.2	Rock mass strength of soft rocks	33
3.3.2.1	Sampling	34
3.3.3	Rock mass classification	35
3.4	Laboratory work: hard rocks	36
3.4.1	Bulk density and porosity	36
3.4.2	Point load test	36
3.4.3	Discontinuity orientation	37

---

3.4.4	RocLab™	37
3.5	Laboratory work: soft rocks	38
3.5.1	Bulk density	38
3.5.2	Direct shear strength test	38
3.5.2.1	Preparation of the sample	38
3.5.2.2	Magnitude of normal load	39
3.5.2.3	Calculating cohesion and friction angle	39
3.6	Summary	40

#### CHAPTER FOUR - GEOMORPHOLOGY AND GEOLOGY

4.1	Introduction	41
4.2	Geomorphology	41
4.3	Rock mass description	44
4.3.1	Rock mass description of hard rocks	47
4.3.1.1	Indurated andesite	48
4.3.1.2	Scoriaceous andesite	50
4.3.1.3	Altered andesite	52
4.3.1.4	Indurated dacite	54
4.3.2	Rock mass description of soft rocks	55
4.3.2.1	Block and ash flow	56
4.3.2.2	Matahina Ignimbrite	57
4.4	Distribution of lithotechnical units	59
4.5	Summary	60

#### CHAPTER FIVE - GEOTECHNICAL PROPERTIES

5.1	Introduction	62
5.2	Hard rocks	62
5.2.1	Unit weight and porosity	62
5.2.2	Intact strength	63
5.2.2.1	Schmidt hammer	63
5.2.2.2	Uniaxial compressive strength	64
5.2.3	Discontinuities	65
5.2.3.1	Discontinuity orientation	65

5.2.3.2	Discontinuity spacing and Rock Quality	
	Designation	66
5.2.3.3	Discontinuity condition	67
5.2.3.4	Discontinuity infill	68
5.2.3.5	Discontinuity seepage	68
5.2.4	Rock Mass Rating and Geological Strength Index	68
5.2.5	Hoek-Brown strength parameters	71
5.2.5.1	Selection of parameters PLCN, $m_i$ and D	72
5.3	Soft rocks	75
5.3.1	Unit weight	75
5.3.2	Intact strength	76
5.3.2.1	Block and ash flow	76
5.3.2.2	Matahina Ignimbrite	78
5.4	Summary	79

## CHAPTER SIX – GALENA™ MODELLING

6.1	Introduction	81
6.2	Galena™	81
6.3	Model definition	81
6.3.1	Material properties	82
6.3.2	Slope surface	82
6.3.3	Material profiles	82
6.3.4	Phreatic surface	83
6.3.5	Factor of safety	84
6.3.6	Failure surface	85
6.3.7	Analysis method	87
6.4	Model construction	87
6.4.1	Slope profiles	87
6.4.2	Stratigraphy	89
6.4.3	Watertable	93
6.4.4	Sensitivity analysis	94
6.4.4.1	Earthquake forces	95
6.4.4.2	Watertable elevation	95
6.4.4.3	Disturbance factor	96

6.4.5	A possible 8,470 combinations	97
6.5	Stability of slope profiles	97
6.5.1	Small scale failures	99
6.5.2	Large scale failures	102
6.5.2.1	Conditions of failure graphs	102
6.5.2.2	Profiles showing realistic conditions of failure	109
6.5.2.3	Profiles showing unrealistic conditions of failure	112
6.6	Summary and conclusions	115
<b>CHAPTER SEVEN – RISK ANALYSIS</b>		
7.1	Introduction	118
7.2	Geomorphology and geology	118
7.3	Geotechnical properties	119
7.4	Galena™ modelling	120
7.5	Risk analysis	122
7.5.1	Estimation of landslide run-out distance	122
7.5.1.1	Selection of H/L ratio	123
7.5.1.2	Topographical effects on landslide run-out	127
7.5.2	Estimation of landslide run-out depth	131
7.5.3	Risk analysis	132
7.5.3.1	South-western run-out zone: profile 6	132
7.5.3.2	Eastern run-out zones: profiles 4a, 5a and 6	134
7.5.3.3	North-western run-out zones: profiles 4 and 5	137
7.6	Summary	139
<b>REFERENCES</b>		143
<b>APPENDICES</b> (located on accompanying compact disc)		
Appendix A	Guidelines for measurement of hard rock mass strength	
Appendix B	Scanline survey outline	

Appendix C	Guidelines for measurement of soft rock mass strength
Appendix D	Method for calculating uncorrected and corrected point load strength
Appendix E	Method for calculating the magnitude of normal stress for direct shear tests
Appendix F	Rock mass descriptions of hard and soft rocks
Appendix G	Unit weight and porosity data
Appendix H	Schmidt hammer data
Appendix I	Point load data
Appendix J	Scanline survey datasheets
Appendix K	Stereonets and discontinuity spacing
Appendix L	Calculation of RQD ratings
Appendix M	Calculation of RMR parameters
Appendix N	Calculation of GSI parameters
Appendix O	Combinations of PLCN, $m_i$ and D and associated $c$ and $\phi$
Appendix P	Direct shear data for the soft rocks
Appendix Q	x/y co-ordinate pairs for each slope profile
Appendix R	Combinations of earthquake force, watertable elevation and D, and resulting F values

# *LIST OF FIGURES*

---

Figure 1.1	Tectonic setting of Putauaki.	3
Figure 1.2	Digital elevation model indicating approximate location of study area.	4
Figure 2.1	Cross-sections of volcanic landslides as compared to non-volcanic landslides.	8
Figure 2.2	Schematic illustrating the direction of proposed dilational stresses associated with the intrusion of dykes within the volcano edifice.	11
Figure 2.3	Schematic illustrating shear stress distribution in relation to morphological changes on the volcano flanks.	12
Figure 2.4	Slope angle of Quaternary volcanoes that have undergone major slope failure.	12
Figure 2.5	Factors contributing to the inherent instability of volcanoes.	13
Figure 2.6	The RMR system or Geomechanics Classification.	17
Figure 2.7	The modified GSI classification scheme.	18
Figure 2.8	Modelled failure of a volcanic cone using a two dimensional distinct element model.	22
Figure 3.1	DEM indicating location of rock mass strength measurements.	27
Figure 3.2	Schematic diagram of a scanline survey.	29
Figure 3.3	Schematic illustrating dip and dip direction of a discontinuity.	31
Figure 3.4	Schematic of a profile gauge and associated discontinuity roughness grades.	32
Figure 3.5	Grain sizes associated with coarse and fine soils.	34
Figure 4.1	Major geomorphological features of Putauaki and the surrounding landscape.	42
Figure 4.2	Putauaki viewed from the north-west.	43

Figure 4.3	DEM showing location of rock mass description sites.	45
Figure 4.4	Schematic illustrating inferred stratigraphy and ages of lithotechnical units identified on Putauaki.	46
Figure 4.5	Indurated andesite outcrop exhibiting a scoriaceous surface structure that is absent deeper within the rock mass.	49
Figure 4.6	Indurated andesite outcrop exhibiting wide discontinuity spacing.	50
Figure 4.7	Scoriaceous andesite outcrop exhibiting a scoriaceous nature.	51
Figure 4.8	Discontinuity sets in the scoriaceous andesite.	52
Figure 4.9	A tomo in the scoriaceous andesite.	53
Figure 4.10	Altered andesite outcrop exhibiting a readily disaggregated nature.	54
Figure 4.11	Light grey colour characteristic of the indurated dacite.	55
Figure 4.12	Indurated dacite outcrop exhibiting very wide discontinuity apertures.	55
Figure 4.13	Block and ash flow deposit.	57
Figure 4.14	Matahina Ignimbrite outcrop.	58
Figure 4.15	DEM indicating location and approximate boundaries of each lithotechnical unit.	59
Figure 5.1	Graph showing the effect of changing PLCN, $m_i$ and $D$ , on $c$ and $\phi$ for the indurated andesite.	73
Figure 5.2	Graph of peak shear stress versus normal stress for the block and ash flow.	77
Figure 5.3	Graph of peak shear stress versus normal stress for the Matahina Ignimbrite.	78
Figure 6.1	Galena™ model of slope profile 4 illustrating the right handed x/y co-ordinate system.	83
Figure 6.2	Schematic illustrating the Dupuit approximation for estimating the form of an asymmetrical watertable.	85

Figure 6.3	Schematic illustrating how Galena™ models failure surfaces using x-left, x-right and radius parameters.	86
Figure 6.4	DEM indicating location of run-lines.	88
Figure 6.5	Schematic illustrating the division of run-lines into slope profiles.	89
Figure 6.6	DEM indicating location of run-lines relative to the boundaries of each lithotechnical unit.	90
Figure 6.7a	Galena™ models of slope profiles 2, 2a, 3 and 3a showing subsurface stratigraphy.	91
Figure 6.7b	Galena™ models of slope profiles 4, 4a, 5 and 5a showing subsurface stratigraphy.	92
Figure 6.7c	Galena™ models of slope profiles 6 and 6a showing subsurface stratigraphy.	93
Figure 6.8	Location of $H_1$ and $H_2$ parameters for each slope profile.	94
Figure 6.9	Realistic watertable elevation for Putauaki.	97
Figure 6.10	Calculation of the segment area of $F_{min}$ .	98
Figure 6.11	Galena™ models of slope profiles 2, 2a, 3, and 3a showing position of $F_{min}$ .	101
Figure 6.12a	Galena™ models of slope profiles 4 and 4a showing position of $F_{min}$ .	102
Figure 6.12b	Galena™ models of slope profiles 5, 5a, 6, and 6a showing position of $F_{min}$ .	103
Figure 6.13	Graphs of $F$ against watertable elevation at various earthquake forces ranging from 0.0 – 0.4 g.	105
Figure 6.14a	Conditions of failure graphs for profiles 4, 4a, and 5.	107
Figure 6.14b	Conditions of failure graphs for profiles 5a, 6 and 6a.	108
Figure 6.15	Galena™ model of profile 4a indicating a 12 % watertable elevation.	111

---

Figure 6.16	Galena™ model of profile 6a indicating a 25 % watertable elevation.	113
Figure 6.17	Profile of run-line 6 – 6a with watertable heights ranging from 30 – 90 %.	114
Figure 7.1	Schematic representation of the procedure used to calculate the H/L ratio of a potential landslide.	123
Figure 7.2	Log-log relationship between ratio of fall height and travel distance to volume of debris-avalanche deposits.	124
Figure 7.3	Volume of prefailure edifice compared to collapse volume.	126
Figure 7.4	DEM illustrating predicted maximum and minimum run-out distances of landslides sourced from each slope profile.	128
Figure 7.5	Schematic representation of the procedure used to position landslide run-out zones.	130
Figure 7.6	DEM illustrating predicted maximum and minimum run-out zones of landslides sourced from each slope profile.	131
Figure 7.7	DEM illustrating maximum and minimum run-out zones sourced from profile 6a.	133
Figure 7.8	DEM illustrating maximum and minimum run-out zones sourced from profiles 4a, 5a and 6.	136
Figure 7.9	DEM illustrating maximum and minimum run-out zones sourced from profiles 4 and 5.	137
Figure 7.10	Landslide risk zonation map for Putauaki.	142

# *LIST OF TABLES*

---

Table 3.1	Terms describing discontinuity spacing	30
Table 3.2	Terms describing discontinuity persistence	31
Table 3.3	Terms describing seepage	33
Table 4.1	Rock mass characteristics of hard rock lithotechnical units	47
Table 4.2	Rock mass characteristics of soft rock lithotechnical units	56
Table 4.3	Typical rock mass characteristics for each lithotechnical unit	61
Table 5.1	Unit weight and porosity of the hard rock units	63
Table 5.2	UCS values of the hard rock units calculated from average $r$ values	63
Table 5.3	UCS of the hard rock units calculated from average $I_{s50}$ assuming PLCN of 20 and 25	64
Table 5.4	Orientations of major discontinuity sets for hard rock units	66
Table 5.5	Discontinuity spacing and RQD ratings for hard rock units	67
Table 5.6	RMR values for the hard rock units	69
Table 5.7	GSI ratings for the hard rock units	71
Table 5.8	Input values selected for this study to estimate strength parameters for the hard rock units	75
Table 5.9	Unit weight of the soft rock masses	75
Table 5.10	Comparison of measured geotechnical data for the block and ash flow with published geotechnical data for similar deposits	77
Table 5.11	Comparison of measured geotechnical data for the Matahina Ignimbrite with published geotechnical data for similar deposits	79
Table 5.12	Final geotechnical properties for the hard and soft rock units	80

---

Table 6.1	Chord length, segment height and approximate area of $F_{\min}$ for slope profiles showing small and large scale failure	99
Table 6.2	Critical earthquake force required to produce an $F = 1.0$ for profiles 4, 4a, 5, 5a, and 6 at varying levels of D	110
Table 6.3	Critical earthquake force required to produce an $F = 1.0$ for profile 6a at varying levels of D	112
Table 6.4	Conditions promoting failure for slope profiles showing potential for large scale failure	117
Table 7.1	Approximate area, chord length, maximum width and maximum volume of $F_{\min}$ for slope profiles 4, 4a, 5, 5a, and 6	125
Table 7.2	H/L estimates of maximum and minimum run-out of landslides sourced from each slope profile	127
Table 7.3	Estimated depths of landslide deposits sourced from each slope profile	132
Table 7.4	Summary of landslide risk categorisation for each slope profile	140

# CHAPTER 1

# *INTRODUCTION*

---

## **1.1 INTRODUCTION**

It is well recognised that the collapse of stratovolcanoes (cone volcanoes) is a common phenomenon with many examples being identified in recent international literature (Voight & Elsworth 1997; van Wyk de Vries *et al.* 2000; Siebert 2002). However, while a number of volcanoes of this type are nationally very familiar (for example Mountains Taranaki, Ngauruhoe, and Ruapehu), limited research on the stability of these features has been undertaken to date in New Zealand. Putauaki (Mount Edgecumbe) is a cone volcano located onshore in the Bay of Plenty, New Zealand. The steep slope angles characteristic of Putauaki and its location within the active volcanic front on the eastern boundary of the Taupo Volcanic Zone (TVZ) are essential prerequisites for volcanic collapse. This study considers the stability of Putauaki and how failure of the volcanic edifice may impact upon fringing towns and industrial facilities.

## **1.2 THESIS AIMS AND OBJECTIVES**

The aim of this thesis is to assess the stability of Putauaki and analyse the risk associated with collapse of the volcanic edifice. Objectives to achieve this aim are:

- 1) to construct a geomorphic and geological map of Putauaki establishing structure and field geotechnical properties of individual lithotechnical units;
- 2) to determine the geotechnical properties of each lithotechnical unit identified using field and laboratory strength tests;
- 3) to produce stability models of Putauaki determining likelihoods of collapse; and

- 4) based on the mapping and modelling above, analyse the risk posed to surrounding communities associated with collapse of Putauaki.

### **1.3 GEOLOGICAL SETTING OF PUTAUAKI**

New Zealand sits astride the convergent margin of the Pacific and Australian Plates (Figure 1.1). Subduction of the Pacific Plate beneath the Australian Plate occurs at the Hikurangi Trough lying east of the North Island. Onshore evidence of the subduction is in the form of the TVZ; a 300 km long, north-east trending zone containing the main focus of young, active volcanism in New Zealand (Wilson *et al.* 1995) (Figure 1.1). The TVZ reaches from Ohakune in the south, extending offshore of the Bay of Plenty coast to the Whakatane seamount north of White Island (Cole 1990; Gamble 1993; Gamble & Wright 1995). While the eastern margin of the TVZ is well defined by a line of volcanoes extending from Mountains Ruapehu, through Tauhara, Putauaki, and White Island, the western boundary, largely buried by ignimbrites, is generally defined by caldera margins (Wilson *et al.* 1995) (Figure. 1.1).

Active rifting and crustal thinning in the northern part of the onshore TVZ has resulted in formation of the Whakatane Graben; a 20 km wide linear depression trending north-east from the Okataina Volcanic Centre to the Bay of Plenty coast (Beanland 1995; Nairn 1995) (Figure 1.1). The Whakatane Graben is a complex depression bounded to the north-west by normal faults while bounded to the south-east by intersecting north trending transcurrent faults and north-east trending normal faults (Duncan 1970). The Whakatane Graben dominates the structure of the Bay of Plenty.

Evidence from drill holes indicate that over the last 1 Ma the Whakatane Graben has been infilled with volcanogenic sediment - ignimbrite sequences derived mostly from the Okataina Volcanic Centre to the south (Duncan 1970). These volcanogenic sediment - ignimbrite sequences overlie indurated greywacke basement rocks at a depth of about 1 km (Nairn 1995). On the south-east flank of the Whakatane Graben, rhyolitic and andesitic lava flows and domes are interbedded within the sediment - ignimbrite sequence suggesting a significant, if relatively small, volcanic centre has been intermittently active during the last

several thousand years (Duncan 1970). Putauaki, overlooking Kawerau Township 2 km to the north-west, is the product of the most recent activity within the Whakatane Graben (Nairn 1995) (Figure 1.1).

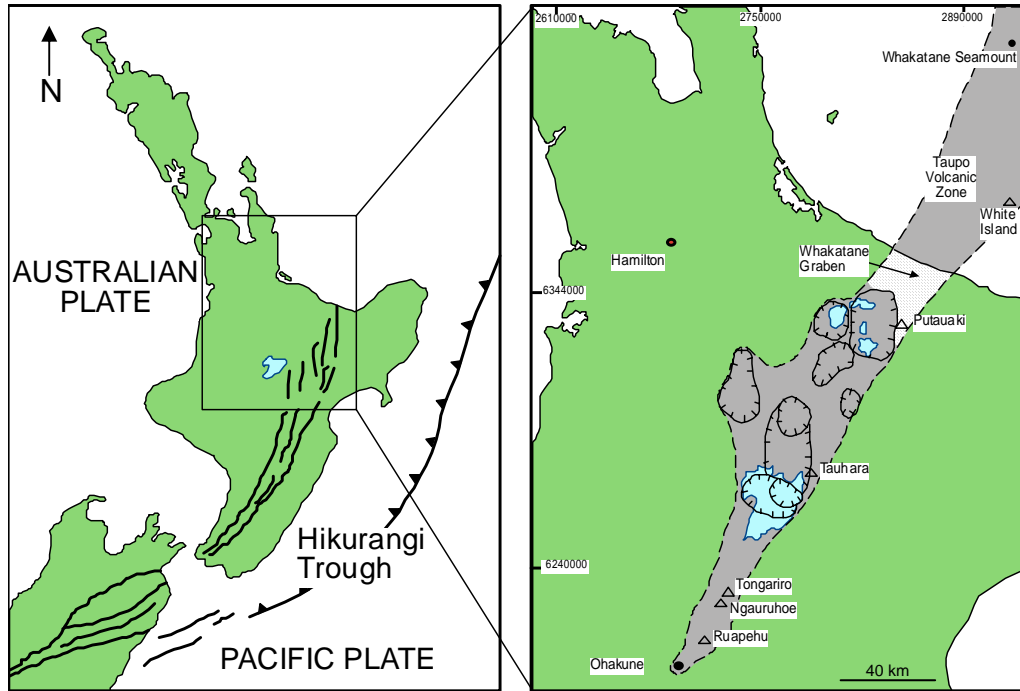
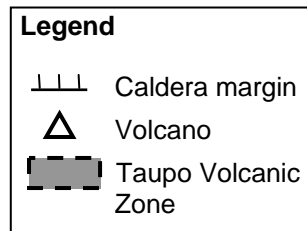


Figure 1.1 – Tectonic setting of Putauaki. Adapted from Nairn (1995).



### 1.4 STUDY AREA

The aim of this study is to analyse the risk posed by volcanic collapse from Putauaki. Clearly Putauaki will act as a locator for the study area. However, the scale to which volcanic collapse may impact upon the surrounding landscape is at this stage unknown, meaning the study area boundaries shown in Figure 1.2 are only approximate.

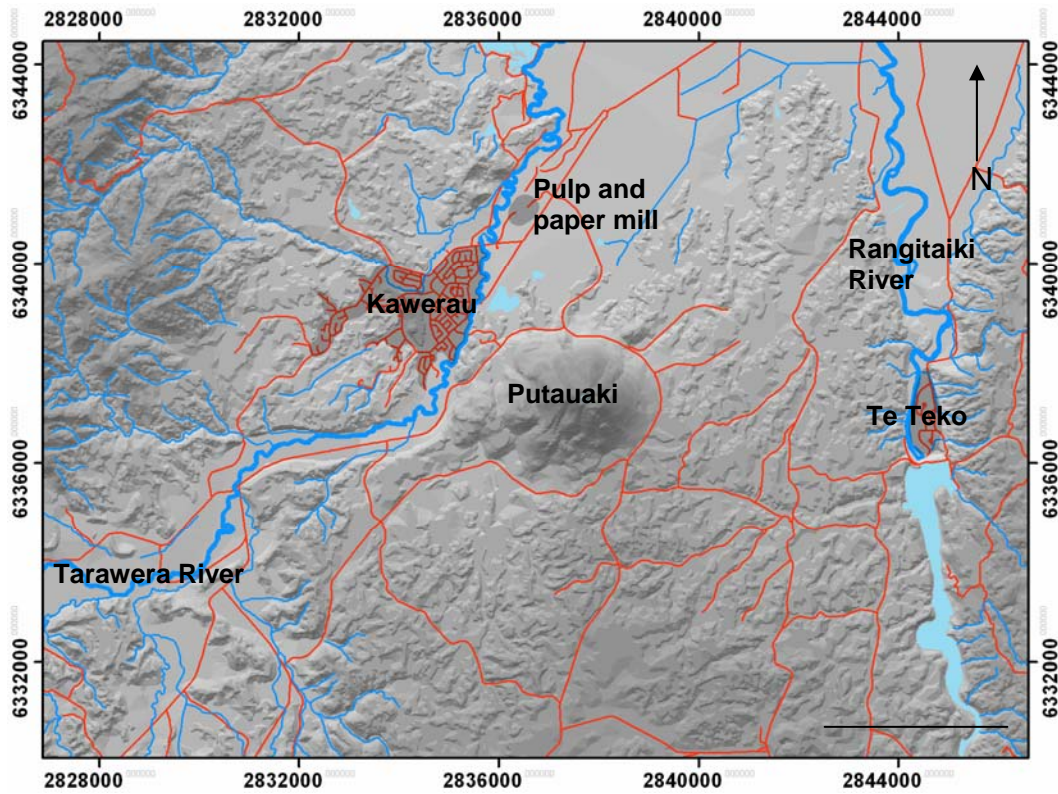
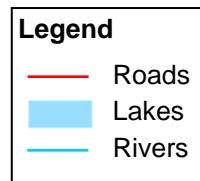


Figure 1.2 – Digital elevation model indicating approximate location of study area. Black line represents 4 km.



## 1.5 STUDY OUTLINE

This chapter presents a general introduction outlining aims and objectives of the study, and providing a geological setting of the study area. This is followed in Chapter 2 by a literature review discussing landslides in volcanic settings and their potential causes, geotechnical classification of volcanoes using rock mass classification methods and rock mass strength criteria, and stability analysis methods applied to volcanoes. Chapter 3 covers the methodology of the study including field data collection and laboratory testing. Chapter 4 describes how geomorphic mapping and measurement of rock mass strength parameters provides the foundations for the geotechnical characterisation of lithotechnical units present within the study area. Chapter 5 presents the results of field and laboratory strength measurements for each lithotechnical unit. Strength and stratigraphical

data compiled in the field and laboratory are then used to construct Galena™ slope stability models which are used to assess the sensitivity of the slopes to factors such as earthquake forces and watertable elevation (Chapter 6). Chapter 7 draws conclusions on the findings of the thesis aims and objectives, including the final aim of analysing the risk associated with flank failure from Putauaki.

## CHAPTER 2

# *LITERATURE REVIEW*

---

### **2.1 INTRODUCTION**

Unlike ordinary mountains, formed by slow uplift and erosion, volcanoes are constructed relatively rapidly. As a consequence of this ‘rapid’ construction, many volcanic edifices are unstable and liable to collapse, producing volcanic landslides. The aim of this literature review is to outline aspects important in the assessment of volcano instability. It will be divided into three sections. Section 2.2 will address volcanic landslide frequency and source area morphology, Section 2.3 defines factors which may contribute to the initiation of volcanic landslides and Section 2.4 discusses geotechnical classification of volcanoes highlighting the importance of rock mass classification schemes and preparation of data for stability modelling. In conclusion, various methods of volcano stability modelling will be examined.

### **2.2 LANDSLIDES IN VOLCANIC SETTINGS**

#### **2.2.1 TERMINOLOGY**

A complex terminology for volcanic mass movements has evolved over the years. An abbreviated list is given in Siebert (2002) and includes rockslide avalanche, rockfall avalanche, rock avalanche, debris avalanche, debris flow and sturzstrom. Although volcanic mass movements initiate as a sliding movement, flow soon dominates, reflecting the two most commonly used terms in a volcanological context, debris avalanche and debris flow. While the latter refers to water-saturated mass movements (Smith & Lowe 1991; Iverson *et al.* 1997; Capra *et al.* 2002), debris avalanches portray a variable water content from largely dry to containing sufficient water to cause transformation into debris flows (Siebert 2002). The reader should note that the forthcoming study will employ the term volcanic landslide to refer to all volcanic mass movements.

### **2.2.2 EVENT FREQUENCY**

Structural collapse producing volcanic landslides was once thought to occur only once or twice during the life cycle of a volcano, but studies have demonstrated repetitive occurrence at some volcanoes – up to seven times at Mauna Loa, Hawaii (Moore *et al.* 1994), eight at Mount Taranaki, New Zealand (Palmer *et al.* 1991), and more than ten times at Augustine, Alaska (Begét & Kienle 1992). In fact, in a well-studied region such as Japan, volcanic landslides have been documented at more than 40% of volcanoes (Siebert 2002). Seventeen avalanche calderas are known or inferred to have formed in the last 400 years; a global frequency of roughly four per century (Siebert 1996). Simkin & Siebert (1994) listed volcanic landslide deposits for more than 350 Quaternary volcanoes, including more than 1 out of 6 of the world's Holocene volcanoes.

Due to the incomplete nature of the early historic record, post collapse eruptions concealing evidence of landslides, and the fact that many volcanoes have yet to be investigated in sufficient detail, these figures could be viewed as minima.

### **2.2.3 SOURCE AREAS**

The failure surfaces of volcanic landslides are typically more deeply seated than their non-volcanic counterparts and not as influenced by stratigraphic dip slopes (Figure. 2.1). Their greater depth may be attributed in part to the presence of large amounts of weakly indurated pyroclastic and altered material (Reid *et al.* 2000; Siebert 2002). Smaller-volume volcanic landslides without associated eruptions, for example Yasour Volcano, southwest Pacific, 1975, tend to form shallow depressions on the flanks of volcanoes. This is in contrast to the large amphitheatres of large volume volcanic landslides which often extend into the core of the volcano and contain the central vent (Siebert 1984).

Volcano morphology varies widely and as a result so too do failure scarps; in plan view ranging from  $< 15 - 120^\circ$  of the edifice (Francis & Wells 1988; De Silva *et al.* 1993), the widths perpendicular to the breached direction ranging from  $< 1 - > 10$  km (Siebert 1996). Steep sided andesitic and dacitic stratovolcanoes, attaining a relief of several kilometres and upper slopes exceeding  $30^\circ$ , are obvious candidates for slope failure (Francis & Wells 1988). Nevertheless,

providing a suitable mechanism exists, low angle shield volcanoes have also undergone collapse for example Oahu and Molokai, Hawaii (Vallance *et al.* 1995).

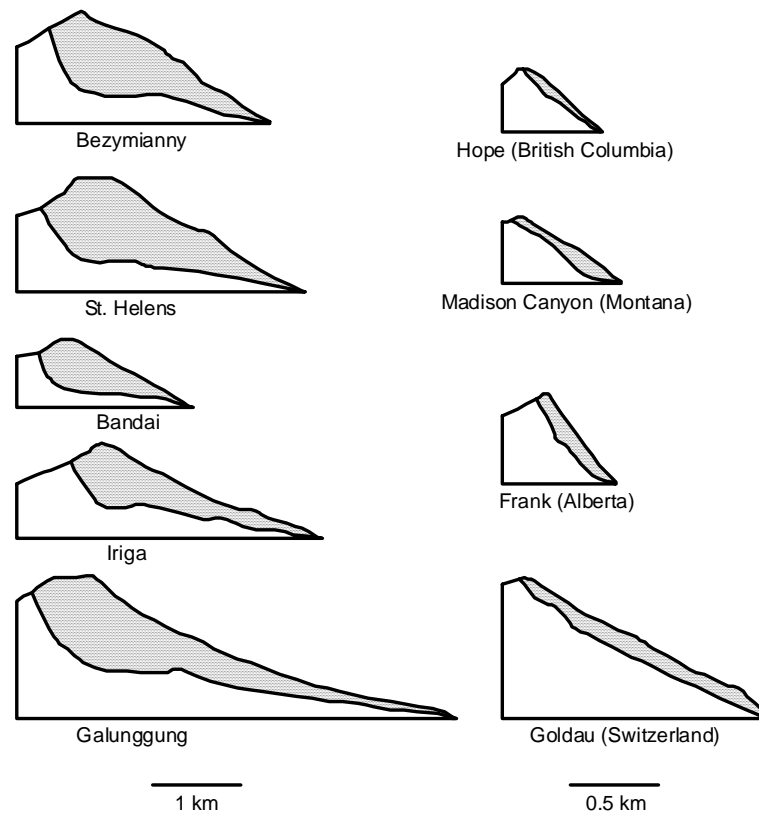


Figure 2.1 – Cross-sections of volcanic landslides (left column) as compared to non-volcanic landslides (right column, drawn at 2x scale). Shaded portion indicates volume removed by slope failure. Vertical scale equals horizontal scale. Adapted from Siebert (1999)

#### 2.2.4 DEPOSIT MORPHOLOGY

Perhaps the most distinctive feature of volcanic landslide deposits is the surface morphology commonly characterised by regions of hummocky terrain with numerous small (several metres to hundreds of metres in length) hills and closed depressions (Moore *et al.* 1994; Siebert 2002). Long radial ridges may predominate in some deposits, the long axis in many cases paralleling flow direction (Siebert 1984; Siebert 2002). Surface drainage is often irregular or discontinuous and small lakes or ponds may form in depressions (Siebert 1996). While portions of some debris avalanche deposits contain hundreds to thousands

of closely spaced hummocks, examples where hummocky morphology is largely subdued or absent are reported (Francis & Wells 1988).

## **2.3 FACTORS CONTRIBUTING TO VOLCANIC LANDSLIDES**

### **2.3.1 OVERVIEW**

Volcanoes can be thought of as transient accumulations of unstable material on regional bedrock. Gravitational adjustments lead to slow settling of the entire volcanic cone; however, segments of volcanoes can break off and slide down-slope. While the last two decades have shown advances in understanding the causes of large volcanic landslides, a comprehensive analysis of the causes remains in its infancy. Important factors in the inherent instability of volcanoes include:

- 1) extensive hydrothermal alteration;
- 2) magmatic intrusions,
- 3) elevated pore-water conditions and seismicity;
- 4) the presence of potential weak ‘destabilising layers’; and
- 5) cone morphology.

Sections 2.3.2 – 2.3.6 will discuss each of these factors in more detail.

### **2.3.2 HYDROTHERMAL ALTERATION**

Hydrothermal systems exist at many volcanoes where buried intrusives interact with groundwater producing highly acidic hot fluids which promote rock dissolution and clay mineral formation along geologic structures (discontinuities, faults and dykes) and lithologic boundaries (López & Williams 1993; Watters *et al.* 2000). This process allows strong rock to be generally replaced by weaker, clay-rich rock that, if unfavorably oriented with regard to slope stability, may provide potential sliding planes or release surfaces producing a mechanically unstable edifice (Vallance 1999; van Wyk de Vries *et al.* 2000; Watters *et al.* 2000). However, not all types of hydrothermal alteration result in lowered rock mass strengths. Silicification for example generally produces a stronger and more elastic rock mass (Watters *et al.* 2000). While it is difficult to assess the specifics

of hydrothermally altered rock masses, a strength decrease is a good first approximation (López & Williams 1993; Watters *et al.* 2000).

As the occurrence of volcanic hydrothermal systems can extend long after magmatic addition to the edifice has ceased (Davidson & De Silva 2000), collapses related to hydrothermal alteration can pose a significant risk even at inactive volcanoes.

### **2.3.3 MAGMATIC INTRUSIONS**

Magmatic intrusions correlate with deformation of the edifice, suggesting that intrusion is more forceful than passive. Voight & Elsworth (1997) propose that intruding dykes may have a dilational effect on volcanoes, presumably fracturing and weakening the edifice promoting collapse in a direction perpendicular to that of intrusion orientation (Figure 2.2). Particularly susceptible to failure as a result of forceful magmatic intrusion are steep sided, less voluminous lava-dome complexes which may become oversteepened (Siebert 1996).

Earthquakes are inferred to play a significant role in the initiation of large volcanic landslides. Pre-failure seismicity is commonly related to stresses induced by forceful magma intrusion, as well as regional tectonic earthquakes, explaining the the number of volcanic landslides occurring on volcanoes located within subduction margins (west coast of United States of America; Colima Volcanic Complex, Mexico; Mount Taranaki, New Zealand) (Voight & Elsworth 1997). It is not difficult to understand the detrimental effects that dynamic seismic vibrations may have on the stability of a volcanic edifice.

### **2.3.4 ELEVATED PORE-WATER PRESSURES**

Elevated pore-water pressures affect rock frictional resistance, essentially lowering the strength of rock masses. Magmatic intrusions are a commonly accepted means for creating elevated pore-water pressures in portions of the edifice (Elsworth & Voight 1995; Voight & Elsworth 1997). Alternatively, the resulting increase in permeability of hydrothermally altered rock masses may be responsible for elevated pore-water pressures (Day 1996; Cecchi *et al.* 2005). Hürlimann *et al.* (1999) illustrated how pore-water pressures strongly increased

during rapid loading in undrained conditions. Earthquakes, a common process in active volcanic areas, can cause fast loading resulting in saturated soil. Heavy rainfall is also known to be a frequent cause of the generation of elevated pore-water pressures (Siebert 2002).

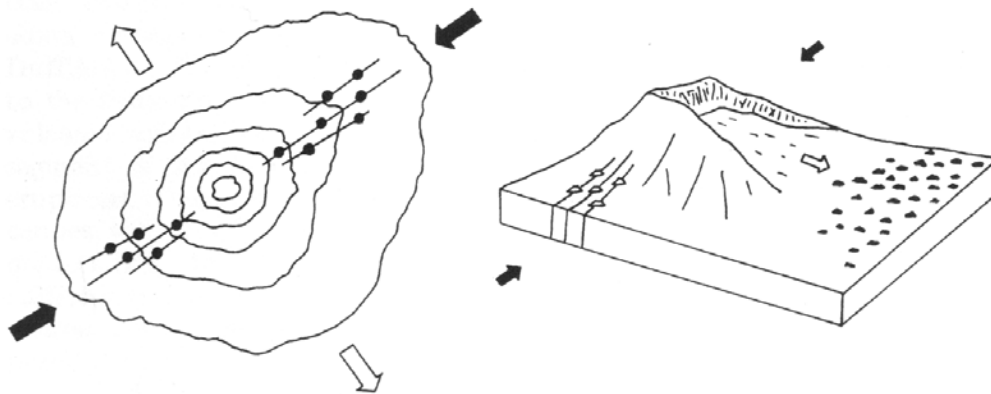


Figure 2.2 – Schematic illustrating the direction of proposed dilational stresses associated with the intrusion of dykes within the volcano edifice. It is thought that intruding dykes promote collapse in a direction perpendicular to that of intrusion orientation. Black arrows indicate orientation of dyke intrusion. White arrows indicate likely direction of collapse. Adapted from Siebert (1984).

### 2.3.5 DESTABILISING LAYERS

Stability modelling indicates that volcano slopes composed of materials with common strength properties tend to be very stable, suggesting that the presence of a weak ‘destabilising layer’ is needed in order to reduce the strength of the volcanic pile (Hürlimann *et al.* 1999). Proposed destabilising layers include pyroclastic rocks within volcanic slopes or at the basement contact (Siebert 1984) and palaeosols (Hürlimann *et al.* 1999). Lava flows subsequent to palaeosol formation may result in massive lavas overlaying what is one of the weakest materials found on the edifice.

### 2.3.6 CONE MORPHOLOGY

Changes in morphology of the volcano flank can strongly influence volcano stability. Hürlimann *et al.* (1999) found considerable stress anomalies, distinguished by high shear stress, to be located within the edifice where the slope inclination changes from steep cone to the smooth volcano flank. The presence of

canyons provided similar anomalies as shown in Figure 2.3. It is not improbable that large landslides may be initiated in these high stress zones of the volcanic slope.

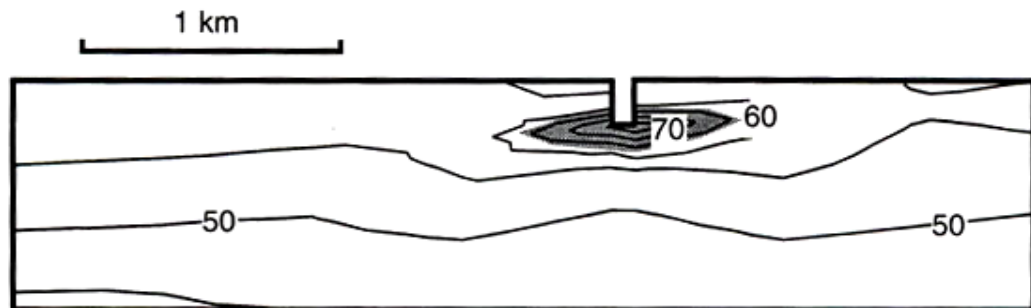


Figure 2.3 – Schematic illustrating shear stress distribution in relation to morphological changes on the volcano flanks. The image above shows how shear stresses increase near the base of the canyon where the highest values are located. Values in MPa. Sourced from Hürlimann *et al.* (2002).

Slope angle also contributes to failure at volcanoes, more so on steep flanked stratovolcanoes than low-angle shield volcanoes. Figure 2.4 shows a possible correlation between slope angle and the frequency of major slope failure for Quaternary volcanoes which have undergone major slope failure. Landslides appear most likely on slope angles between 20 – 36°.

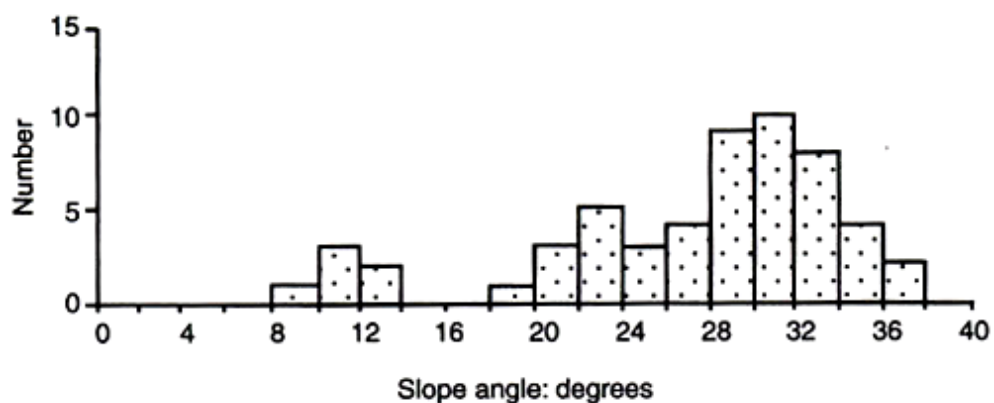


Figure 2.4 – Slope angle of Quaternary volcanoes that have undergone major slope failure ( $n = 55$ ). Sourced from Siebert (1999).

### 2.3.7 MULTIPLE FACTORS

It is highly likely that the inherent instability of volcanoes is attributable to a combination of events or circumstances rather than any single process (Figure 2.5). While a final factor may ‘trigger’ a volcanic landslide, it is never the sole cause. Magmatic intrusions at Bezymianny Volcano, Kamchatka in 1956 and Mount St Helens, Washington in 1980 produced major deformation (Voight *et al.* 1983; Siebert 2002), while earthquakes precipitated edifice failure (Siebert 2002). Active hydrothermal and magmatic systems both had an influence on the collapse of Nevado de Colima, Mexico (Stoopes & Sheridan 1992). Voight & Elsworth (1997) concluded that intense, variably-oriented jointing, and hydrothermal alteration is particularly significant in reducing shear strength of volcanic slopes. However, it is the superposition of subsequent factors, such as pore water pressure enhancement, that cause this gradually weakened material to fail. The large population of volcanoes meeting slope angle criteria, for example, that have not to this point undergone failure, suggests that a triggering mechanism is required to initiate failure (Siebert 1996).

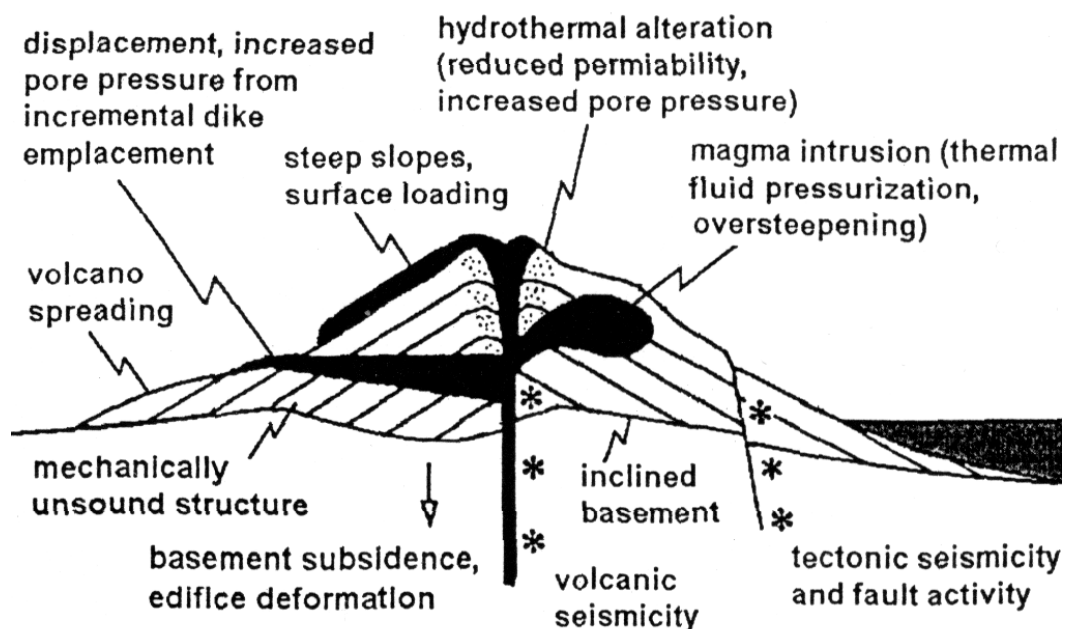


Figure 2.5 – Factors contributing to the inherent instability of volcanoes. Sourced from Siebert (2002).

## 2.4 GEOTECHNICAL CLASSIFICATION OF VOLCANOES

The objectives and processes involved in the geotechnical assessment of volcano stability is in theory no different to any other geotechnical stability investigation. Detailed geomorphological field mapping of the field area must be carried out identifying and classifying rock masses and their structure, laboratory analysis must follow measuring intact rock strength, after which numerically based stability analysis is undertaken. However, the lack of rock strength data for most volcanoes, partly reflecting the difficult logistical and, in certain instances, hostile work environment, largely hinders quantitative assessment of volcano slope stability (Watters & Delahaut 1995; Watters *et al.* 2000).

Authors such as Voight, Siebert, Watters, Hürlimann and more recently Zimbelman, have made great contributions to volcanic stability research. Detailed discussions presented by Siebert (1984; 1996; 2002), Voight & Elsworth (1997) and Voight (2000) are of critical importance in regard to theoretical considerations important in the stability of volcanoes. Equally important are the works of Hürlimann (1999) and Hürlimann *et al.* (2000) who evaluated the causes of volcanic landslides in the Canary Islands using numerical stability models, while Watters *et al.* (2000) and Thomas *et al.* (2004) applied rock mass classifications in their assessment of the stability of volcanoes in the Cascade Ranges, west coast of United States of America. More recently, Zimbelman *et al.* (2003) and Zimbelman *et al.* (2004) combined the theoretical, geological, geotechnical and numerical methods of others in assessing the stability of Citlaltepétl Volcano in Mexico.

### 2.4.1 ROCK MASS CLASSIFICATION

Rock mass classification schemes are an empirical design method which has been successfully applied throughout the world. These classification schemes seek to assign numerical values to those properties or features of the rock mass considered likely to influence its behaviour, and to combine these individual values into one overall classification rating for the rock mass (Brady & Brown 2004). While rock mass classifications have never been intended to replace analytical studies, field measurement or engineering judgment, the operational and economical difficulties of *in situ* testing (highlighted in Sonmez *et al.* (2004) and

Hoek & Diederichs (2006)), have increased the popularity of rock mass classifications.

To apply a rock mass classification scheme, the rock mass is divided into a number of structural regions such that certain features are more or less uniform within each region. While rock masses are discontinuous in nature, they may nevertheless be uniform in regions, the boundaries of structural regions generally coinciding with major geological features such as faults and shear zones (Bieniawski 1989). When delineating structural regions in a volcanic setting, Watters *et al.* (2000) highlighted the importance of accounting for the degree of alteration of a rock mass, while Zimbelman *et al.* (2004) state that it is best to concentrate on those areas which are most intensely altered as these represent the weakest rocks of the volcanic edifice.

Many rock mass classification schemes exist. For this study the Rock Quality Designation (RQD), basic Rock Mass Rating (RMR), and modified Geological Strength Index (GSI) were applied. The RQD is a prerequisite for the RMR, and the parameters of discontinuity spacing, roughness, weathering and infilling from the RMR are required for the modified GSI. The modified GSI is essential for the calculation of Hoek-Brown strength parameters and conversion to equivalent Mohr-Coulomb values – data that are essential for stability modelling. Thus, all three rock mass classifications are necessary in this study.

#### **2.4.1.1 ROCK QUALITY DESIGNATION**

The RQD proposed by Deere (1964) is related to the degree of fracturing of a core. The RQD calculates the total lengths of all intact segments of a core with a length > 100 mm. These lengths are added together and expressed as a percentage of the total core length, grading from very poor rock (< 25 %) through to excellent rock (> 90 %). Cores however, are not always readily available so Priest & Hudson (1976) proposed the following relationship between the average number of discontinuities per metre and the theoretical RQD of a rock mass:

$$\text{RQD} = 100 e^{-0.1\lambda} (0.1\lambda + 1) \quad (2.1)$$

where:  $\lambda$  = number of discontinuities per metre that are  $> 0.1$  m.

While giving a simple and inexpensive means of determining fracture intensity of a rock mass, the RQD ignores discontinuity characteristics of the rock mass such as orientation, aperture and infilling.

#### **2.4.1.2. ROCK MASS RATING**

The RMR system, or Geomechanics Classification, was first introduced by Bieniawski (1973) and has since been modified to conform with international standards and procedures. The RMR uses the following six parameters to classify a rock mass:

- 1) uniaxial compressive strength of the intact rock mass;
- 2) RQD;
- 3) spacing of discontinuities;
- 4) condition of discontinuities;
- 5) groundwater conditions; and
- 6) orientation of discontinuities.

When applying the RMR, a large number of measurements for each parameter are averaged to provide statistically accurate data. Ratings are assigned to each parameter according to Figure 2.6. These ratings vary according to the importance of the parameter; the higher the rating the greater the effect on rock mass conditions and vice versa. The overall RMR for the structural region under consideration is obtained by adding the values of the ratings determined for the individual parameters. RMR ratings range from 0 – 100.

#### **2.4.1.3 GEOLOGICAL STRENGTH INDEX**

Hoek *et al.* (1992), Hoek (1994) and Hoek *et al.* (1995) developed the GSI to overcome some of the deficiencies that had been identified when using the RMR scheme with rock mass strength criteria. The GSI is based on the understanding that the strength of a jointed rock mass is dependent on the freedom of the rock

pieces to slide and rotate under different stresses, this freedom in turn being controlled by the geometrical shape of the intact rock pieces and the condition of the surfaces separating the pieces (Brady & Brown 2004). GSI values are obtained using a table of the degree of fracturing, or the structure, and the fracture surface condition as shown in Figure 2.7. There are four structure categories ranging from blocky through to disintegrated and five fracture surface conditions ranging from very good through to very poor.

<b>Strength of intact rock material</b>							
Point-load strength index (MPa)	> 10	4 – 10	2 – 4	1 – 2	Uniaxial preferred at this low range		
Uniaxial compressive strength (MPa)	> 250	100 – 250	50 – 100	25 – 50	5 – 25	1 – 5	< 1
Rating	15	12	7	4	2	1	0
<b>RQD</b>		90 – 100	75 – 90	50 – 75	25 – 50	< 25	
Rating		20	17	13	8	3	
<b>Discontinuity spacing</b>	> 2.0 m	0.6 m – 2.0 m	200 mm – 0.6 m	60 mm – 200 mm	< 60 mm		
Rating	20	15	10	8	5		
<b>Condition of discontinuities</b>							
Persistence (m)	< 1 m	1 – 3 m	3 – 10 m	10 – 20 m	> 20 m		
Rating	6	4	2	1	0		
Aperture (mm)	None	< 0.1	0.1 – 1.0	1 – 5	> 5		
Rating	6	5	4	1	0		
Roughness	Very rough	Rough	Slightly rough	Smooth	Polished		
Rating	6	5	3	1	0		
Infill	None	Hard; < 5 mm	Hard; > 5mm	Soft; < 5 mm	Soft; > 5 mm		
Rating	6	4	2	2	0		
Weathering	Non	Slightly	Moderate	Highly	Rotten		
Rating	6	5	3	1	0		
<b>Groundwater (general conditions)</b>	Dry	Damp	Wet	Dripping	Flowing		
Rating	15	10	7	4	0		
<b>Rock mass class determined from total ratings</b>							
Rating	100 – 81	80 – 61	60 – 41	40 – 21	< 21		
Class No.	I	II	III	IV	V		
<b>Description</b>	<b>Very good rock</b>	<b>Good rock</b>	<b>Fair rock</b>	<b>Poor rock</b>	<b>Very poor rock</b>		

Figure 2.6 - The RMR system or Geomechanics Classification. Adapted from Bieniawski (1973).

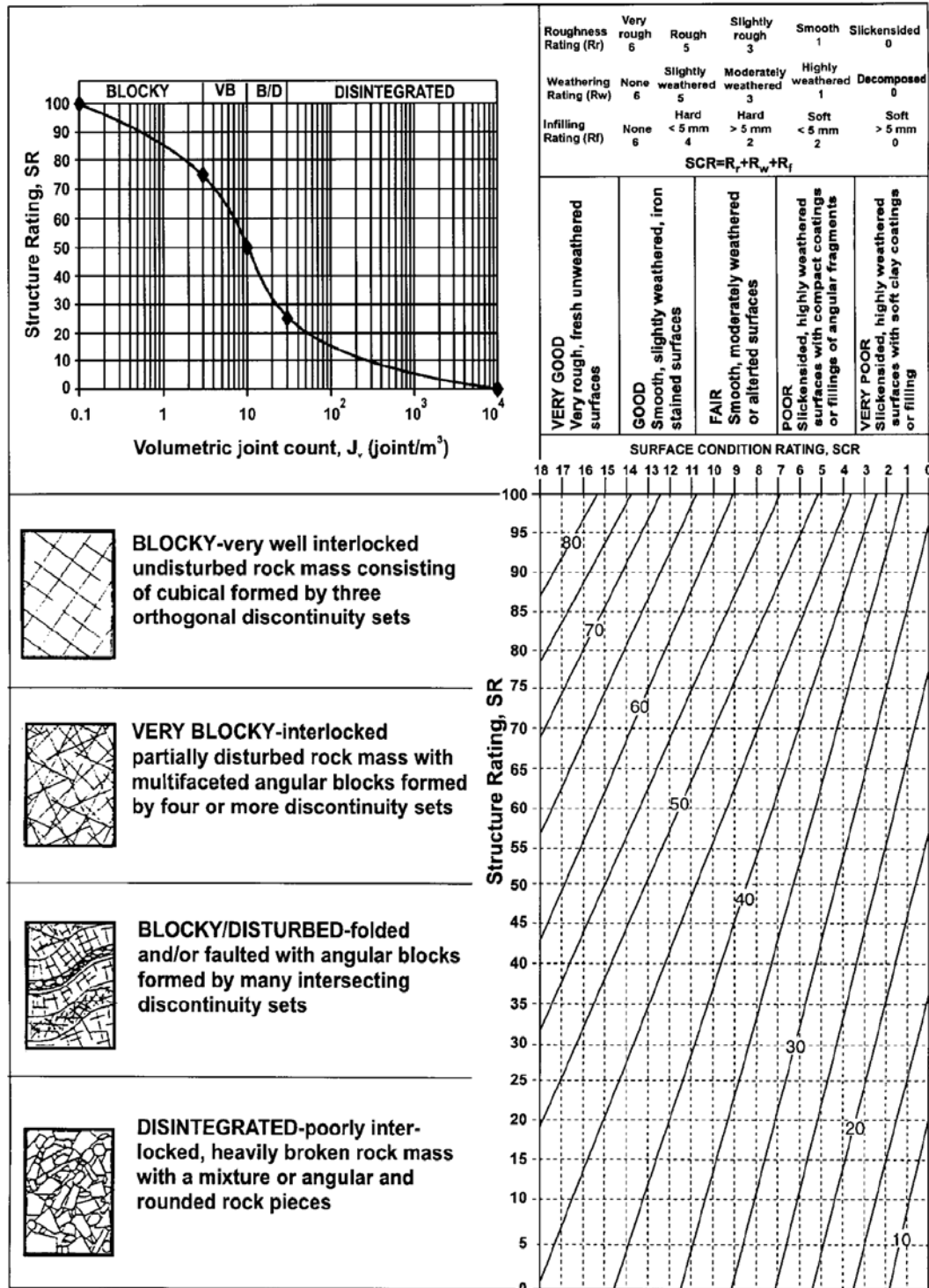


Figure 2.7 – The modified GSI classification scheme. Sourced from Sonmez & Ulusay (1999).

The creators of the GSI have never hidden the fact that the index is subjective; the final classification originating from qualitative visual examination of the rock mass. In an attempt to provide a more quantitative numerical basis for the GSI,

Sonmez & Ulusay (1999) suggested a modified GSI which introduced two terms into the existing GSI classification scheme; structure rating and surface condition rating. In order to assign ratings to these terms, it was suggested that easily measurable input parameters such as joint roughness and weathering, infilling, and volumetric joint be used (top of Figure 2.7). The intersection of these terms on the GSI table is used to assign a GSI value. While the modified GSI has attempted to provide a more numerical basis for classification of rock masses, it is still best not to be too precise when assigning a GSI value to a rock mass. In most cases the GSI should be stated as a range.

## 2.4.2 ORGANISING DATA FOR STABILITY MODELLING

When carrying out slope stability analysis, it is a general requirement of stability models that rock mass strength data be in the form of one of two strength criteria; the Hoek-Brown strength criterion (written in terms of major and minor effective principal stresses at failure, uniaxial compressive strength of the intact rock mass and the material constants  $m$  and  $s$ ), or the Mohr-Coulomb strength criterion (written in terms of cohesion and friction angle).

### 2.4.2.1 HOEK-BROWN STRENGTH PARAMETERS

The Hoek-Brown strength criterion of Hoek & Brown (1980) was designed initially as a basis for providing input data for the analysis and design of underground excavations in hard rock. The criterion is given by the equation:

$$\sigma_1' = \sigma_3' + \sigma_{ci} \left( m \frac{\sigma_3'}{\sigma_{ci}} + s \right)^{0.5} \quad (2.2)$$

where  $\sigma_1'$  and  $\sigma_3'$  are major and minor effective principal stresses at failure,  $\sigma_{ci}$  is the uniaxial compressive strength of the intact rock mass and  $m$  and  $s$  are material constants ( $s = 1$  for intact rock).

The authors sought to link the empirical criterion to geological observations by means of one of the available rock mass classification schemes and, for this purpose they chose the RMR proposed by Bieniawski (1973). Due to the lack of suitable alternatives, the criterion was soon adopted by the rock mechanics

community and its use quickly spread beyond the original design limits. Consequently, it became necessary to re-examine these relationships and introduce new elements to account for the wide range of practical problems to which the criterion was being applied (Hoek *et al.* 2002). This led to revision of the criterion and the introduction of the Generalised Hoek-Brown criterion (Hoek 1994) defined by the equation:

$$\sigma'_1 = \sigma'_3 + \sigma_{ci} \left( m_b \frac{\sigma'_3}{\sigma_{ci}} + s \right)^a \quad (2.3)$$

Note that  $m$  is replaced by  $m_b$ , the material constant for the whole rock mass. The value for  $m_b$  is calculated from a reduced value of  $m_i$ , the material constant for intact rock, by incorporating the GSI and a disturbance factor (D) as follows:

$$m_b = m_i \exp\left(\frac{GSI - 100}{28 - 14D}\right) \quad (2.4)$$

D varies from 0 for undisturbed *in situ* rock masses to 1 for very disturbed rock masses. Because the basis of assigning a D value is qualitative, interpretation of D is rather subjective. Wyllie & Mah (2004) have presented guidelines on the categorisation of D in mining situations where blast damage and stress relaxation may disturb the rock mass. The GSI was introduced to the equation after recognition that the RMR was no longer adequate as a basis for relating geological observations in the field to the failure criterion. Calculation of  $m_i$  is usually from the ratio of compressive strength to the tensile strength:

$$\frac{\sigma_c}{\sigma_t} \approx m_i \quad (2.5)$$

In order for  $\sigma_c$  and  $\sigma_t$  to be determined, triaxial tests are required. If triaxial tests are not possible, values of  $m_i$  for a wide variety of rock types available in the literature (for example Hoek (1994)) may be substituted.

Having calculated  $m_b$ , this leaves only  $s$  and  $a$  to be determined which are given by the following equations:

$$s = \exp\left(\frac{GSI - 100}{9 - 3D}\right) \quad (2.6)$$

$$a = \frac{1}{2} + \frac{1}{6} (\exp^{-GSI/15} - \exp^{-20/3}) \quad (2.7)$$

For comparative reasons it may be necessary to present material strength properties in the form of Mohr-Coulomb parameters (cohesion and friction angle). Calculation of equivalent Mohr-Coulomb parameters from Hoek-Brown parameters can be simply undertaken using rock mass strength analysis programs such as RocLab<sup>TM</sup>. Alternatively, the conversion may be possible using slope stability analysis programs.

### 2.4.3 STABILITY MODELLING

Stability models are of vital importance to volcano stability assessment, as they show how changes in rock strength and/or internal geologic structure can affect volcano slope stability (Apuani *et al.* 2005). A number of different methods have been used to model the stability of volcanic slopes including 2-dimensional limit equilibrium analysis (Hürlimann *et al.* 1999; Voight 2000; Moon *et al.* 2005), 3-dimensional limit equilibrium analysis (Reid *et al.* 2000) and 2-dimensional distinct element models (the most commonly used being UDEC) (Zimbelman *et al.* 2004). Recently, 3-dimensional distinct element models (for example 3DEC) have been introduced to model slope stability (Wyllie & Mah 2004); however, their application to volcanic edifices is, to date, very limited.

Distinct element models operate by representing the failed mass as an assemblage of discrete blocks, the boundaries of each individual block being assigned strength characteristics reflecting chemical alteration, faulting, or lithological variations (Zimbelman *et al.* 2004). A time stepping function allows the model to fail, and the velocity and displacement histories of specific blocks are traced (Figure 2.8).

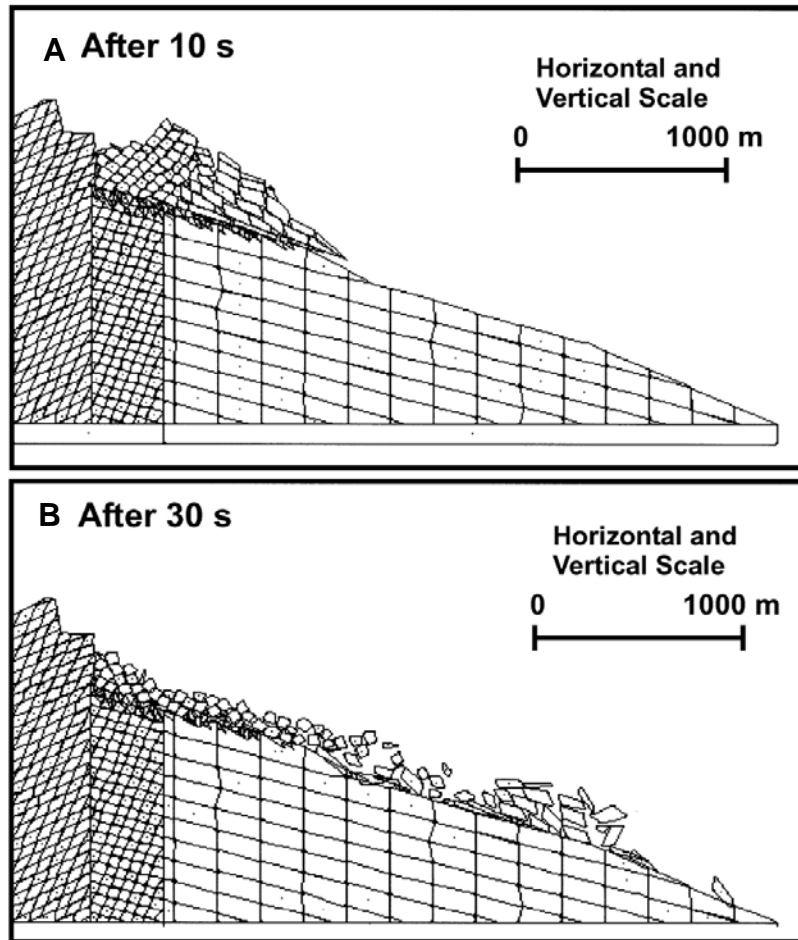


Figure 2.8 – Modelled failure of a volcanic cone using a two dimensional distinct element model. (A) At 10 seconds after failure initiation; and (B) at 30 seconds after failure initiation, intact block begins to disaggregate into smaller pieces. Shaded regions indicate differing lithologies. Sourced from Zimbelman *et al.*(2004)

A more simplistic approach is that of limit equilibrium analysis, which quantifies the stability along a predetermined failure plane via the ratio of the forces resisting failure and the forces driving failure (Wyllie & Mah 2004). This ratio is termed the factor of safety (F) and is expressed as:

$$F = \frac{\text{sum of resisting forces (A)}}{\text{sum of driving forces (B)}} \quad (2.8)$$

When  $A = B$ ,  $F = 1.0$ . As  $F$  increases  $> 1.0$ , so too does the likelihood of a stable slope. An  $F$  value  $< 1.0$  represents a more unstable slope. An accurate

understanding of the parameters controlling slope stability can never be known precisely, thus  $F$  quoted to one decimal place is generally suitable.

Due the present shortage of numerical data relating to volcanic slope stability, in attempting to model such a complex system, a number of simplifications must be incorporated into stability models, making any results not absolute (Apuani *et al.* 2005). As complete stability of a slope is non-existent, the models reflect nature satisfactorily.

## **2.5 SUMMARY**

Volcanic landslides are not the rare event they were once thought to be. Many examples of volcanic collapse have been identified in the international literature. A range of factors is recognised as being influential in the initiation of volcanic landslides, including rock alteration, magmatic intrusions, pore-water pressures, seismic accelerations, destabilising layers, and cone morphology. However, while it is possible to identify many individual factors important in volcanic collapse, the most likely scenario is that multiple factors are responsible.

Geotechnical assessment of a volcano is in theory no different to any other form of slope stability investigation. It is, however, an area of research which remains in its infancy, meaning rock strength data for volcanoes are limited. Recently, authors such as Zimelman (2003; 2004) have combined theoretical, geological, geotechnical and numerical methods in their attempt to assess volcano stability. They highlighted the important role of rock mass classification schemes in interpreting volcano edifice strength, noting the significance of altered rock masses when selecting structural regions.

Strengths of rock masses are calculated via the Hoek-Brown strength criterion (or alternatively the Mohr-Coulomb criterion). The output values from these criteria are generally accepted directly by stability models. The power of stability models lies in their ability to assess how changes in rock strength and/or internal geologic structure can affect volcano slope stability. Different methods of stability analysis have been used to assess model volcanic slopes including distinct element models and limit equilibrium methods.

# CHAPTER 3

## ***METHODOLOGY***

---

### **3.1 INTRODUCTION**

The methodology of this study involved three separate stages, each of which is required to determine the stability of a slope.

Firstly, the geomorphology of the field area was mapped using a combination of stereoscopes and field reconnaissance. Geographical information systems (GIS) played an important role in geomorphic mapping for its ability to produce spatially referenced maps of the field area. GIS was also implemented to produce topographical profiles of the field area which were later used for stability modelling.

Secondly, rock masses in the field area were described and both hard and soft rocks defined. Description of rock mass strength of hard and soft rocks follows the guidelines of the New Zealand Geotechnical Society for the field description of rock and soil respectively (Burns *et al.* 2005). Rock mass classification schemes completed rock mass description.

Finally, geotechnical properties of each rock mass were measured in the laboratory. Hard rock masses incorporated point load strength testing, bulk density and porosity measurements, while discontinuity orientation was assessed using stereonet analysis. Soft rock masses incorporated direct shear strength tests and bulk density measurements.

### **3.2 GEOMORPHOLOGY**

#### **3.2.1 GEOGRAPHICAL INFORMATION SYSTEMS (GIS)**

GIS is a group of spatially referenced computer based mapping programs that allow integration and visualisation of spatial data. Due to its ability to produce geographically referenced maps, ArcGIS™ 9.1 was selected to produce maps of

the study area. Pre-existing NZMS 260 1:50,000 datasets for contours (20 m intervals), river systems, road networks, townships and spot heights were imported into GIS producing geographically referenced maps of the field area. New datasets, in the form of global positioning system (GPS) waypoints, were recorded in the field and imported into GIS. GPS waypoints indicated rock mass description, sampling and field measurement locations. Digital elevation models (DEM), which portray spatial data in three dimensions (x, y and z), were produced for the study area, vastly simplifying visual interpretation of the landscape.

### **3.2.2 TOPOGRAPHICAL PROFILES**

Galena™, the slope stability program used in this study, requires the topographical profile of a slope in order to assess its stability (complete details of Galena™ are discussed in Chapter 6). Topographical profiles were constructed by drawing a run-line digitally onto a DEM. The run-line represents the path of the topographical profile. With the aid of an AML (automated macro language file), height points along the run-line were recorded as a database file in the form of x (horizontal distance along the run-line) and y (elevation) co-ordinates. The horizontal spacing at which height points were recorded along the run-line is adjustable depending on how many x points were required. Galena™ accepts a maximum of 48 x/y co-ordinate pairs, so the AML was programmed to record 48 heights. For example, a run-line 4080 m in length would be sampled every 85 m producing 48 sample heights. Exporting the database file to Microsoft® Excel allowed for plotting horizontal distance (x axis) against elevation (y axis). This produced a topographical profile of that run-line based on 48 x/y co-ordinate pairs. These co-ordinate pairs were then imported into Galena™ from Microsoft® Excel.

### **3.2.3 GEOMORPHIC DESCRIPTION**

Description of the geomorphology of Putauaki and the surrounding landscape was carried out initially using a combination of aerial photographs viewed three dimensionally under stereoscopes, and topographical maps. Geomorphic details that were mapped included breaks in slope, slope angles, evidence of erosional and/or depositional features, valley and ridge-line trends, and alluvial systems. Field mapping expanded upon initial geomorphic description by providing

measured slope angle data, scale sketches of slope morphology, and panoramic photographs allowing correlation and comparison of geomorphic features. Based on this geomorphic information, landform units including alluvial plains, strongly and subdued dissected landscape, concave and convex slope units, and rounded and angular slope breaks were defined, and their boundaries hand sketched onto base maps. This hand sketched geomorphic information was then digitised into GIS as a new spatially referenced data layer.

### **3.3 ROCK MASS DESCRIPTION**

In the past, description of Putauaki has taken a lithological and petrological perspective (Duncan 1970; Carol 1998) meaning attention has not been directed to the geotechnical characteristics of the rock masses that are so important to this study. It was therefore important for this study to describe the rock masses of Putauaki from a geotechnical viewpoint.

When describing a rock mass, it is imperative to locate exposures that are representative of the rock mass as a whole. The steep flanks and dense vegetation of Putauaki meant accessing suitable exposures was difficult and sometimes hazardous. In some instances, exposures were described from afar meaning quantitative measurements for that exposure could not be attained. Often, it was found to be easier and safer to describe exposures in close proximity to summit access tracks. Accessibility was therefore a limiting factor in selecting description locations.

Once representative exposures were selected, the next stage of describing a rock mass is measurement of rock mass strength. Rock mass strength was measured at a total of 32 sites, the locations of which are illustrated in Figure 3.1. Measurement of rock mass strength is discussed in Sections 3.3.1 – 3.3.2. Finally, rock masses were classified using rock mass classification schemes (Section 3.3.3).

Rock mass descriptions for both hard and soft rock were incorporated into this study to describe the rock masses of Putauaki. Hard rock is defined here as material that is indurated to the point where intact field samples can be collected

in the form of fallen blocks. Alternatively, soft rocks must be sampled via soil cores or a sample bag of loose material. The separation of these two rock types is important as different approaches must be employed in order to describe and quantify the geotechnical characteristics of each.

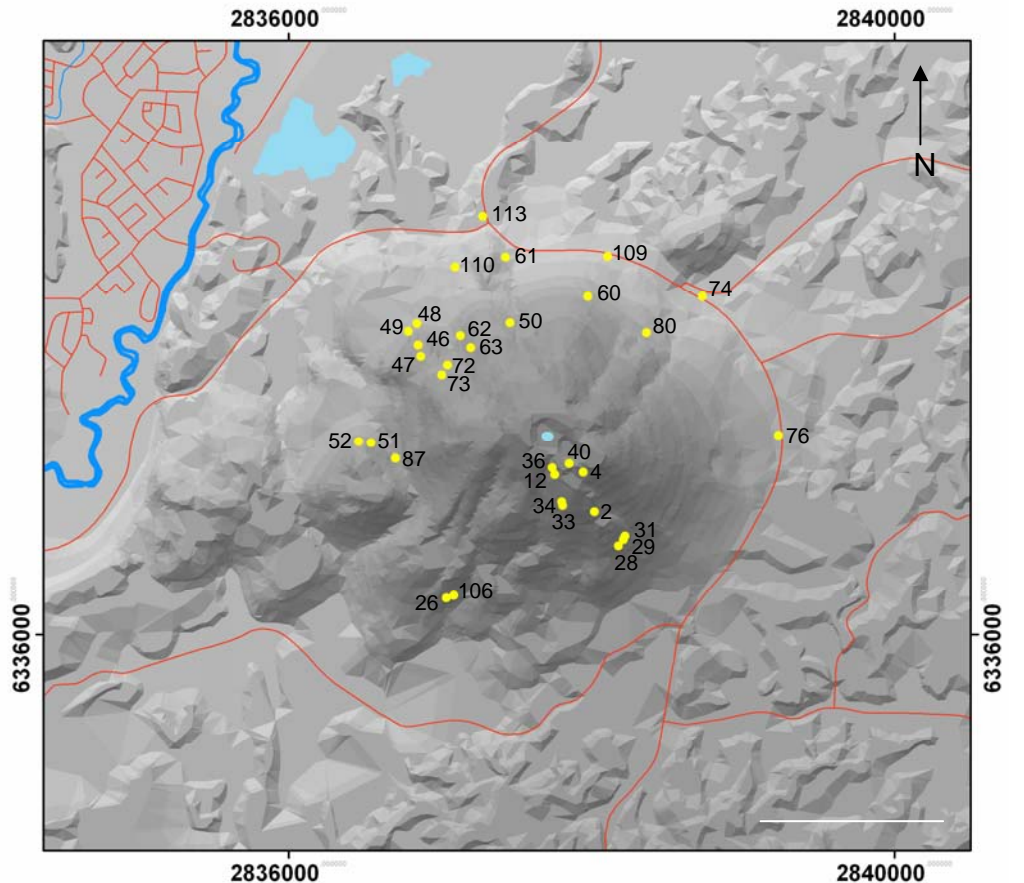
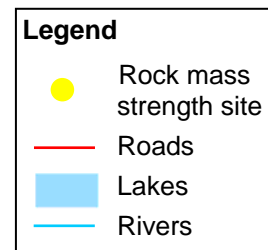


Figure 3.1 – DEM indicating location of rock mass strength measurements (yellow markers). Numbers indicate site numbers. White bar represents 1 km.



### 3.3.1 ROCK MASS STRENGTH OF HARD ROCKS

A number of factors control the strength of a rock mass, and as a result numerous classifications of rock mass strength have been proposed for geotechnical purposes (as listed in Selby (1993)). For this study, measurement of rock mass strength of hard rocks followed the guidelines of the New Zealand Geotechnical

Society for the field description of rock (Burns *et al.* 2005). Parameters measured are presented in Appendix A and include weathering state, colour, grain size, texture, intact strength, an inferred rock name, fabric, and presence of bedding. Discontinuities were also measured (Section 3.3.1.2), as was grain size and texture from a volcanological perspective (after Best & Christiansen (2001)). Small but representative hand specimens were collected to accompany each rock mass strength description.

### **3.3.1.1 SCHMIDT HAMMER**

The Schmidt hammer test is designed to provide a simple field index value of the intact strength of a rock mass. The advantage of the Schmidt hammer is that it is light and easily transportable into the field where large numbers of tests can be carried out in a relatively short time (Selby 1993).

Following a method similar to that suggested by Brown (1981), 20 test impact readings were recorded at each site, an average of the 10 highest readings being interpreted as the rebound value of the rock mass. Test impact sites were more than 60 mm from an edge or discontinuity, and flat and free from debris as suggested by (Selby 1993). All hammer tests were in a horizontal direction so no correction was required. The N type Schmidt hammer was used for this study.

### **3.3.1.2 DISCONTINUITIES**

Discontinuities within a rock mass concentrate stresses, influence groundwater movement, act as potential failure planes and in general weaken the rock mass (Selby 1993; Wyllie & Mah 2004). Therefore, in order to gain even a partial understanding of the rock mass, the discontinuities must first be addressed.

A representative description of the discontinuity population as a whole was carried out at the 32 sites where rock mass strength was measured (Figure 3.1). Data collected included persistence, aperture, nature of filling, surface roughness and shape, seepage, dip and dip direction of major discontinuity sets, and a representative description of the upper and lower terminations of discontinuities. Termination descriptions included visible/discontinuity, visible/rock, or not visible.

### 3.3.1.2.1 SCANLINE SURVEYS

A more in-depth description of discontinuities at the outcrop scale was carried out via the scanline survey approach (Figure 3.2). This method involves attaching a measuring tape to the outcrop face, after which the nature of all discontinuities intersecting the measuring tape is described. Parameters measured for each discontinuity are the same as those described in Section 3.3.1.2.

Five scanline surveys were carried out at sites 12, 26, 33, 40 and 52 (Figure 3.1). Refer Appendix B for parameters measured in each scanline survey.

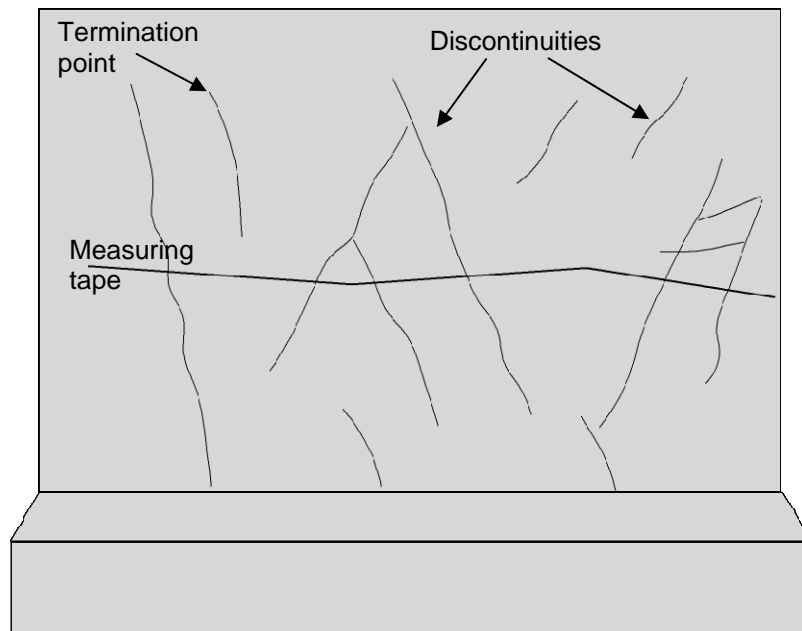


Figure 3.2 – Schematic diagram of a scanline survey. Adapted from Brady & Brown (2004)

### 3.3.1.2.2 DISCONTINUITY SPACING

The perpendicular distance between adjacent discontinuities refers to the discontinuity spacing. Spacing of discontinuities determines the dimensions of blocks in the slope which in turn influences the scale of potential rock falls. Discontinuity spacing was measured as the difference between successive ‘distance’ measurements where the discontinuities intersect the scanline (Figure 3.2). Spacing terms are defined in Table 3.1.

Table 3.1 – Terms describing discontinuity spacing. Adapted from Burns *et al.* (2005).

<b>Term</b>	<b>Spacing</b>
Extremely widely spaced	> 6 m
Very widely spaced	2 – 6 m
Widely spaced	2 m – 600 mm
Moderately widely spaced	600 – 200 mm
Closely spaced	200 – 60 mm
Very closely spaced	60 – 20 mm
Extremely closely spaced	< 20 mm

### 3.3.1.2.3 DISCONTINUITY ORIENTATION

The orientation of discontinuities with respect to slopes is the primary geological factor influencing slope stability (although other properties such as persistence and spacing are significant) (Selby 1993; Wyllie & Mah 2004). Discontinuity dip and dip direction were measured in the field using a Clar-type geological compass. Discontinuity dip is defined as the maximum inclination of a discontinuity to the horizontal in degrees. The dip direction of a discontinuity is defined as the direction of the horizontal trace of the line of dip measured clockwise from north (Wyllie & Mah 2004) (Figure 3.3). All discontinuity orientations presented in this study are in the form of dip/dip direction (for example 30/089).

### 3.3.1.2.4 DISCONTINUITY INFILL

Infill is the term given to material which separates adjacent walls of discontinuities. If the discontinuity contains infilling, the shear strength properties are often modified by the thickness and properties of the infill (Wyllie & Mah 2004). In this study, discontinuity surfaces were typically clean, meaning shear strength is derived solely from the rock material. On the odd occasion where infill was observed, the coarse nature and limited volume of the material restricted sampling for shear tests. Where possible, infill was described following guidelines set out by the New Zealand Geotechnical Society for the field description of soil (Burns *et al.* 2005).

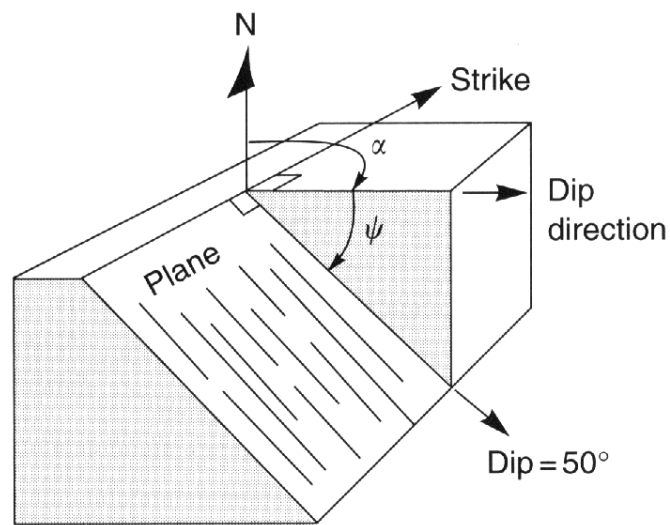


Figure 3.3 – Schematic illustrating dip and dip direction of a discontinuity. Discontinuity dip is defined as the maximum inclination of a discontinuity to the horizontal in degrees. Dip direction is defined as the direction of the horizontal trace of the line of dip measured clockwise from north. Sourced from Wyllie & Mah (2004)

#### 3.3.1.2.5 DISCONTINUITY PERSISTENCE

Persistence describes the trace length of a discontinuity to its termination in solid rock or against other discontinuities, as observed in an exposure. This parameter essentially defines the size of blocks and the length of a potential sliding surface. Persistence terms are not defined by the New Zealand Geotechnical Society, thus description of persistence follows the scheme of Brown (1981) (Table 3.2).

Table 3.2 – Terms describing discontinuity persistence. Adapted from Brown (1981).

<b>Term</b>	<b>Persistence</b>
Very low persistence	< 1 m
Low persistence	1 – 3 m
Medium persistence	3 – 10 m
High persistence	10 – 20 m
Very high persistence	> 20 m

### 3.3.1.2.6 DISCONTINUITY ROUGHNESS

The roughness of a discontinuity is an important component of the shear strength, particularly where the discontinuity is not filled. A profile gauge, consisting of a row of pins held together in a single layer which is free to move in response to undulations on the discontinuity surface, was used to measure the surface roughness of discontinuities (Figure 3.4a). The profile gauge was pressed against the surface (in a number of different directions) and the resulting profiles sketched and compared against roughness grades (Figure 3.4b).

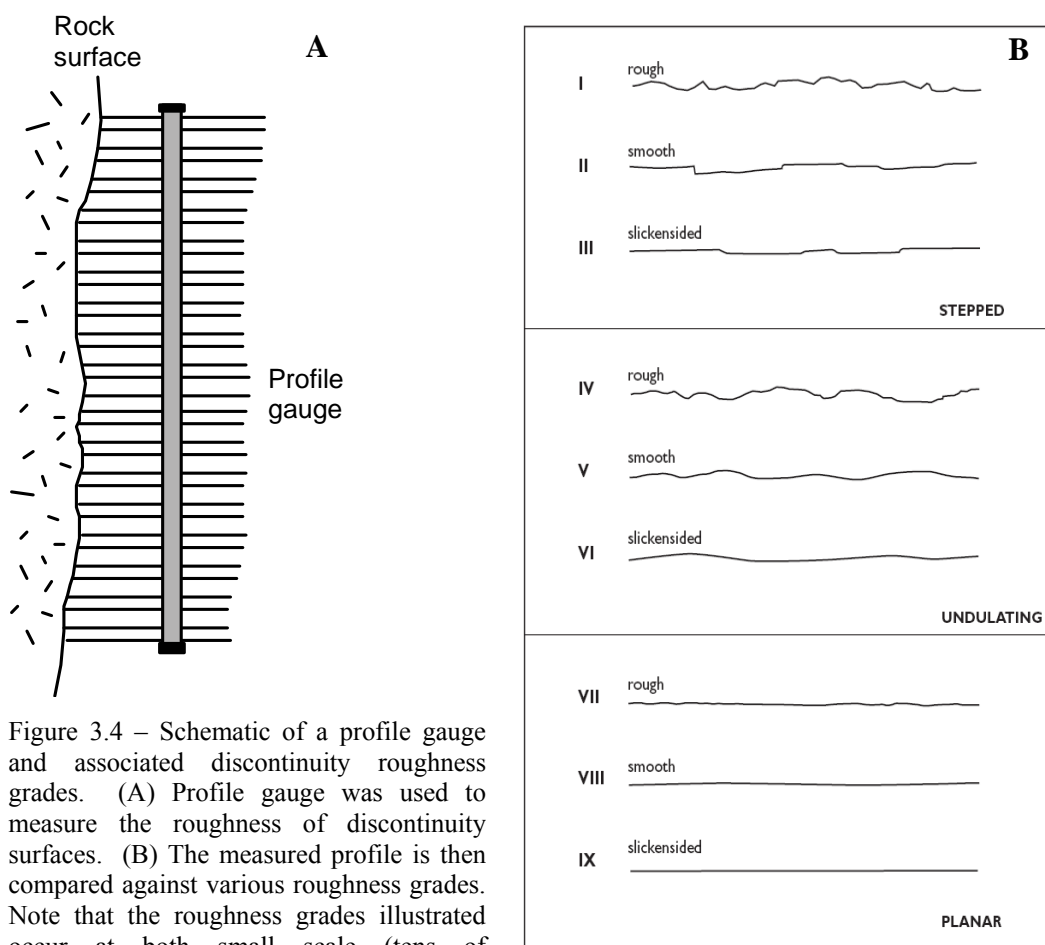


Figure 3.4 – Schematic of a profile gauge and associated discontinuity roughness grades. (A) Profile gauge was used to measure the roughness of discontinuity surfaces. (B) The measured profile is then compared against various roughness grades. Note that the roughness grades illustrated occur at both small scale (tens of millimetres) and large scale (several metres). Adapted from Bradshaw (2004).

### 3.3.1.2.7 DISCONTINUITY SEEPAGE

Water seepage through rock masses results mainly from flow within the discontinuities. The presence of groundwater in a rock slope can have a

detrimental effect upon stability for a number of reasons, perhaps the most important being the ability of water pressures in a discontinuity to reduce the shear strength of potential failure surfaces. Seepage ratings are not defined by the New Zealand Geotechnical Society, thus description of seepage follows the scheme of Brown (1981) (Table 3.3).

### 3.3.1.3 SAMPLING

Hard rock samples were collected for laboratory determination of point load strength, porosity and bulk density (Section 3.4). Samples were collected in the form of fallen blocks from each scanline site (sites 12, 26, 33, 40 and 52 on Figure 3.1). Samples collected met the guidelines of Franklin (1985) (for determining point load strength) and Brown (1981) (for determining porosity and density using the saturation and buoyancy technique).

Table 3.3 – Terms describing seepage. Adapted from Brown (1981).

<b>Description</b>	<b>Seepage rating</b>
Tight and dry, water flow does not appear possible	I
Dry with no evidence of water flow	II
Dry, but shows evidence of water flow (for example rust staining)	III
Damp but no free water present	IV
Shows seepage, occasional drops of water but no continuous flow	V
Continuous flow of water	VI

### 3.3.2 ROCK MASS STRENGTH OF SOFT ROCKS

Where possible, rock mass strength of soft rock masses was described following those guidelines previously discussed for describing hard rock masses. However, a lack of discontinuities within the soft rocks generally meant this description was brief and often uninformative. In this case, description of the rock mass strength of soft rocks followed the guidelines of the New Zealand Geotechnical Society for the field description of soil (Burns *et al.* 2005). For geotechnical purposes, soils

can be grouped into coarse or fine soils. The grain sizes associated with coarse and fine soils are illustrated in Figure 3.5. The basis for division into a coarse or fine soil is a 35 % fines content, that is a fine soil has > 35 % of grains finer than 0.06 mm and a coarse soil has < 35 % of grains finer than 0.06 mm (Burns *et al.* 2005). In the situation whereby a soft rock mass fits the criteria for a coarse soil, it will be described as such. Alternatively, if a soft rock mass meets the fine soil criteria, it will be described as a fine soil.












TYPE	COARSE								FINE		ORGANIC
	Boulders	Cobbles	Gravel			Sand			Silt	Clay	Organic Soil
			coarse	medium	fine	coarse	medium	fine			
Size Range (mm)	200	60	20	6	2	0.6	0.2	0.06	0.002	Refer to Section 2.3.5	
Graphic Symbol											

Figure 3.5 – Grain sizes associated with coarse and fine soils. Sourced from Burns *et al.* (2005).

Parameters used to describe coarse soils are presented in Appendix C and include particle size proportions, maximum particle size, grading, particle shape, particle weathering and strength, colour, relative density, structure, moisture condition, lithology, and any relative geological information (for example, parent rock or mineralogy).

Fine soils are described following the parameters presented in Appendix C and include particle size proportions, plasticity, colour, soil strength, structure, and moisture condition. The presence of any coarse material was described following the parameters for the description of coarse soils.

### 3.3.2.1 SAMPLING

Representative, undisturbed soft rock samples were collected from sites 74, 76, 109, 110 and 113 (Figure 3.1) according to the soil core method suggested by Chandler & Rogers (1980). Briefly, this involves cutting a horizontal ledge into

an exposure pit large enough to collect at least five cores. One by one, soil corers are pressed gently into the soil until the corer is flush at the soil surface, taking care not to compact the soil at all. The corers are then dug out of the soil and the sample ends trimmed so that they are flush with the corer, after which the corer and sample are wrapped tightly so as to prevent any moisture loss. Soil cores were used to determine bulk density and direct shear strength of soft rocks as discussed in Section 3.5.

In the event whereby a soft rock mass was too loosely packed and/or poorly sorted to allow for representative sampling via soil cores, alternative approaches were incorporated. For determining bulk density, the mass and approximate volume of 13 slightly cemented, intact samples was measured. Measuring an approximate volume required that an average of three means of each dimension be calculated. In all cases, the highest and lowest values were deleted for each lithology as specified by Franklin (1985), after which an average was calculated from the remaining values.

For determining direct shear strength, a methodology similar to that of Simoni & Houlsby (2006), who constructed artificial direct shear cores in the laboratory from samples of loose material. Direct shear methodology is presented in Section 3.5.2.

### **3.3.3 ROCK MASS CLASSIFICATION**

Having already selected representative exposures and measured rock mass strength, rock mass classification is the final stage in describing a rock mass. Rock mass classification schemes seek to assign numerical values to properties of a rock mass considered likely to influence its behaviour, and to combine these individual values into one overall classification rating for the rock mass (Brady & Brown 2004). The reader is directed to Chapter 2 for a discussion of rock mass classification schemes in general. Those classification schemes employed in this study (namely the RQD, RMR and GSI) are also discussed in Chapter 2.

What will be noted here is that rock mass classification schemes are designed for the classification of fractured rock masses. The applicability of these schemes to

soft rock masses is therefore limited by the fact that soft rock masses do not contain a sufficient amount of discontinuities to make the classification scheme valid.

Rock mass classifications were undertaken at locations 12, 26, 33, 40 and 52 (Figure 3.1).

### **3.4 LABORATORY WORK: HARD ROCKS**

#### **3.4.1 BULK DENSITY AND POROSITY**

The unit weight of a rock mass is required when modelling slope stability. Unit weight can be calculated from a known bulk density. Hard rock bulk density and porosity was determined using the saturation and buoyancy technique of Brown (1981). While porosity of the hard rocks is not required for modelling, it is simple to calculate from the saturation and buoyancy method and offers an additional perspective into the nature of each rock mass. Volumes of hard rock samples were measured using the approach mentioned in Section 3.3.2.1 for soft rocks. In all cases, the highest and lowest values were deleted for each lithology as specified by Franklin (1985), after which an average was calculated from the remaining values.

#### **3.4.2 POINT LOAD TEST**

The point load test is an index test that is used to help determine the intact strength of rock masses; a parameter crucial for stability modelling. The point load test often replaces the uniaxial compressive strength (UCS) test as when properly conducted it is as reliable as the UCS test but much quicker to carry out (Kahraman 2001). The Point Load Test is designed to be carried out on cylindrical, irregular lump or cut blocks samples; cut blocks were tested in this study using an Engineering Laboratory Equipment Limited point load tester (model P14A). The structure of cut blocks and point load methodology followed that stated by Franklin (1985).

The failure load  $P$  was recorded for each point load sample and the uncorrected and corrected point load strength calculated as shown in Appendix D. In all cases,

the highest and lowest point load values were deleted for each lithology and the average of the remaining values calculated as specified by Franklin (1985).

### 3.4.3 DISCONTINUITY ORIENTATION

Discontinuity orientations are best represented using stereonet analysis whereby orientations of discontinuities are plotted as poles on a reference sphere. Based on discontinuity orientations collected from scanline surveys, the stereographic projection program RockWorks2002 was used to construct stereonets with a Schmidt Equal Area Projection. Contouring the poles determined clusters of high pole concentration. By averaging these clusters, the orientation of major discontinuity sets could be determined.

The number of discontinuities in a set can be adjusted to account for the relative orientation of the discontinuity with respect to the rock face as follows:

$$N = \frac{N_{app}}{\sin \theta} \quad (3.1)$$

Where  $N$  is the adjusted number of discontinuities,  $N_{app}$  is the measured number of discontinuities, and  $\theta$  is the angle between the rock face and strike of the discontinuity set.

Equation 3.1 was used to calculate an appropriate increase in the number of discontinuities in each set to more accurately represent the population of discontinuities.

### 3.4.4 ROCLAB™

A difficulty when modelling rock masses numerically is selection of rock mass property data. Galena™ requires all rock mass material properties to be in the form of one of two failure criteria (that is, entirely Mohr-Coulomb or Hoek-Brown). In a situation such as that at Putauaki where both soft rock (represented by the Mohr-Coulomb failure criterion) and hard rock (represented by the Hoek-Brown failure criterion) exist, rock mass property data needs to be converted. The rock mass strength analysis program RocLab™ (Rocscience 2006) helps resolve

this issue by allowing the user to easily obtain Hoek-Brown and equivalent Mohr-Coulomb parameters based on the input parameters GSI, UCS, the material constant  $m_i$ , and D.

A value representing the GSI of each rock mass was obtained from sites 12, 26, 33, 40 and 52 (Figure 3.1). Selection of values to represent UCS,  $m_i$  and D is discussed in detail in Chapter 5.

### **3.5 LABORATORY WORK: SOFT ROCKS**

#### **3.5.1 BULK DENSITY**

Bulk densities of soft rocks were calculated using the simple equation:

$$\rho = \frac{\text{mass of soil}}{\text{volume of soil}} (\text{kg m}^3) \quad (3.2)$$

In all cases, the highest and lowest values were deleted for each lithology as specified by Franklin (1985), after which an average was calculated from the remaining values.

#### **3.5.2 DIRECT SHEAR STRENGTH TEST**

Measuring direct shear strength using the shear box is a simple technique which allows determination of the intact strength of a soil, or in this case soft rock. Intact strength of soft rocks is represented by the Mohr-Coulomb parameters cohesion ( $c$ ) and friction angle ( $\phi$ ). The test involves inserting the sample into the shear box sample holder which is divided horizontally, after which a gradually increasing horizontal force is applied to the lower part of the holder until the sample shears. Samples were tested in an undrained, unconsolidated state using a Wykeham Farrance Engineering Limited direct shear machine (model 25000) following the method suggested by Chandler & Rogers (1980).

##### **3.5.2.1 PREPARATION OF THE SAMPLE**

In the situation where representative undisturbed soft rock samples were able to be collected using soil cores, these samples were inserted directly into the shear box. However, those soft rocks which were too loosely packed and/or poorly

sorted to allow for representative sampling via soil cores, required that direct shear cores be manually constructed from loose field samples. This raises the question as to what grain sizes should the reconstructed core consist of to be representative of the soft rock mass? The depth of a direct shear sample collected in the field is approximately 20 mm. Thus a sample with grains coarser than 10 mm (half of the sample depth) would intersect the shear plane, potentially affecting measured peak shear stress. For this reason, artificial cores were constructed from the proportion of the sample with a grain size  $< 8$  mm (8 mm being the equivalent of  $-4 \phi$ ; the closest sieve size finer than 10 mm based on the Udden-Wentworth grain size scale).

Each artificial core was constructed so as to give a bulk density accurate to within 1 % of that measured for the equivalent soft rock mass.

### 3.5.2.2 MAGNITUDE OF THE NORMAL LOAD

A normal stress must be applied to the sample via dead weights to reflect *in situ* overburden stress of the material in question. The method for calculating the magnitude of normal stress is presented in Appendix E.

### 3.5.2.3 CALCULATING COHESION AND FRICTION ANGLE

Throughout the duration of the direct shear test, readings from the vertical and proving ring dials were recorded at the regular interval of 30 seconds. Readings were taken for the entirety of the test until the shear box butted up against the carrier. At a shearing rate of  $0.183 \text{ mm min}^{-1}$ , this was equivalent to approximately 50 minutes per sample.

To calculate  $c$  and  $\phi$ , a curve of the shear stress versus shear displacement was plotted for each sample and the peak shear stress read from this curve. These values of peak shear stress were then plotted on a graph of peak shear stress versus normal stress, and a best-fit line fitted to the points. The value of  $c$  is given by the point at which the best-fit line intercepts the y-axis, while  $\phi$  is determined from the slope of the best-fit line.

### 3.6 SUMMARY

This chapter described how ArcGIS™ was used to produce spatially referenced maps of the study area. Geomorphic description and mapping of the study area was undertaken using stereoscope analysis and field reconnaissance, after which geomorphic features identified were digitised onto maps using GIS. It was explained how descriptions of rock masses involved locating representative exposures, measuring rock mass strength and classifying the rock mass.

Rock mass descriptions were incorporated for both hard rocks and soft rocks. Measurement of hard rock mass strength required description of the rock mass as a whole, scanline surveys (describing discontinuity condition), and rock mass classification. A general lack of discontinuities in the soft rocks meant rock mass strength was measured solely using descriptions of the rock mass as a whole. Samples for laboratory strength testing were collected in the form of fallen blocks (in the case of hard rock masses) or soil cores/bagged loose material (in the case of soft rock masses).

Geotechnical properties of hard and soft rock masses were measured in the laboratory. In the case of hard rocks, bulk density and porosity were measured, and point load tests were carried out allowing calculation of equivalent UCS. The orientation of major discontinuity sets was determined using stereonet analysis and the number of discontinuities in each set adjusted to allow for sampling bias. Soft rock bulk density was determined and intact strength measured using direct shear strength tests on soil cores. In the situation whereby soft rock samples were in the form of bagged loose material, artificial cores were constructed.

# CHAPTER 4

# ***GEOMORPHOLOGY AND GEOLOGY***

---

## **4.1 INTRODUCTION**

The geomorphology of Putauaki and the surrounding landscape is discussed in this chapter. Field mapping and description of major geomorphological features identifies slope angles, valley and ridge form, landscape dissection intensity, alluvial channels and breaks in slope.

Mention is made of how rock exposures on Putauaki are selected based on accessibility and how representative they are of the rock mass as a whole. Descriptions of rock mass characteristics are undertaken for each exposure. These characteristics are then used as a basis for defining different lithotechnical units. For each lithotechnical unit defined, an in-depth rock mass description will be presented.

## **4.2 GEOMORPHOLOGY**

Lying approximately 80 m a.s.l, the strongly dissected landscape surrounding Putauaki represents the eroded upper surface of the  $280 \pm 30$  ka Matahina Ignimbrite (Burt *et al.* 1998) (Figure 4.1). A strong south-west to north-east tendency is apparent within the dissection pattern of the landscape (Figure 4.1). Valleys are commonly sharp and relatively narrow in nature. To the north-west of Putauaki, the Tarawera River valley is deeply incised into the landscape, and includes the present flow path of the Tarawera River (Figure 4.1). Kawerau Township is located within this river valley.

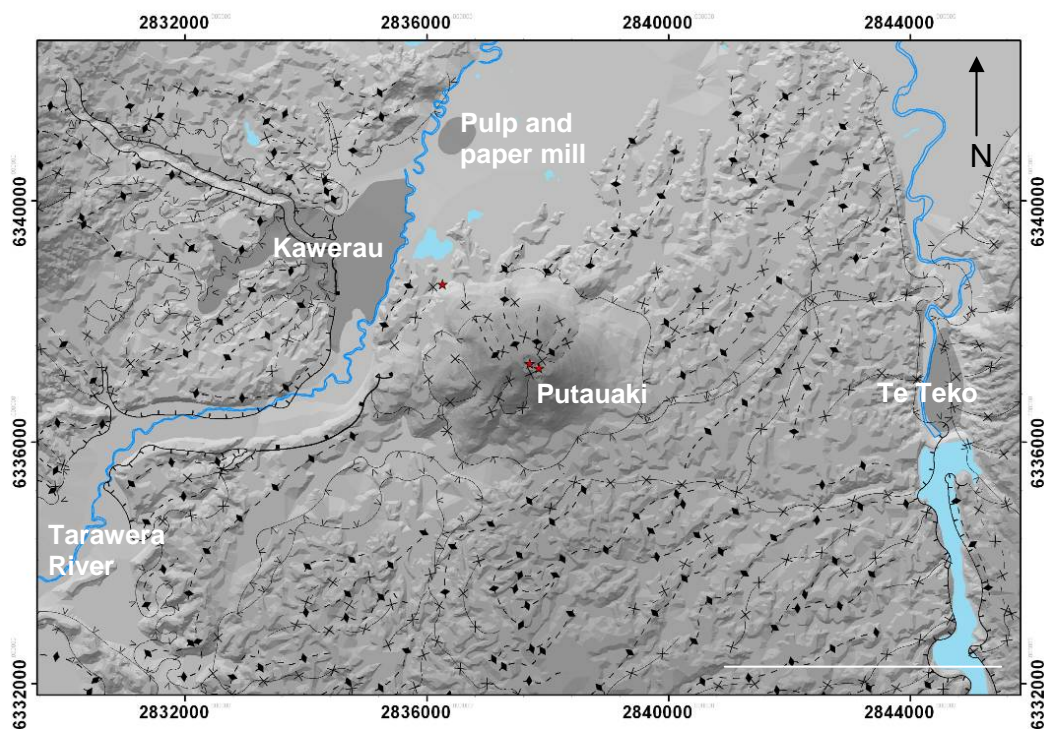
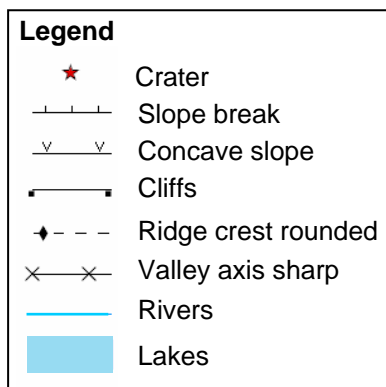


Figure 4.1 – Major geomorphological features of Putauaki and the surrounding landscape. Also shown are the Tarawera River, the townships of Kawerau and Te Teko, and the pulp and paper mill. White line represents 4 km. Geomorphological symbols from Cooke & Doornkamp (1990).



In plan view, Putauaki is a roughly circular feature (Figure 4.1), its circumference measuring approximately 10 km. Its volume has been reported as being approximately 1.61 km<sup>3</sup> (Duncan 1970). Putauaki consists of two primary features including Main Dome (approximately 6 ka) and Main Cone (approximately 4 ka) (Nairn 1995) (Figure 4.2). The summit of Main Cone is a prominent feature standing approximately 820 m a.s.l., thus protruding some 740 m above the surrounding landscape. Main Cone displays an average slope angle of 36° nearer to its summit, which lessens to approximately 32° closer to the base of the cone (Figure 4.2). According to Siebert (1984), both these angles coincide well with the average slope angles of volcanoes which have undergone major

slope failure in the past. However, a lack of any evidence of landslide deposits on the landscape surrounding the volcano indicates that Putauaki has not undergone volcanic collapse. The flanks of Main Cone show little evidence of significant erosion (Figure 4.2). The lower regions of the north, south and west flanks portray an irregular topography of poorly developed young ridges and valleys while the east flank is characterised by a non-dissected, draped appearance (Figure 4.2). A step-like morphology is apparent on the north flank of Main Cone, interpreted as the result of successive lava flows travelling progressively shorter distances (Duncan 1970) (Figure 4.2). Drainage channels cutting through the vegetation appear common on Putauaki, particularly on the north flank; however, the observation of flowing surface waters anywhere on the volcano is extremely rare.

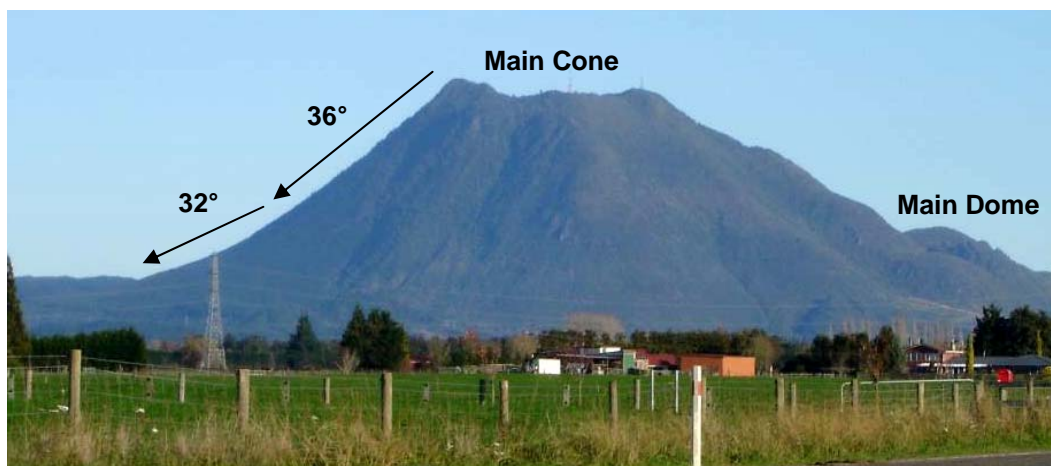


Figure 4.2 – Putauaki viewed from the north-west. Putauaki is a prominent feature on an otherwise subdued landscape. Arrows represent slope angles of Main Cone. The flanks of Putauaki show little evidence of significant erosion. The irregular topography of rounded ridges and poorly developed valleys attest to the young age of Putauaki. Note the non-dissected draped appearance of the eastern (left in figure) flank. A step-like morphology is apparent on the western (right in figure) flank. The summit of Main Dome can be seen in the background behind the western flank.

Two small craters are present at the summit of Main Cone (Figure 4.1). Explosive activity associated with the formation of these craters (and other eruptives) must have been minor because no associated pyroclastic deposits have been found (Nairn 1995; Carol 1998). Main Crater is the most south-east of the two, and with an area of  $0.028 \text{ km}^2$  is the largest. The walls of Main Crater maintain slope angles approximating  $30^\circ$  and a crater depth of at least 40 m is apparent.

However, dense vegetation within Main Crater restricts access. Small (20 m<sup>2</sup>) rock falls are evident on the interior of the crater walls. Secondary Crater is located approximately 200 m to the north-west of Main Crater. A cool water lake is a permanent feature of this crater, the lake being the only evidence of permanent water on the volcano. The level of the lake is seen to vary by approximately 40 cm on a seasonal basis. Secondary Crater is also vegetated; however, its walls are more subdued showing angles of approximately 17°. Secondary Crater is approximately 20 m deep, the true depth of the crater being obscured by the crater lake.

Sitting at the base of the western flank of Main Cone is perhaps one of the most conspicuous features of Putauaki, Main Dome (Figure 4.2). The summit of Main Dome reaches approximately 420 m a.s.l. Slope angles are more subdued than those of Main Cone, maintaining angles of approximately 24°. Drainage channels and craters are not evident on Main Dome, nor is there any evidence of dissection of its flanks. While Main Dome is a separate feature from Main Cone, the reference to Putauaki in this study is understood to include both features. Reference to either one of the structures will be made using the title Main Cone or Main Dome.

### **4.3 ROCK MASS DESCRIPTION**

Cas & Wright (1987) described stratovolcanoes as typically consisting of up to 80% volcanoclastic (or fragmented volcanic rock) material with only a small proportion of lava flows interspersed. Putauaki; however, does not follow this pattern, with predominantly coherent lavas making up the volcano. The lack of volcanoclastic material may be due to the quiescent eruptive history of Putauaki (Nairn 1995).

Rock mass descriptions were undertaken at a total of 32 sites. The distribution of these sites is illustrated in Figure 4.3. As described in detail in Section 3.3, selection and subsequent description of rock mass exposures was a time consuming process. Many months of fieldwork were required to navigate the dangers posed by the steep flanks and dense vegetation in the search for representative exposures. Once located and provided access was possible, in-

depth descriptions of the rock mass as a whole, as well as descriptions of discontinuity condition, were undertaken. Sampling of the rock mass was also necessary.

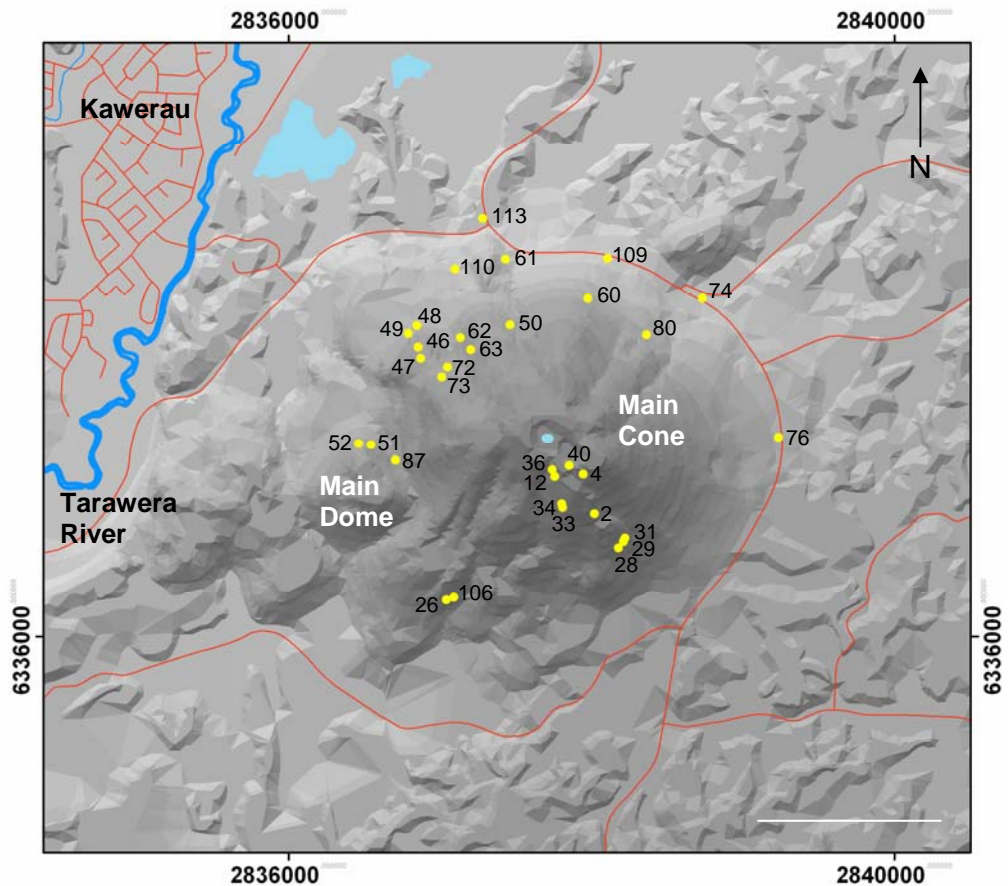
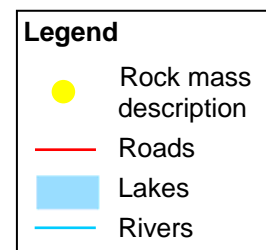


Figure 4.3 – DEM showing location of rock mass description sites (yellow markers). Numbers indicate site numbers. White bar represents 1 km.



Based upon the method used to sample rock masses at each of the sites shown in Figure 4.3, it is possible to divide the rock masses of Putauaki into two broad groups; hard rocks (those rock masses indurated to the point that intact samples can be collected in the form of fallen blocks), and soft rocks (those rock masses that require samples to be collected via a soil core or bag of loose material). Further subdivision of the rock masses at each site is possible based on

description of rock mass characteristics. Six separate lithotechnical units are identified including four hard rock units (indurated andesite, scoriaceous andesite, altered andesite, and indurated dacite) and two soft rock units (block and ash flow, and Matahina Ignimbrite).

Figure 4.4 illustrates the stratigraphical succession, along with approximate ages, of the six lithotechnical units identified on Putauaki. The  $280 \pm 30$  ka Matahina Ignimbrite (Burt *et al.* 1998) is the oldest lithotechnical unit identified. The Mamaku Tephra, dated at  $C^{14} 7250 \pm 20 C^{14}$  yr BP (Hajdas *et al.* 2006) underlies the next oldest lithotechnical unit, indurated dacite, which was described by Nairn (1995) to be approximately 6 ka. The Whakatane Tephra dated at  $C^{14} 4830 \pm 20 C^{14}$  yr BP (Hajdas *et al.* 2006) marks the division between indurated dacite and the andesitic units, the andesitic units described by Nairn (1995) to be approximately 4 ka. The block and ash flow, described by Carol (1998) to be  $C^{14} 3115 \pm 35 C^{14}$  yr BP, is the youngest lithotechnical unit identified on Putauaki. The Waimihia Tephra dated at  $C^{14} 3230 \pm 20 C^{14}$  yr BP (Hajdas *et al.* 2006), separates the block and ash flow from the underlying andesitic units of this study.

Lithotechnical unit	Years B.P.	Tephra
		0
Block and ash flow	3115 +/- 35	
		3232 +/- 20
Indurated andesite Scoriaceous andesite Altered andesite	4000 ?	Waimihia Tephra
		4830 +/- 20
Indurated dacite	6000 ?	Whakatane Tephra
		7250 +/- 20
Matahina Ignimbrite	280,000 +/- 30	Mamaku Tephra

Figure 4.4 – Schematic illustrating inferred stratigraphy and ages of lithotechnical units defined on Putauaki. Andesitic units are all approximately 4 ka.

The remainder of this chapter will provide detailed rock mass descriptions for each lithotechnical unit. While at times definitions of rock mass description

terminology will be provided in the text (for example ‘wide’ aperture or > 10 mm), the reader is referred to Appendices A and C for a complete definition of all rock mass description terms used.

### 4.3.1 ROCK MASS DESCRIPTION OF HARD ROCKS

Four hard rock lithotechnical units were identified on Putauaki. Rock mass characteristics for each hard rock unit are presented in Table 4.1.

Table 4.1 – Rock mass characteristics of hard rock lithotechnical units. The reader is directed to Appendix F for a complete copy of the rock mass description for each hard rock unit.

<b>Indurated andesite.</b> Described at sites: 12, 26, 28, 29, 31, 34, 36, 46, 47, 48, 49, 50, 60, 61, 62, 63, 72, 73, 80, 87, 106	
Rock	Slightly to moderately weathered, dark greyish black, massive, phaneritic porphyritic, medium strong ANDESITE
Joints	Joints widely spaced, medium to very low persistence, joint surfaces smooth and undulating and slightly weathered. Joints either very tight or open to wide. Unfilled joints dry with no evidence of flow, filled joints damp with no free water. Three joint sets plus random joints produce medium, blocky shaped blocks.
Infill	Sandy, fine to coarse GRAVEL with a trace of silt, dark grey, homogenous. Very strong, loosely packed particles, dry, well graded. Maximum particle size 60 mm. Andesitic gravel angular to sub-angular, slightly weathered. Sand fine to coarse.
<b>Scoriaceous andesite.</b> Described at sites: 2, 33	
Rock	Moderately weathered, dark pinkish grey, massive, phaneritic, porphyritic, weak ANDESITE.
Joints	Joints very widely spaced, high persistence, joint surfaces rough and stepped and moderately weathered. Joints either extremely wide or wide. Unfilled joints damp but no free water. Three joint sets plus random joints produce very large, tabular shaped blocks.
Infill	Sandy, fine to medium GRAVEL with some silt, dark reddish brown, homogenous. Weak, loosely packed particles, moist, well graded. Maximum particle size 20 mm. Andesitic gravel angular, moderately weathered. Sand fine to coarse. Silt slightly plastic.
<b>Altered andesite.</b> Described at sites: 4, 40	
Rock	Highly weathered, light greyish red, coarse slaty fabric, phaneritic, porphyritic, weak ANDESITE.
Joints	Joints moderately spaced, low persistence, joint surfaces rough and stepped and highly weathered. Joints wide. Unfilled joints dry with no evidence of flow. Three joint sets plus random joints produce medium, tabular shaped blocks.
Infill	Sandy, fine to coarse GRAVEL with minor cobbles, dark brownish red, homogenous. Very weak, loosely packed particles, dry, well graded. Maximum particle size 100 mm. Andesitic gravel angular to sub-angular, highly weathered. Sand fine to coarse. Cobbles angular, highly weathered.
<b>Indurated dacite.</b> Described at sites: 51, 52	
Rock	Slightly weathered, light grey, massive, phaneritic, porphyritic, strong DACITE.
Joints	Joints widely spaced, medium persistence, joint surfaces smooth and undulating and slightly weathered. Joints wide to very wide. Unfilled joints dry with no evidence of flow. Three joint sets plus random joints produce very large, tabular shaped blocks.
Infill	Sandy, fine to coarse GRAVEL with a trace of silt, light grey, homogenous. Very strong, loosely packed particles, dry, well graded. Maximum particle size 50 mm. Dacitic gravel angular to sub-angular, slightly weathered. Sand fine to coarse.

Rock mass description of the hard rock units followed the New Zealand Geotechnical Society guidelines for the field description of rock (Burns *et al.* 2005) as discussed in Chapter 3. This section will in turn describe each hard rock mass.

All hard rock lithotechnical units are described as phaneritic, with a strongly crystalline porphyritic texture. Phenocrysts range from coarse (2 – 60 mm) to medium (60  $\mu$ m – 2 mm) grain sizes. The ratio of coarse to medium grain sizes for a typical hard rock mass was approximately 25%:75%.

#### **4.3.1.1 INDURATED ANDESITE**

Exposures of indurated andesite are present on the northern, southern and western flanks of Main Cone (sites 50, 106 and 49 respectively). Indurated andesite is presumed to underlie the block and ash flow on the eastern flank. Field strengths approximated medium strong; however, some exposures exhibited strong field strengths (site 50). Colour is generally a variation of dark grey. Some sites show a slight pinkish surface tinge (sites 28 and 29) presumed to be the result of oxidation (Carol 1998) (Figure 4.5). Indurated andesite is slightly weathered; though some exposures did exhibit moderate weathering (sites 62 and 63). Often, indurated andesite is seen to exhibit a moderately thick (approximately 40 mm) scoriaceous surface that is comparable to that of scoriaceous andesite (site 34) (Figure 4.5). It is important not to confuse this type of indurated andesite with contrasting scoriaceous andesite, which maintains a scoriaceous texture throughout the rock mass. The majority of exposures of indurated andesite are described as massive, lacking any indication of a fabric (fabric defined here as being < 100 mm thick). A partially slaty habit (too coarse to be categorised as a fabric) is observed at some sites (sites 29, 46, 62) (Figure 4.6).

Discontinuity spacing is typically wide (0.6 – 2 m); however, sites 12, 28, 29 and 60 showed moderate spacing (0.2 – 0.6 m). Discontinuity spacing less than 0.2 m is uncommon. Discontinuities appear relaxed, with apertures regularly exceeding 10 mm (wide aperture). At sites 29 and 80 apertures exceeded 100 mm (extremely wide) (Figure 4.6). Discontinuity persistence consistently measured < 10 m (medium persistence) but this is in part due to vegetation around the

outcrops restricting observations over greater distances. Discontinuity surfaces are generally smooth and undulating. Discontinuity walls are clean and show little evidence of weathering (for example rust staining) exhibiting a similar intact strength and dark grey colour to that of unweathered indurated andesite.

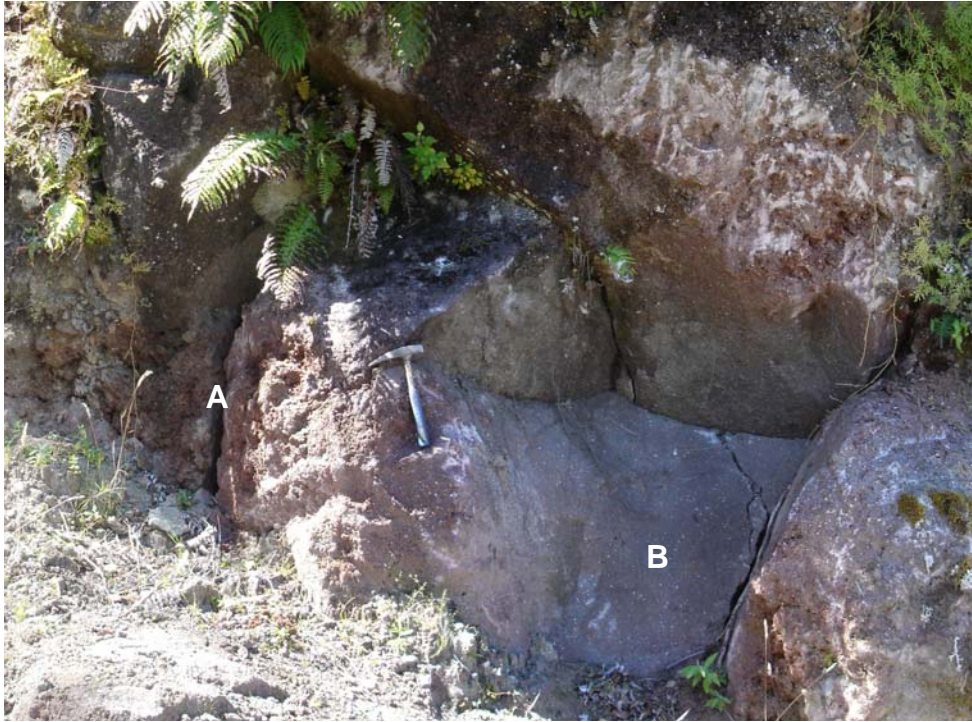


Figure 4.5 – Indurated andesite outcrop exhibiting a scoriaceous surface structure (indicated by ‘A’) that is absent deeper within the rock mass. In the above a figure a loose block has dislodged (indicated by ‘B’) exposing the non-scoriaceous interior of this rock mass. The pinkish tinge of this unit is presumed to be the result of oxidation. Photo taken at site 34. Geological hammer for scale.

Discontinuity infill was rare; infill that was observed comprised predominantly loosely packed, fine to coarse andesitic gravel with a subordinate (20 – 50 %) fraction of fine sand and traces (< 5 %) of silt (sites 80 and 87). Gravel sized constituents were strong (broken by a hammer blow). As a result of the wide aperture of discontinuities, as well as the coarse nature of the infill, moisture drains freely, causing discontinuities to be normally dry. However, where outcrops are under vegetative shelter, infill is seen to be damp. Free water is not associated with this rock mass.

Indurated andesite is approached in this study as being approximately 4 ka, intermediate in age between indurated dacite and the block and ash flow (Figure 4.4).



Figure 4.6 – Indurated andesite outcrop exhibiting wide discontinuity spacing. The relaxed state of the discontinuities produces some extremely wide apertures as seen in the upper right of the figure where shrubbery is growing within the discontinuity (indicated by ‘A’). Note the slaty habit of the indurated andesite displayed nearer the base of the outcrop (indicated by ‘B’). Photo taken at site 29. White bar represents 1 m.

#### 4.3.1.2 SCORIACEOUS ANDESITE

Exposures of scoriaceous andesite are present on the upper extent of the southern flank of Main Cone (sites 2 and 33). It is likely that this unit represents an outer facies of an andesitic lava flow which upon cooling was subsequently brecciated by the still hot and flowing inner facies, resulting in a scoriaceous texture (Figure 4.7). Weak field strengths and a strong pinkish grey colour are both characteristic of this unit. Scoriaceous andesite is moderately weathered.

In a similar fashion to indurated andesite, the discontinuity spacing and aperture of scoriaceous andesite exceeds wide. Discontinuity persistence of the scoriaceous andesite is high (10 – 20 m), the highest of all the hard rock units.

Discontinuity surfaces are rough and stepped (reflecting the scoriaceous texture of this unit), and moderately weathered. Dominant discontinuity sets are obvious at the outcrop scale; however, the scoriaceous texture of this rock mass, along with the sub-canopy location and associated blankets of moss-like vegetation, mean a clear view of minor discontinuities is difficult (Figure 4.8).



Figure 4.7 – Scoriaceous andesite outcrop exhibiting a scoriaceous texture. Photo taken at site 2. Key for scale.

Discontinuity infill as described at site 33 consists predominantly of loosely packed, fine to medium andesitic gravel with some (12 – 20 %) silt. Gravel sized constituents were weak (able to be broken with fingers). The sub-canopy location of the scoriaceous andesite allows for consistently damp infill irrespective of recent rainfall, and also gives the silt fraction of the infill a readily mouldable habit. Free water in the discontinuities was not observed.

Open cavities, or tomos (Figure 4.9), averaging 1 m across are very common for scoriaceous andesite (site 2). Scoriaceous cobbles and boulders lining the sidewalls and bases of these tomos is evidence of an origin attaining to the internal collapse of a large void. Commonly hidden beneath a carpet of forest

floor detritus, the full extent of these tomos is unknown. Three large scale tomos were observed within a 100 m radius of site 33. They were not observed elsewhere. These large tomos are seen to occur within semi-linear depressions (or small valleys) showing widths of up to 15 m, lengths in excess of 50 m and vertical sidewalls up to 20 m (Figure 4.8). Large tomos were not observed at any other site.



Figure 4.8 – Discontinuity sets in the scoriaceous andesite. Major discontinuity sets are very apparent; however, the sub-canopy location and associated blankets of moss-like vegetation mean a clean view of minor discontinuities is difficult. Note the canyon-like location of the outcrop. Photo taken at site 33. Safety helmet for scale.

Representing an andesitic lava flow, scoriaceous andesite is suggested to be of similar age to that of indurated andesite.

#### 4.3.1.3 ALTERED ANDESITE

Altered andesite is located in close proximity to the crater rim of Main Cone (sites 4 and 40). Exposures of altered andesite are rare, observations being made only

on the southern and eastern rim of Main Crater. It is unknown as to whether altered andesite or an equivalent deposit is present at Secondary Crater. If altered andesite is present at Secondary Crater, the existence of a crater lake suggests the possibility that this unit possesses a lower permeability than the other hard rock units. A greyish red colour is indicative of this unit, as well as weak field strength; a sample of altered andesite was easily disaggregated into finer components by hand (Figure 4.10). The altered andesite is strongly weathered. The close proximity of this unit to the volcanic crater, along with its low field strength and red colour, suggests the possibility that this unit has undergone some form of alteration associated with volcanic activity within the central conduit.



Figure 4.9 – A tomo in the scoriaceous andesite. These cavities are a common feature of the scoriaceous andesite, thought to represent internal collapse of voids within the rock mass. Forest detritus commonly obstructs the full extent of these cavities. Photo taken at site 2. Silva compass for scale.

Discontinuities are moderately spaced, show a low persistence (1 – 3 m), and aperture is wide. These characteristics allow for small cobble sized (60 – 200 mm) rock fragments to readily dislodge. Discontinuity surfaces are rough and stepped, and strongly weathered. Infill is weak, loosely packed, dry, and consists of fine to coarse gravel sized constituents with minor (5 – 12 %) cobbles.

The age of the altered andesite is suggested to be similar to that of the indurated andesite.



Figure 4.10 – Altered andesite outcrop exhibiting a readily disaggregated nature. The nature of this lithotechnical unit is evidence of its weak field strength. Weathered surfaces of the altered andesite appear grey, while freshly exposed surfaces appear reddish (as indicated by ‘A’). Photo taken at site 40. Key for scale.

#### 4.3.1.4 INDURATED DACITE

Indurated dacite is the only lithotechnical unit that is absent from Main Cone. However, indurated dacite is the sole constituent of Main Dome. The light grey colour of indurated dacite (relative to the darker colours associated with the andesitic units) makes for easy field identification (Figure 4.11). Field strength is strong, the highest of all hard rock units. Indurated dacite is slightly weathered.

Discontinuities are widely spaced, display medium persistence and appear very relaxed with apertures reaching very wide (1 – 10 cm) (Figure 4.12). Discontinuity surfaces are smooth and undulating, and moderately weathered. Discontinuity surfaces are dry and there is no evidence of water flow. Infill is rare in this unit. Infill observed was strong, fine to coarse gravel with a trace of silt (sites 51 and 52).

The age of the indurated dacite is approximately 6 ka (Nairn 1995). This unit most likely represents early volcanic activity from Putauaki.

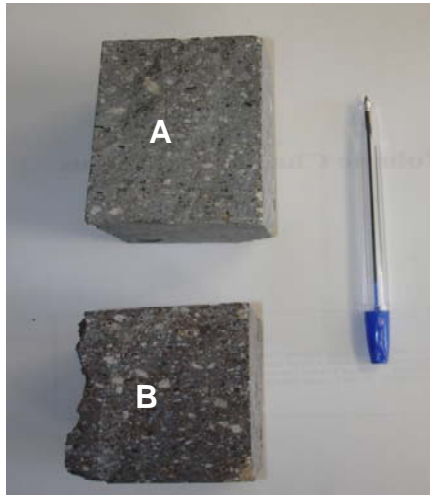


Figure 4.11 – (A) Light grey colour characteristic of the indurated dacite. (B) A sample of indurated andesite which exhibits a much darker colour. The relatively light colour of the indurated dacite aids field identification of this unit. Pen for scale.



Figure 4.12 – Indurated dacite outcrop exhibiting very wide discontinuity apertures (as shown by ‘A’ in the lower right of the above figure). Photo taken at site 52. Safety helmet for scale.

### 4.3.2 ROCK MASS DESCRIPTION OF SOFT ROCKS

Two soft rock lithotechnical units were identified on Putauaki. Rock mass characteristics of each soft rock unit are presented in Table 4.2. This section will in turn describe each soft rock mass.

Table 4.2 – Rock mass characteristics of soft rock lithotechnical units. The reader is directed to Appendix F for a complete copy of rock mass descriptions for soft rock unit.

<b>Block and ash flow.</b> Described at sites: 74, 76, 109, 110	
Coarse soil (entire deposit)	Sandy, gravelly and cobble rich with some boulders, light brownish grey, homogenous. Loosely packed, dry, well graded. Sand and gravel fine to coarse, angular to sub-angular, equidimensional, slightly weathered. Cobbles and boulders sub-rounded to sub-angular, slightly weathered. Matrix supported, monolithologic deposit consisting of indurated non-vesicular andesitic material.
Fine soil (matrix)	Sandy SILT with some gravel, light grey, homogenous. Stiff, dry, low plasticity.
<b>Matahina Ignimbrite.</b> Described at site: 113	
Fine soil	SILT with some sand and gravel, light greyish white, homogenous. Stiff, dry, low plasticity. Pumice maximum clast size < 70 mm (coarse pebble), well graded, (all similar sizes), sub-rounded to sub-angular, very weak, greyish white. Lithics maximum clast size < 15 mm (medium pebble), poorly graded (all similar sizes), sub-angular, strong, brownish black.
Rock	Slightly weathered, light greyish white, massive, aphanitic, very weak IGNIMBRITE.
Joints	No joints apparent

#### 4.3.2.1 BLOCK AND ASH FLOW

The block and ash flow is proposed to have originated from the collapse of a viscous lava dome extruded above the summit of Main Cone (Nairn 1995). The block and ash flow has been dated by Carol (1998) to be  $C^{14} 3115 \pm 35 C^{14}$  yr BP, making it the youngest lithotechnical unit identified on Putauaki. What appears to be two lobes of block and ash flow are present on Putauaki, the larger draping the eastern flank (sites 74, 76 and 109); while a secondary flow is present as a channelised deposit on the north-west flank (site 110). Both flow lobes are approached as one lithotechnical unit for the reason that they exhibit similar rock mass characteristics.

The block and ash flow deposits of Putauaki contain a multitude of clast sizes amongst a finer matrix. Rock mass description of the block and ash flow in its entirety followed the New Zealand Geotechnical Society guidelines for the field description of coarse soil (Burns *et al.* 2005), while description of the matrix followed similar guidelines, but for fine soils (Table 4.2).

The block and ash flow is very poorly sorted (Figure 4.13). Clasts range in size from fine sand to boulders; all clast sizes are present in similar proportions. The deposit is loosely packed, clasts able to be plucked out from the deposit if they

have not already dislodged independently (Figure 4.13). It is a monolithologic deposit consisting entirely of slightly weathered sub-angular to sub-rounded clasts of indurated andesite.



Figure 4.13 – Block and ash flow deposit. The block and ash flow is very poorly sorted containing constituents ranging in size from fine sand to boulders. The deposit is loosely packed, fallen blocks regularly littering the bases of outcrops. Blocks appear matrix supported. Photo taken at site 109. Geological hammer for scale.

The block and ash flow is described as matrix supported. While definitions of the grain size at which the matrix exists may vary, it is apparent from deposits that larger clasts are more often than not supported by the finer material (Figure 4.13). The matrix is of low plasticity while consisting predominantly of silt sized constituents with some medium gravel. The block to matrix ratio approximates 45%:55%.

#### **4.3.2.2 MATAHINA IGNIMBRITE**

The Matahina Ignimbrite is unique from the other lithotechnical units in the sense that it is unrelated to any volcanic activity originating from Putauaki. The Matahina Ignimbrite underlies Putauaki, thus playing a very important role in the

stability of the volcano. For this reason, Matahina Ignimbrite is included as a lithotechnical unit influential in the stability of Putauaki.

Rock mass description of the Matahina Ignimbrite initially followed the New Zealand Geotechnical Society guidelines for the field description of rock (Burns *et al.* 2005); however, a limited number of discontinuities within this unit meant this description was brief and uninformative. As an alternative, rock mass description followed similar guidelines, but for the field description of fine soil.

Field strength of the Matahina Ignimbrite is very weak. The deposit is slightly weathered; unweathered regions being only slightly stronger than those regions that are weathered. The Matahina Ignimbrite is light grey in colour and exhibits little evidence of discontinuities (Figure 4.14a). The predominant clast size is silt comprising approximately 70 % of the deposit. Strong, sub-angular, medium gravel-sized lithics and very weak, sub-angular, coarse gravel-sized pumice clasts comprise approximately 20 % of this soft rock unit (Figure 4.14b). The plasticity of the Matahina Ignimbrite is low and the structure is homogenous.

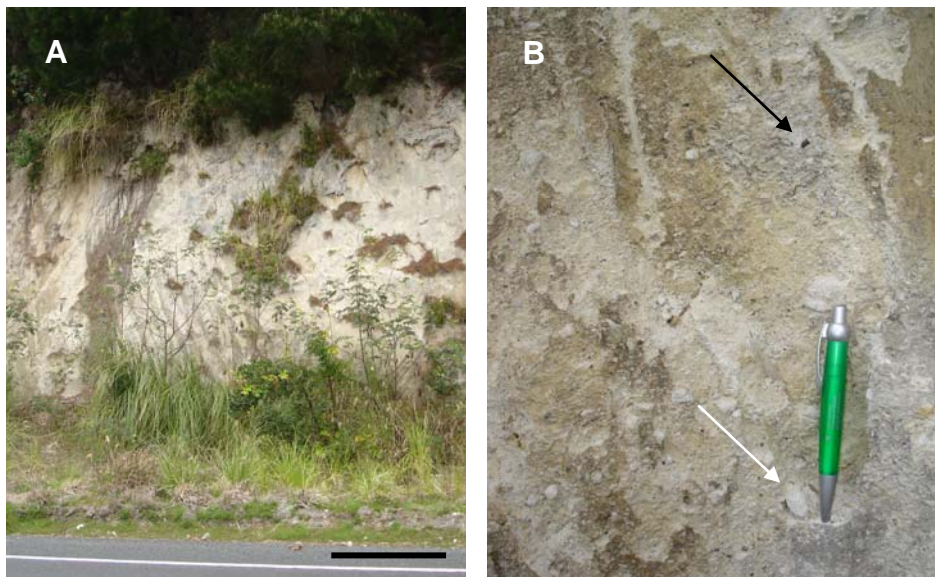


Figure 4.14 – (A) Matahina Ignimbrite outcrop. (B) Lithics (black arrow) and pumice clasts (white arrow) combined makeup approximately 20 % of the Matahina Ignimbrite. Black bar represents 2 m. Photo taken at site 113. Pen for scale.

### 4.4 DISTRIBUTION OF LITHOTECHNICAL UNITS

Based on rock mass descriptions at 32 sites, six lithotechnical units have been defined on Putauaki. Figure 4.3 shows the location of each rock mass description site. Correlating each lithotechnical unit to its associated description site helps define approximate boundaries of each unit. Rock mass descriptions also provided an understanding of the nature of each unit, which further aided the positioning of lithotechnical boundaries. Figure 4.15 illustrates the location and approximate boundaries of each lithotechnical unit as defined for this study.

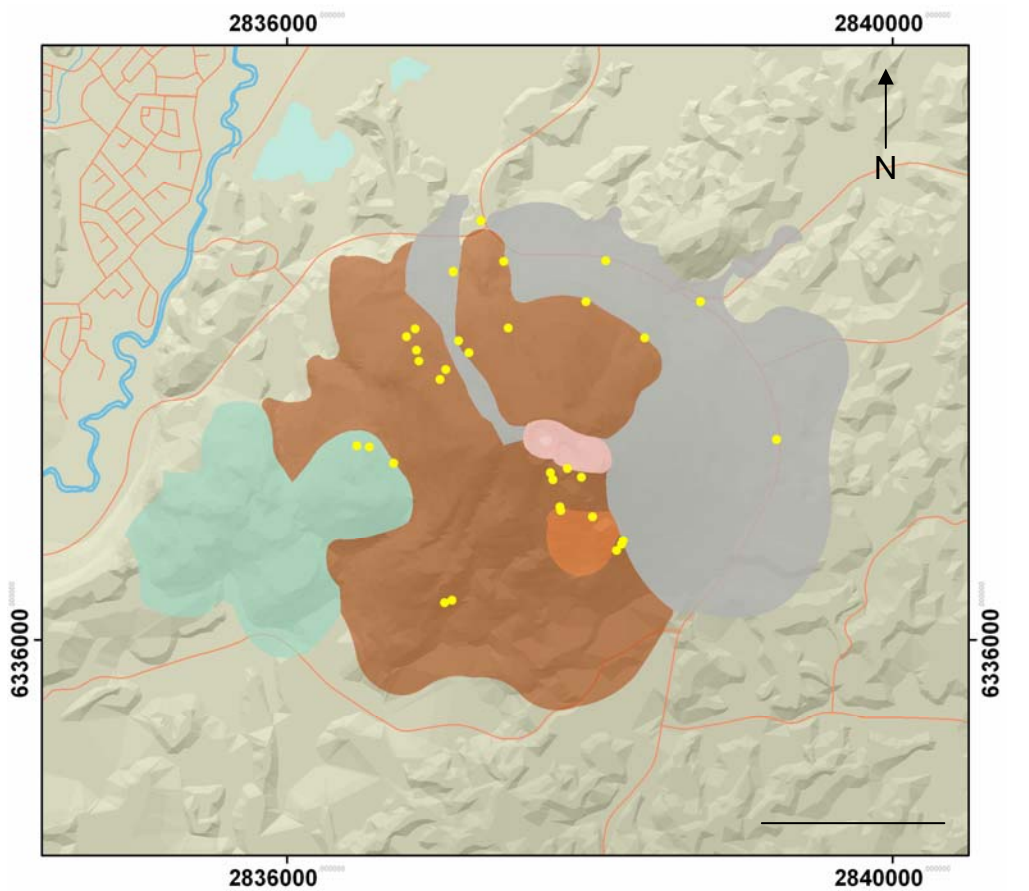
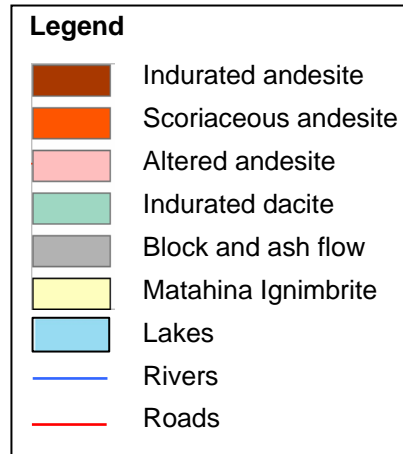


Figure 4.15 – DEM indicating location and approximate boundaries of each lithotechnical unit. Black line represents 1 km.



## 4.5 SUMMARY

Putauaki is seen to stand high above its surrounding landscape which is strongly dissected. Putauaki comprises two predominant features; the larger and younger Main Cone (the summit of which lies 820 m a.s.l., and flanks of which slope at angles up to 36°) and smaller and older Main Dome (the summit of which lies 420 m a.s.l. and flanks of which slope at 24°). Both features show little evidence of erosion or surface water.

Rock mass descriptions were carried out at a total of 32 sites on Putauaki. Based on sampling methodology, rock masses were divided into two groups; hard rocks (samples collected in the form of fallen blocks) and soft rocks (samples requiring collection via a soil corer or bag of loose sample). Description of the characteristics of each rock mass provided a foundation for defining six lithotechnical units including four hard rock units (indurated andesite, scoriaceous andesite, altered andesite, and indurated dacite) and two soft rock units (block and ash flow, and the Matahina Ignimbrite). Table 4.3 lists the sampling methodology and associated description site, along with typical rock mass characteristics of each lithotechnical unit. Correlation of each lithotechnical unit to its respective site location allowed approximate boundaries of each unit to be inferred (Figure 4.15).

Table 4.3 – Typical rock mass characteristics for each lithotechnical unit. Based on sampling methodology, rock masses may be initially divided into two groups: hard rocks or soft rocks. Refer Figure 4.4 for site locations. Refer Appendix F for a complete rock mass descriptions for each site.

Sampling method	Rock type	Site number	Key features of rock mass strength	Lithotechnical unit
Fallen block	Hard rock	12, 26, 28, 29, 31, 34, 36, 46, 47, 48, 49, 50, 60, 61, 62, 63, 72, 73, 80, 87, 106	Slightly weathered, dark grey, medium strong ANDESITE. Joints widely spaced, medium persistence, wide aperture, surfaces smooth and undulating and slightly weathered, no evidence of seepage. Infill sandy, fine to coarse GRAVEL, very strong, loosely packed, dry, angular, slightly weathered.	Indurated andesite
		2, 33	Moderately weathered, pinkish grey, weak ANDESITE. Joints widely spaced, high persistence, surfaces smooth and undulating and moderately weathered, wide aperture, no evidence of seepage. Infill sandy, fine to medium GRAVEL with some silt, weak, loosely packed, moist, angular, moderately weathered, silt slightly plastic.	Scoriaceous andesite
		4, 40	Highly weathered, light grey-red, weak ANDESITE. Joints moderately spaced, low persistence, surfaces rough and stepped and strongly weathered, wide aperture, no evidence of seepage. Infill sandy, fine to medium GRAVEL, minor cobbles, very weak, loosely packed, dry, angular highly weathered.	Altered andesite
		51, 52	Slightly weathered, light grey, strong DACITE. Joints widely spaced, medium persistence, surfaces smooth and undulating and slightly weathered, wide aperture, no evidence of seepage. Infill sandy, fine to coarse GRAVEL, very strong, loosely packed, dry, angular, slightly weathered.	Indurated dacite
Core	Soft rock	74, 76, 110, 113	Poorly sorted, sandy, gravelly and cobble rich with some boulders, light grey, loosely packed, dry, matrix supported, monolithologic consisting of indurated andesite.	Block and ash flow
		113	SILT with some gravel, light grey, dry, low plasticity. Pumice clasts < 70 mm (coarse pebble), sub-rounded, very weak. Lithics < 15 mm (medium pebble), sub-angular, strong, brownish black.	Matahina Ignimbrite

# CHAPTER 5

# *GEOTECHNICAL PROPERTIES*

---

## **5.1 INTRODUCTION**

Geotechnical data obtained for each lithotechnical unit is presented and discussed in the following chapter; the aim of this chapter is to determine geotechnical properties required to aid interpretation of the stability of Putauaki. For the hard rocks this includes measurement of intact properties and discontinuity characteristics, and classification of the rock mass using the RMR and GSI. Input variables GSI, UCS,  $m_i$ , and D are defined to enable calculation of Hoek-Brown and equivalent Mohr-Coulomb parameters using RocLab<sup>TM</sup>. For the soft rocks, unit weight and measured Mohr-Coulomb parameters are presented.

## **5.2 HARD ROCKS**

### **5.2.1 UNIT WEIGHT AND POROSITY**

Table 5.1 shows unit weights calculated for each hard rock unit. A summary of the unit weights of jointed lavas presented by Moon *et al.* (2005) shows unit weights to range from 20.6 – 27.5 kN m<sup>-3</sup>. The two indurated units coincide well with the lower portion of this range. However, unit weights of the scoriaceous and altered andesite are much lower, comparable to hydrothermally altered rock masses (Moon *et al.* 2005). While the scoriaceous andesite does not appear to be altered, its low unit weight is most likely a result of the high porosity associated with this unit. Porosities measured in this study are typically higher than those reported by others for andesitic lithologies. For example, Oguchi & Matsukura reported porosities ranging from 2 – 10 % for weathered andesites in Nasuno-gahara, Japan (1999), while Özsan & Akin (2002) reported porosities ranging from 3.3 – 4.1 % for andesites at the Uruş Dam, Turkey.

Table 5.1 – Unit weight and porosity of the hard rock units. Values are presented as an average  $\pm$  standard error. Refer Appendix G for complete unit weight and porosity data.

	<b>Indurated andesite</b>	<b>Indurated dacite</b>	<b>Scoriaceous andesite</b>	<b>Altered andesite</b>
Average unit weight ( $\text{kN m}^{-3}$ )	22.8 $\pm$ 0.2	23.39 $\pm$ 0.09	15 $\pm$ 1	16.9 $\pm$ 0.1
Average porosity (%)	11.1 $\pm$ 0.8	8.2 $\pm$ 0.2	27.3 $\pm$ 2.1	30.12 $\pm$ 0.7

## 5.2.2 INTACT STRENGTH

### 5.2.2.1 SCHMIDT HAMMER

Using the correlation method presented in Selby (1993), average Schmidt hammer rebound numbers ( $r$ ) for each hard rock were converted to UCS values (Table 5.2) based on their respective unit weights as presented in Table 5.1. The resulting UCS values for each unit appear very low for lithologies of this type, suggested UCS values for igneous rocks being at least 100 MPa. The fact that all the hard rock units show relatively low intact strengths can perhaps be expected taking into account their unit weights, which are seen to be less than (in the case of the scoriaceous and altered andesite), or equivalent to (in the case of the indurated andesite and dacite), the lower portion of unit weights for jointed lavas summarised by Moon *et al.* (2005) (Section 5.2.1). It is important to note here is the difficulty associated with correlating  $r$  with UCS. The likelihood of any one correlation method being universal to many rock types, as well as accounting for the sensitivity of the Schmidt hammer to discontinuities, is very small (Selby 1993). While this limitation potentially makes the correlation unreliable, this method is sufficient for providing approximate estimations of the UCS of an intact rock.

Table 5.2 – UCS values of the hard rock units calculated from average  $r$  values. Calculation of UCS assumed unit weights from Table 5.1 and average  $r$  values provided below.  $r$  values are presented as an average  $\pm$  standard error. UCS values are presented as an average  $\pm$  the level of accuracy possible from the correlation method of Selby (1993). Refer Appendix H for complete Schmidt hammer data.

	<b>Indurated andesite</b>	<b>Indurated dacite</b>	<b>Scoriaceous andesite</b>	<b>Altered andesite</b>
Average $r$ value	41.2 $\pm$ 0.6	51.2 $\pm$ 0.2	18.4 $\pm$ 0.2	16.6 $\pm$ 0.4
UCS (MPa)	62 $\pm$ 3	95 $\pm$ 3	15 $\pm$ 3	15 $\pm$ 3

### 5.2.2.2 UNIAXIAL COMPRESSIVE STRENGTH

The average point load strength index ( $I_{s50}$ ) (calculated from point load tests) for each intact hard rock is presented in Table 5.3. Conversion of the  $I_{s50}$  to a UCS requires multiplication by a point load conversion factor (PLCN). However, there is no consensus within the literature upon a precise value for this conversion factor (Stevenson 1986). A majority of authors believe the range lies somewhere in the vicinity of 20 – 25 (Kahraman 2001). Assuming a PLCN within this range, maximum and minimum UCS values for each hard rock were calculated (Table 5.3). UCS values calculated from Schmidt hammer data are also shown for comparison. As with UCS calculated from Schmidt hammer data, UCS calculated from the  $I_{s50}$  are much lower than expected when compared to the literature, even when considering the highest PLCN of 25. Increasing porosity lowers the intact strength of a rock mass (Stevenson 1986; Brady & Brown 2004), thus the lower than expected intact strength of the hard rocks correlates well with their relatively high porosities (Table 5.1).

Table 5.3 – UCS values of hard rock units calculated from average  $I_{s50}$  assuming PLCN of 20 and 25. Values are presented as an average  $\pm$  standard error. Refer Appendix I for complete point load data.

	<b>Indurated andesite</b>	<b>Indurated dacite</b>	<b>Scoriaceous andesite</b>	<b>Altered andesite</b>
Average $I_{s50}$	2.7 $\pm$ 0.2	2.0 $\pm$ 0.4	1.12 $\pm$ 0.06	0.7 $\pm$ 0.2
UCS (MPa) (estimated from $I_{s50}$ )				
PLCN 20	54 $\pm$ 3	40.6 $\pm$ 0.8	23 $\pm$ 4	14 $\pm$ 1
PLCN 25	68 $\pm$ 4	51 $\pm$ 1	28 $\pm$ 5	18 $\pm$ 2
UCS (MPa) (estimated from Schmidt hammer)				
	62 $\pm$ 3	95 $\pm$ 3	15 $\pm$ 3	15 $\pm$ 3

For indurated andesite, indurated dacite and altered andesite, UCS calculated using both the Schmidt hammer and the point load test coincide with each other. However, the Schmidt hammer converted UCS for scoriaceous andesite is less than the point load converted UCS. This may simply be a reflection of the Schmidt hammer's high sensitivity to surface roughness and weathering (Selby

1993) or in the case of the scoriaceous andesite, surficial fracturing of a highly porous rock mass.

Later analysis is based on UCS values calculated from point load data (rather than Schmidt hammer data) as point load data is accepted as giving a better approximation of the true UCS (Franklin 1985).

### **5.2.3 DISCONTINUITIES**

Discontinuity data was collected from five scanline surveys; one for each of the scoriaceous andesite (site 33), altered andesite (site 40), and indurated dacite (site 52), and two for the indurated andesite (sites 12 and 26). Full details of each scanline can be found in Appendix J.

#### **5.2.3.1 DISCONTINUITY ORIENTATION**

Discontinuity orientations collected from scanline surveys for each hard rock lithotechnical unit were analysed using the stereographic projection program RockWorks2002. Using equation 3.1 (Section 3.4.3), the number of discontinuities making up each cluster was adjusted to account for the relative orientation of the discontinuity with respect to the rock face, after which the orientations of major discontinuity sets were determined for each unit. Three major discontinuity sets were determined for each hard rock lithotechnical unit. Table 5.4 presents orientations of these major discontinuity sets in order of their cluster significance; discontinuity set 1 contains the greatest number of discontinuities and thus being the most significant.

Each hard rock lithotechnical unit exhibits two discontinuity sets with steep dips of at least  $70^\circ$ , and a third discontinuity set dipping at approximately  $40^\circ$ . The exception to this is indurated andesite 1 which exhibits three steeply dipping discontinuity sets of approximately  $70^\circ$ . The steeply dipping discontinuity sets possibly represent cooling discontinuities. Aside from indurated andesite 2, the more shallow dipping discontinuity sets approximating  $40^\circ$  are too steep to represent the volcano slopes of each scanline area, described in Chapter 4 to approximate  $32 - 36^\circ$ . Further comparison of discontinuity sets in each hard rock unit is difficult. While this may suggest that discontinuity distribution varies

between individual lava flows, it is important to highlight that these discontinuity orientations are localised features, meaning complications will arise when making comparisons with the general overall slopes.

Table 5.4 – Orientation of major discontinuity sets for hard rock units. Discontinuity sets presented in order of significance, discontinuity set 1 being the most significant.  $N_{app}$  is the measured number of discontinuities from scanline surveys.  $N$  is the adjusted number of discontinuities. Indurated andesite 1 and 2 represent sites 12 and 26 respectively. Refer Appendix K for stereonet plots identifying joint sets, and associated calculations of  $N$ .

	<b>Indurated andesite 1</b>	<b>Indurated andesite 2</b>	<b>Indurated dacite</b>	<b>Scoriaceous andesite</b>	<b>Altered andesite</b>
Discontinuity set 1 orientation	70/211	70/312	76/143	48/027	70/308
$N_{app}$	3	4	2	12	9
$N$	34	14	10	20	16
Discontinuity set 2 orientation	78/320	35/210	74/334	86/022	45/165
$N_{app}$	6	1	1	3	1
$N$	6	4	7	6	11
Discontinuity set 3 orientation	69/122	84/104	44/066	70/149	71/246
$N_{app}$	5	3	7	2	6
$N$	5	3	7	5	6

### 5.2.3.2 DISCONTINUITY SPACING AND ROCK QUALITY DESIGNATION

Discontinuity spacing was measured from scanline surveys as described in Section 3.3.1.2.2. The average discontinuity spacing for each hard rock unit was calculated, after which RQD ratings were calculated using average discontinuity spacing and equation 2.1 (Section 2.4.1.1). Table 5.5 presents average discontinuity spacing, and RQD ratings, for each hard rock lithotechnical unit.

Average discontinuity spacing of the altered andesite is the smallest of all the hard rocks (measuring  $188 \pm 37$  mm (close spacing)). The widest discontinuity spacing of all the hard rocks is exhibited by scoriaceous andesite, with spacing of  $676 \pm 156$ mm (wide spacing). Indurated dacite and both indurated andesite 1 and 2, exhibit moderate spacing.

Table 5.5 – Discontinuity spacing and RQD ratings for hard rock units. Values are presented as an average  $\pm$  standard error. Indurated andesite 1 and 2 represent sites 12 and 26 respectively. Refer Appendix K (for complete spacing data) and Appendix L (for RQD calculations).

	<b>Indurated andesite 1</b>	<b>Indurated andesite 2</b>	<b>Indurated dacite</b>	<b>Scoriaceous andesite</b>	<b>Altered andesite</b>
Average discontinuity spacing (mm)	380 $\pm$ 44	403 $\pm$ 154	350 $\pm$ 88	676 $\pm$ 156	188 $\pm$ 37
RQD (%)	97	97	97	99	90
Rock quality	Excellent	Excellent	Excellent	Excellent	Excellent

With the exception of altered andesite, the RQD of each hard rock is  $> 96\%$  (excellent rock). The lower RQD rating of the altered andesite reflects the closely spaced discontinuities. While the altered andesite is the most fractured hard rock on Putauaki, the RQD rating of this unit is still 90 % (excellent rock).

### 5.2.3.3 DISCONTINUITY CONDITION

Discontinuity apertures of all four hard rock units regularly exceeded 5 mm. While only surface apertures were visible for observation and description, it would be expected that discontinuity aperture would decrease deeper into the rock mass where the degree of stress release is less (Wyllie & Mah 2004).

Discontinuity wall roughness commonly fitted into one of two categories: those that are slightly rough (typically the indurated units); and those that are very rough (typically scoriaceous and altered andesite). For the indurated units and the altered andesite, it was uncommon for discontinuities to persist  $> 10$  m. Discontinuity persistence within the scoriaceous andesite was the largest, regularly exceeding 10 m. Discontinuities commonly terminated at other discontinuities (as compared to terminating within solid rock), providing potential release surfaces for loose blocks.

Discontinuity surfaces of the indurated andesite and dacite were slightly weathered. In contrast, discontinuity surfaces of the altered andesite were highly weathered. The degree of weathering of discontinuity surfaces within the scoriaceous andesite was moderate.

#### **5.2.3.4 DISCONTINUITY INFILL**

Discontinuity infill for each lithotechnical unit comprised predominantly loosely packed, soft, coarse ( $> 5$  mm) constituents of the parent rock. A finer grained ( $< 5$  mm) infill was found to be present in some discontinuities in the altered and scoriaceous andesite. This infill was also loosely packed. Infill was never found to be hard.

#### **5.2.3.5 DISCONTINUITY SEEPAGE**

The majority of discontinuities were described as dry with no evidence of flow. Exceptions to this are a few locations showing iron staining on the discontinuity surface suggesting the presence of moisture, and those localities that are under vegetative shelter (discontinuities in such locations presented a damp infill). Obviously, the water condition of discontinuities is strongly influenced by recent rainfall. Fieldwork was undertaken during February – May, 2006, and rainfall episodes were not uncommon. However, within days of heavy rainfall, discontinuities were dry. At 821 m a.s.l. Putauaki towers above an otherwise relatively low lying terrain. This morphology suggests that any water flow on Putauaki would follow a head gradient and drain to the lower surrounding landscape producing a permanently low watertable. A low watertable would explain the observed discontinuity seepage conditions.

Assuming a low watertable, it seems strange that Secondary Crater contains a permanent lake. As water seepage from rock faces anywhere on Putauaki is not observed, the lake maybe perched on relatively impermeable strata suggesting it is fed by rainfall, not groundwater.

#### **5.2.4 ROCK MASS RATING AND GEOLOGICAL STRENGTH INDEX**

Sections 5.2.2 and 5.2.3 have presented data necessary to classify the hard rock masses following the RMR and GSI. Table 5.6 presents RMR values for each hard rock lithotechnical unit, and GSI ratings for the hard rock units are presented in Table 5.7. Note that only one RMR value and one GSI rating is presented for the indurated andesite. While scanline surveys were undertaken on the indurated andesite at two separate locations (sites 12 and 26) providing discontinuity spacing and RQD data for each site, RMR and GSI parameter ratings were

identical between the two sites (Refer Appendix M). The ratings assigned to indurated andesite in Tables 5.6 and 5.7 are therefore representative of indurated andesite at both sites 12 and 26.

Table 5.6 – RMR values for the hard rock units. Refer Appendix M for RMR categorisation data.

Parameter	Indurated andesite		Indurated dacite		Scoriaceous andesite		Altered andesite	
	Measure	Rating	Measure	Rating	Measure	Rating	Measure	Rating
UCS (MPa)	54 ± 3 – 68 ± 4	7	40.6 ± 0.8 – 51 ± 1	4	23 ± 4 – 28 ± 5	2	14 ± 1 – 18 ± 2	2
RQD	97	20	97	20	99	20	90	20
Discontinuity spacing (mm)	200 – 600	10	200 – 600	10	600 – 2000	15	60 – 200	8
Discontinuity								
Persistence (m)	1 – 3	4	3 – 10	2	10 – 20	1	10 – 20	1
Aperture (mm)	> 5	0	> 5	0	> 5	0	> 5	0
Roughness	Slightly rough	3	Slightly rough	3	Very rough	6	Very rough	6
Infill	Soft, 5 mm	0	Soft, 5 mm	0	Soft, 5 mm	0	Soft, 5 mm	0
Weathering	Slightly	5	Slightly	5	Medium	3	High	1
Groundwater	Dry	15	Dry	15	Damp	10	Dry	15
<b>Total</b>	Good rock	64	Good rock	59	Fair rock	57	Fair rock	53

The RMR assigned the lowest total rating of 53 (fair rock) to the altered andesite. Indurated andesite rated the highest with 64 (good rock), whilst indurated dacite and scoriaceous andesite rated intermediate at 59 (good rock) and 57 (fair rock) respectively. The altered andesite rated the lowest on the RMR as a combined result of its low UCS, closely spaced discontinuities and strongly weathered discontinuity surfaces (accounting for only 11 RMR units in total). The other three hard rock units showed the same three parameters to total at least 19 RMR units. Due to a relatively low UCS and moderately weathered discontinuity surfaces, scoriaceous andesite was expected to rate low on the RMR relative to the indurated units. Scoriaceous andesite represents the second lowest RMR rating;

however, its final rating was only two RMR units less than indurated dacite. It appears that the wide discontinuity spacing and very rough discontinuity surfaces of the scoriaceous andesite (accounting for 21 RMR units relative to a maximum of only 14 RMR units for any one other hard rock) offset the effects of weathering and a low UCS. The indurated andesite was expected to rate the highest on the RMR as it exhibits the highest UCS of all the hard rock units. The RMR; however, assigned only five RMR units more to the indurated andesite for UCS than it assigned to the altered andesite which exhibited a UCS nearly four times less. As a result of this weighting, the final RMR rating of the indurated andesite did not exceed that of the other hard rock units as much as expected.

Overall, the range of RMR ratings between the four hard rock units totals only 11 RMR units. This range is relatively small given four rock masses that exhibit a variety of characteristics. The small range in final RMR ratings could be related to the fact that all four hard rock units were assigned identical RMR ratings for RQD, aperture and infill. Combined, these three parameters account for up to 32 out of a total of 100 possible RMR units. With 32 RMR units effectively removed, the available variation in final RMR ratings is reduced by 32 %.

GSI ratings for hard rock units are presented in Table 5.7. As mentioned in Section 2.4.1.3, it is best not to be too precise when assigning a GSI rating, thus all GSI ratings show a variance of three units. Interestingly, compared with the RMR, the GSI assigned the highest final rating to scoriaceous andesite ( $GSI = 53 \pm 3$ ). GSI ratings for the indurated andesite, indurated dacite and altered andesite followed on  $49 \pm 3$ ,  $48 \pm 3$  and  $42 \pm 3$  respectively. GSI ratings of this study are lie between published values for andesites of  $GSI = 42$  (Özsan & Akin 2002) and  $GSI = 55 - 68$  (Moon *et al.* 2005). Assignment of the highest GSI rating to scoriaceous andesite is predominantly due to the low volumetric joint count of this unit relative to the other hard rocks.

An outline of the GSI classification scheme is presented in Figure 2.7. GSI structure ratings were defined using volumetric joint count (essentially RQD rating) and ranged from 65 (for the altered andesite) through to 83 (scoriaceous andesite) (Table 5.7), the equivalent of blocky through to very blocky. Surface

condition rating of the GSI is based on the discontinuity parameters roughness, weathering and infilling as stated in the RMR. The GSI therefore parallels the RMR when it assigns all four hard rock masses zero units for discontinuity infill (Table 5.7). Discontinuity roughness rated as very rough for both altered and scoriaceous andesite, while indurated andesite and dacite rated as slightly rough. Weathering ranged from slightly weathered (indurated units) through to highly weathered (altered andesite).

Table 5.7 – GSI ratings for hard rock units. Refer Appendix N for GSI categorisation data.

	<b>Indurated andesite</b>	<b>Indurated dacite</b>	<b>Scoriaceous andesite</b>	<b>Altered andesite</b>
Structure rating	79	75	83	65
Surface condition rating				
Roughness	3	3	6	6
Weathering	5	5	3	1
Infilling	0	0	0	0
GSI	49 ± 3	48 ± 3	53 ± 3	42 ± 3

### 5.2.5 HOEK-BROWN STRENGTH PARAMETERS

The slope stability program Galena<sup>TM</sup> was used in this study to assess the stability of Putauaki. Galena<sup>TM</sup> requires all material properties to be in the form of one strength criterion (Hoek-Brown or Mohr-Coulomb). Based on the input parameters unit weight, GSI, UCS,  $m_i$  and D, RocLab<sup>TM</sup> was used to calculate equivalent Mohr-Coulomb (c and  $\phi$ ) values for the hard rocks. The first two input parameters, unit weight and GSI, were previously assigned to each hard rock mass (Tables 5.1 and 5.7 respectively). A range of values have been determined for UCS; however, final UCS values for each unit require selection of a suitable PLCN somewhere in between 20 – 25 (Table 5.3). The material constant for intact rock,  $m_i$ , should ideally be determined by triaxial tests as described by Hoek & Brown (1997). However, tests of this sort were not available for this research. For this study, hard rock andesitic units will assume an  $m_i$  value somewhere between 20 – 30, while  $m_i$  for hard rock dacitic units will assume a value between 22 – 28 as suggested by Wyllie & Mah (2004). Unlike  $m_i$  which is relatively constant for each lithology, D is undefined, a value being chosen on a case by

case basis.  $D$  can vary from 0 (undisturbed *in situ* rock masses) to 1 (for very disturbed rock masses).

Selection of final values to represent the parameters PLCN,  $m_i$  and  $D$  are discussed in Section 5.2.5.1.

#### 5.2.5.1 SELECTION OF PARAMETERS PLCN, $m_i$ AND $D$

The potential range for PLCN,  $m_i$ , and  $D$ , are 20 – 25, 20 – 30 (22 – 28 in the case of indurated dacite), and 0 – 1 respectively. Prior to selecting a single value to represent each parameter, the influence each parameter has on final strength parameters ( $c$  and  $\phi$ ) must be evaluated. To evaluate these effects, RocLab<sup>TM</sup> was used.

By keeping  $m_i$  constant at 20, and  $D$  constant at 0, PLCN was increased from 20 – 25 (in increments of 1.0) and the resulting  $c$  and  $\phi$  were recorded. Next,  $m_i$  was increased one unit to 21,  $D$  kept constant at 0, and PLCN was again increased from 20 – 25. Resulting  $c$  and  $\phi$  were recorded. Next,  $m_i$  was increased yet another unit to 22,  $D$  still kept constant at 0, and PLCN again increased from 20 – 25 recording  $c$  and  $\phi$ . This approach was used to calculate  $c$  and  $\phi$  for all possible combinations of PLCN,  $m_i$  and  $D$ . Assuming ranges of 20 – 25 for PLCN, 20 – 30 for  $m_i$ , and 0 – 1 for  $D$ , this resulted in 726 (or 462 for indurated dacite as  $m_i$  only ranges from 22 – 28) possible combinations (6 x 11 x 11). This approach was carried out for all four hard rock units, producing approximately 2650 values for  $c$  and  $\phi$ . Combinations of PLCN,  $m_i$  and  $D$  calculated for this study, along with resulting  $c$  and  $\phi$ , are presented in Appendix O.

Presenting the effect that all 726 combinations of PLCN,  $m_i$  and  $D$  have on  $c$  and  $\phi$  would be confusing. Alternatively, those combinations using the endpoints of both PLCN (20 and 25) and  $D$  (0 and 1), along with the entire range of  $m_i$  are presented in Figure 5.1. This produces a simple yet representative graph of the influence PLCN,  $m_i$  and  $D$  have on the final intact strength of indurated andesite.

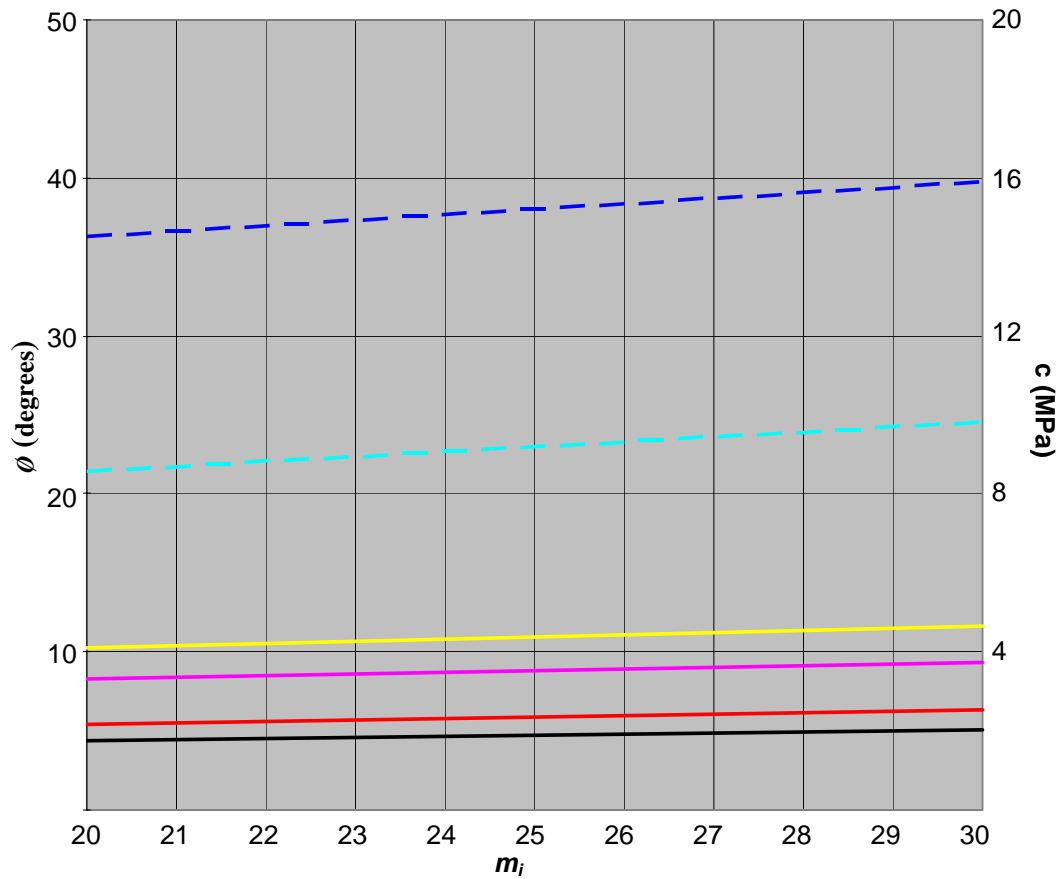


Figure 5.1 – Graph showing the effect of changing PLCN,  $m_i$  and D, on  $c$  (solid lines) and  $\phi$  (dashed lines) for indurated andesite. Lines A – H represent combinations of PLCN and D as indicated by their respective label. Refer Appendix O for the effects of changing PLCN,  $m_i$  and D, on  $c$  and  $\phi$  for all hard rocks.

Legend	
— (Blue dashed)	Line A: PLCN 20; D 0
— (Blue solid)	Line B: PLCN 25; D 0
— (Cyan dashed)	Line C: PLCN 20; D 1
— (Cyan solid)	Line D: PLCN 25; D 1
— (Yellow solid)	Line E: PLCN 25; D 0
— (Magenta solid)	Line F: PLCN 20; D 0
— (Red solid)	Line G: PLCN 25; D 1
— (Black solid)	Line H: PLCN 20; D 1

Figure 5.1 shows how an increase solely in PLCN has no effect on  $\phi$ ; these lines are insensitive to changes in compressive strength (represented by lines A and B, and lines C and D plotting directly over top of one another). Figure 5.1 shows that increasing solely  $m_i$  results in an increase in  $\phi$  of  $3.54^\circ$  for lines A and B (increasing from  $36.2 - 39.74^\circ$ ), and  $3.04^\circ$  for lines C and D (increasing from  $21.4 - 24.44^\circ$ ).

Figure 5.1 also shows that increasing both PLCN and  $m_i$  at the same time results in an increase in  $c$  of 1.36 MPa for lines E and F (increasing from 3.29 – 4.65 MPa), and 0.44 MPa for lines G and H (increasing from 1.74 – 2.18 MPa).

The degree to which  $c$  and  $\phi$  are effected by PLCN and  $m_i$ , appears to be geotechnically comparable to the variance in intact strength exhibited by jointed lavas summarised in Moon *et al.* (2005). They showed that ranges in  $c$  and  $\phi$  of approximately 2 MPa ( $c$ ) and  $8^\circ$  ( $\phi$ ) were common at any one site. These ranges are in excess of those shown by changing PLCN and  $m_i$  (Figure 5.1.) This suggests that for this study, the choice of a single value from 20 – 25 to represent PLCN, and a single value from 20 – 30 (22 – 28 in the case of indurated dacite) to represent  $m_i$ , will not influence the final  $c$  and  $\phi$  more than natural variance would. For this reason, intermediate values of  $m_i = 25$  and PLCN = 22 were chosen to represent all hard rock units.

Having selected final values to represent PLCN and  $m_i$ , this leaves only D to be determined. It can be seen from Figure 5.1 that by varying solely D, the resulting influence on  $c$  and  $\phi$  is greater than that achieved by varying both PLCN and  $m_i$  combined (for example compare lines E and G, with lines E and F). In particular, D is seen to have a large influence on  $\phi$ . For example, line A on Figure 5.1, shows indurated andesite exhibits a  $\phi$  of  $36.2^\circ$  when  $D = 0$ , and both PLCN and  $m_i = 20$ . However, by changing only D to 1 and keeping PLCN and  $m_i$  at 20,  $\phi$  recalculates to  $21.4^\circ$  (line C). This is a decrease of  $14.8^\circ$ .

The situation is similar for the other hard rocks whereby D is seen to influence  $\phi$  on the same scale. For example, under the same conditions (PLCN and  $m_i = 20$  ( $m_i = 22$  for indurated dacite)), there are decreases in  $\phi$  of approximately  $15.5^\circ$ ,  $14.9^\circ$ , and  $14.8^\circ$  for the altered andesite, indurated dacite, and scoriaceous andesite respectively. This variance of  $15^\circ$  is much greater than typical ranges of  $\phi$  suggested by Selby (1993) for undisturbed hard rock. This means that selection of a single value to represent D could result in a calculated strength which is unrepresentative of the rock mass in question. For this reason, final strengths for the hard rock masses were calculated across a range of D values from 0 – 1.

Resulting  $c$  and  $\phi$  values were used in sensitivity analysis for slope stability (Chapter 6).

Table 5.8 shows final values selected for this study to estimate Mohr-Coulomb parameters for hard rock. PLCN and  $m_i$  are represented by the values 22 and 25 respectively, while D is represented by a range of values from 0 – 1.

Table 5.8 – Input values selected for this study to estimate strength parameters for the hard rock units.

	<b>PLCN</b>	<b>UCS (MPa)</b>	<b><math>m_i</math></b>	<b>D</b>
Indurated andesite	22	$60 \pm 4$	25	0 - 1
Indurated dacite	22	$44.7 \pm 0.9$	25	0 - 1
Scoriaceous andesite	22	$25 \pm 5$	25	0 - 1
Altered andesite	22	$15 \pm 1$	25	0 - 1

## 5.3 SOFT ROCKS

### 5.3.1 UNIT WEIGHT

Unit weights of the soft rocks are presented in Table 5.9. An average unit weight of  $19.5 \pm 0.5$  kN m<sup>-3</sup> was measured for the block & ash flow corresponding to a dry density of  $1980 \pm 50$  kg m<sup>-3</sup> (Appendix G). Direct shear cores of the block and ash flow matrix were reconstructed to  $\pm 1.0\%$  of this density. For the Matahina Ignimbrite, a unit weight of  $11.79 \pm 0.08$  kN m<sup>-3</sup> was obtained corresponding to a dry density of  $1202 \pm 8$  kg m<sup>-3</sup>.

Table 5.9 – Unit weight of the soft rock masses. Refer Appendix G for complete unit weight and dry density data.

	<b>Block and ash flow</b>	<b>Matahina Ignimbrite</b>
Average unit weight (kN m <sup>-3</sup> )	$19.5 \pm 0.5$	$11.79 \pm 0.08$
Average dry density (kg m <sup>-3</sup> )	$1980 \pm 50$	$1202 \pm 8$

### 5.3.2 INTACT STRENGTH

Field measurement of soft rock intact strength was not possible. Both the block and ash flow matrix and the Matahina Ignimbrite were too soft to produce a rebound when using the Schmidt hammer, yet too hard to allow use of the soil penetrometer. Obtaining an intact strength for clasts within the block and ash flow was a possibility, but as the block and ash flow was determined to be matrix supported (Chapter 4), these values would have been of limited use in determining an intact strength for the deposit.

Intact strength of the soft rocks was measured in the laboratory using direct shear tests. As discussed in Chapter 3, direct shear tests were carried out on artificial cores constructed from loose material collected in the field (in the case of the block and ash flow), and core samples collected in the field (in the case of the Matahina Ignimbrite).

#### 5.3.2.1 BLOCK AND ASH FLOW

Prior to direct shear tests, an *in situ* overburden stress (or normal load) of 31.39 kg was calculated for the block & ash flow (Appendix P). This was based on presuming a depth of 5 m to the shear plane which is appropriate for a surficially emplaced avalanche deposit. Eight direct shear tests were carried out on reconstructed cores of the block and ash flow matrix under normal loads ranging from 14.5 to 45.5 kg (a range encompasses the calculated *in situ* overburden stress). The peak shear stress from each direct shear test was recorded and plotted on a graph of peak shear stress versus normal stress, after which a best-fit line was fitted to the points (Figure 5.2). The value of  $c$  is given by the point at which the best-fit line intercepts the  $y$ -axis, while  $\phi$  is determined from the slope of the best-fit line (Figure 5.2). An average intact strength of  $c = 0$  kPa and  $\phi = 42.1^\circ$  was measured for the block and ash flow.

Only limited work detailing the geotechnical characteristics of volcanic avalanche deposits has been published. Table 5.10 summarises geotechnical data that does exist for such deposits and compares them to values attained for the block and ash flow of this study.

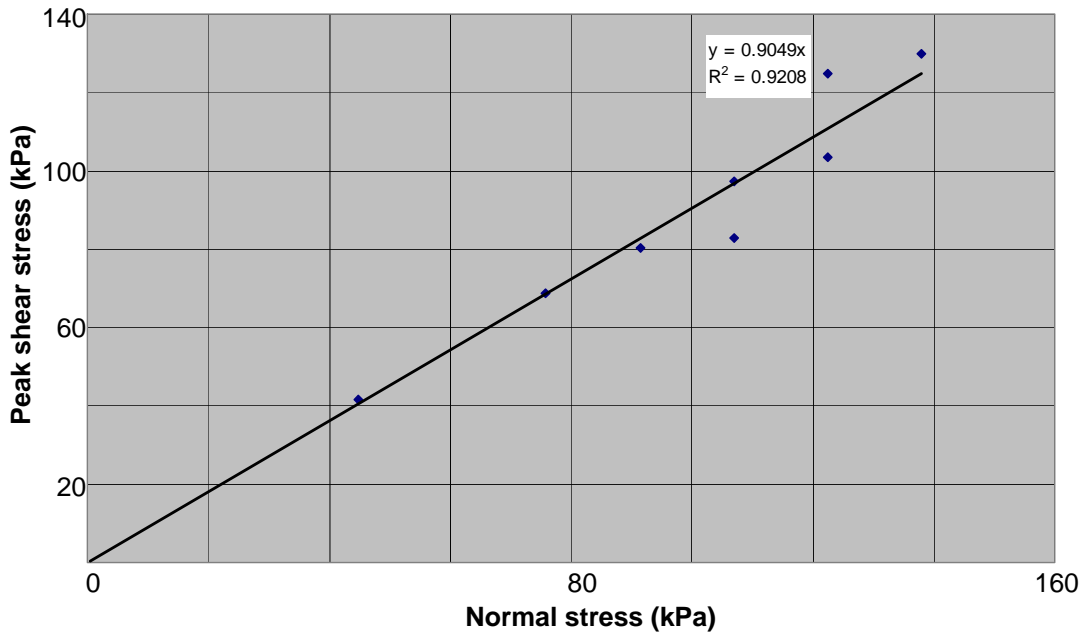


Figure 5.2 – Graph of peak shear stress versus normal stress for the block and ash flow. Refer Appendix P for complete direct shear data.

Table 5.10 – Comparison of measured geotechnical data for the block and ash flow with published geotechnical data for similar deposits.

Deposit	c (kPa)	$\phi$ (degrees)	Unit weight ( $\text{kN m}^{-3}$ )	Reference
Avalanche, Mount St. Helens	0 - 1000	38 - 44	15.11 - 19.0	Voight <i>et al.</i> (1983)
Debris flow, Compania	0	32 - 38	Undefined	Guadagno (1991)
Block and ash flow, Mount Hood	96.6	40.8	Undefined	Watters <i>et al.</i> (2000)
Brecciated rock masses, White Island	0	34.6 - 35.4	Undefined	Bradshaw (2004)
Avalanche, Mount St. Helens	10	40	17.5	Watters <i>et al.</i> (2000)
Block and ash flow, this study	0	42.1	19.5	

Table 5.10 shows, it can be seen that values of  $c$  vary widely within the literature. Thus it is no surprise to see the  $c$  of 0 kPa calculated for the block & ash flow fit within the range of published values. The low  $c$  of the block & ash flow is most

likely a reflection of the fact that it is a granular material, dominated by frictional behaviour. As a result,  $\phi$  of the block and ash flow is high, comparable with that of the upper range of published values. Unit weight is also comparable with the upper range of published values.

### 5.3.2.2 MATAHINA IGNIMBRITE

Prior to direct shear testing, a normal load of 19.04 kg was calculated for the Matahina Ignimbrite (Appendix P). This was based on the assumption of depth to the shear plane of 5 m (the approximate height of the outcrop at which sample cores were collected). Five direct shear tests were carried out on cores of the Matahina Ignimbrite under normal loads ranging from 10 to 30 kg, a range encompassing that of the calculated *in situ* overburden stress. The graph of peak shear stress versus normal stress for the Matahina Ignimbrite is presented in Figure 5.3. An average intact strength of  $c = 1.4$  kPa and  $\phi = 41.7^\circ$  was measured for the Matahina Ignimbrite (Figure 5.3).

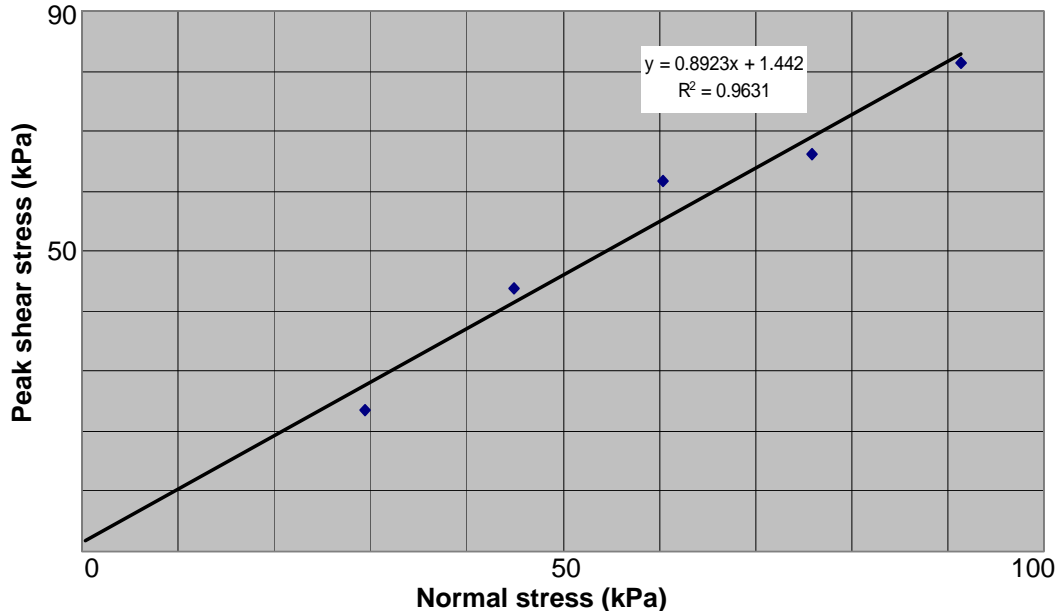


Figure 5.3 – Graph of peak shear stress versus normal stress for the Matahina Ignimbrite. Refer Appendix P for complete direct shear data.

Table 5.11 summarises published geotechnical data of various ignimbrite deposits and compares them to the values measured for the Matahina Ignimbrite. The unit

weight of the Matahina Ignimbrite coincides with the lower boundary of published values for ignimbrites, while  $\phi$  exceeds published ranges by only 1.7°. The value for  $c$  is much lower than published values. Typically, ignimbrite deposits are highly variable, some being characteristic of a hard, jointed rock mass while others such as the Matahina Ignimbrite are more similar to that of a soft, non-jointed soil (Moon 1993). While the Matahina Ignimbrite does not exhibit intact strength values similar to that of some ignimbrites, it does exhibit a low unit weight, low  $c$  and relatively high  $\phi$ ; a trend noted to be common in ignimbrites (Moon 1993). Thus although the unit weight of the Matahina Ignimbrite is not unexpected, the high variability of ignimbrite deposits as a whole may explain the low  $c$  and high  $\phi$  of the Matahina Ignimbrite.

Table 5.11 – Comparison of measured geotechnical data for the Matahina Ignimbrite with published geotechnical data for similar deposits.

Deposit	$c$ (kPa)	$\phi$ (degrees)	Unit weight (kN m <sup>-3</sup> )	Reference
Hinis Ignimbrite, Turkey	Undefined	Undefined	10.2 - 20.7	Oner <i>et al.</i> (2006)
Ignimbrite, Central North Island	140 - 13000	27 - 35	11.89 - 20.84	Moon (1993)
Shirakawa pyroclastic flow, Japan	Undefined	Undefined	16.38	Chigira (2002)
Shirasu Ignimbrite, Kagoshima	10 - 20	30 - 40	11.77 - 9.81	Chigira & Yokoyama (2005)
Matahina Ignimbrite, this study	1.4	41.7	11.79 ± 0.08	

## 5.4 SUMMARY

The aim of this chapter was to determine geotechnical properties required to aid interpretation of the stability of Putauaki. Measurement of the unit weight and intact strength of both the hard and soft rocks, as well as discontinuity description and rock mass classification (in the case of the hard rock units) was used to help produce Table 5.12 which summarises the final geotechnical properties of each lithotechnical unit.

Table 5.12 – Final geotechnical properties for the hard and soft rock units. B&A and MI represent block and ash flow and the Matahina Ignimbrite respectively. UCS<sup>1</sup> was calculated from  $r$ , while UCS<sup>2</sup> was calculated from point load tests.  $c$  and  $\phi$  are presented as possible ranges dependent on D.

Property	Indurated andesite	Indurated dacite	Scoriaceous andesite	Altered andesite	B&A	MI
RQD	97	97	99	90		
Basic RMR	64	59	57	53		
GSI	49 ± 3	48 ± 3	53 ± 3	42 ± 3		
$r$	41.2 ± 0.6	51.2 ± 0.2	18.4 ± 0.2	16.6 ± 0.4		
UCS <sup>1</sup> (MPa)	62 ± 3	95 ± 3	15 ± 3	15 ± 3		
$m_i$	25	25	25	25		
UCS <sup>2</sup> (MPa)	60 ± 4	44.7 ± 0.9	25 ± 5	15 ± 1		
Porosity (%)	11.1 ± 0.8	8.2 ± 0.2	27.3 ± 2.1	30.12 ± 0.7		
Unit weight (kN m <sup>-3</sup> )	22.8 ± 0.2	23.39 ± 0.09	15 ± 1	16.9 ± 0.1	19.5 ± 0.5	11.79 ± 0.08
$c$ (MPa)	2.08 – 3.87	1.55 – 2.89	0.86 – 1.61	0.48 – 0.95	0	1.4 × 10 <sup>-3</sup>
$\phi$ (degrees)	23.05 – 38.15	23.05 – 38.15	23.05 – 38.15	20.92 – 36.94	42.1	41.7

# *GALENA<sup>TM</sup> MODELLING*

---

### 6.1 INTRODUCTION

The following chapter explains how the slope stability program Galena<sup>TM</sup> was used to construct and analyse 10 slope profiles of the flanks of Putauaki. Definition of subsurface stratigraphy, failure surfaces and watertable elevations of each slope profile will be discussed, after which the sensitivity of slope profiles will be assessed in relation to three parameters; earthquake force, watertable elevation and D. Discussion of the sensitivity of slope profiles to these three variables, and what this means for the stability of Putauaki, will follow.

### 6.2 GALENA<sup>TM</sup>

Galena<sup>TM</sup> (version 3.10.13) was used in this study to assess the stability of Putauaki. Galena<sup>TM</sup> uses limiting equilibrium stability analyses (LEA) to assess the stability of modelled slope profiles. Potential instability of the slope is calculated via the method of slices, whereby the potential sliding mass is divided into vertical slices and the factor of safety is calculated based on force equilibrium equations (Wyllie & Mah 2004). A disadvantage of LEA is the fact that they apply simplifying assumptions to satisfy the conditions of equilibrium (Wyllie & Mah 2004). For example, in the case of Galena<sup>TM</sup>, models are two-dimensional meaning assumptions as to the width of the failed mass must be made. However, many advantages of LEA exist, including the ability to allow for varied slope support and reinforcement, and incorporation of saturated shear strength criteria (Eberhardt 2003). The ability of LEA to assess factor of safety sensitivity to changes in material properties and groundwater profiles makes Galena<sup>TM</sup> highly suitable for this study.

### 6.3 MODEL DEFINITION

For Galena<sup>TM</sup> to model the stability of a slope, model parameters must first be defined. Parameters of each model that require definition include material and water properties, slope surface, material profiles, phreatic surfaces, earthquake

force, failure surface, and analysis method. The parameters selected are discussed in this section.

### 6.3.1 MATERIAL PROPERTIES

Galena<sup>TM</sup> allows material properties, or strength parameters, to be defined in the form of Hoek-Brown (UCS, and material constants  $m$  and  $s$ ) or Mohr-Coulomb ( $c$  and  $\phi$ ) parameters. The latter were used for this study. Unit weights of materials are also required. These values were previously determined for each lithotechnical unit, and summarised (Table 5.12).

The pore pressure ratio ( $R_u$ ) is also required by Galena<sup>TM</sup>.  $R_u$  can be calculated independently from Galena<sup>TM</sup>; however, on a heterogeneous slope,  $R_u$  values will vary with material type. For this study, a default  $R_u$  value of 1.1 was used which allows Galena<sup>TM</sup> to independently calculate the  $R_u$  based on the position of the phreatic surface.

### 6.3.2 SLOPE SURFACE

Galena<sup>TM</sup> defines the slope surface as a line made up of a series of x/y co-ordinate pairs. A maximum of 48 co-ordinate pairs may be entered into Galena<sup>TM</sup> for each slope surface. Slope surfaces are defined using a right handed co-ordinate system; that is, the definition of x/y co-ordinate pairs must proceed from the left side of a model with the x co-ordinate positively increasing. For calculation reasons it is recommended that wherever possible, slope surfaces be input into Galena<sup>TM</sup> rising to the right (Galena 2003) (Figure 6.1).

Slope surfaces were obtained from ArcGIS<sup>TM</sup> as described in Section 3.2.2.

### 6.3.3 MATERIAL PROFILES

Galena<sup>TM</sup> defines material profiles in identical fashion to that of the slope surface; as a line (or series of lines) made up of a series of x/y co-ordinate pairs. These lines represent the upper limit of a material profile (Figure 6.1). Galena<sup>TM</sup> recognises that the region below the line represents that of the defined material for that line. Details on definition of the stratigraphy for each slope profile are given in Section 6.4.2

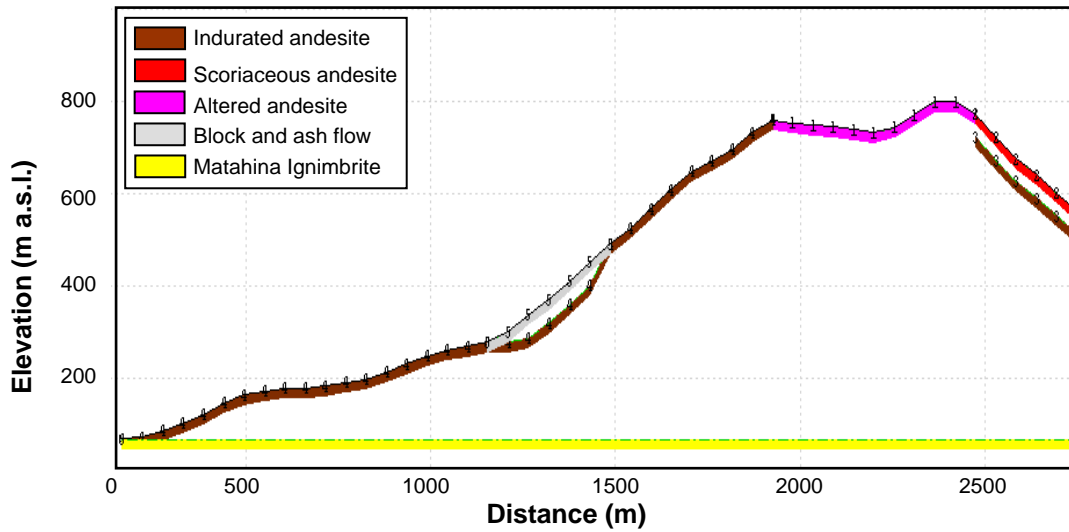


Figure 6.1 – Galena™ model of slope profile 4. The slope profile is constructed using a right handed x/y co-ordinate system allowing the slope surface to rise to the right. Material profiles are defined via lines made up of a series of x/y co-ordinate pairs; these lines represent the upper surface of the material profile. Galena™ recognises that the area below each line consists of the defined material for that line.

### 6.3.4 PHREATIC SURFACE

The phreatic surface function of Galena™ was used to simulate the watertable within the slope. Definition of the phreatic surface is through a series of x/y co-ordinate pairs, in the same manner as that of the slope surface. The absence of piezometers and seepage faces made defining the position of the watertable difficult. For this reason, the Dupuit approximation for estimating the form of an asymmetrical watertable was used. The Dupuit approximation as presented in Keady (1990) is calculated as follows:

$$hz = \left\{ H_1^2 - \left( \frac{H_1^2 - H_2^2}{L} \right) z + \left( \frac{K}{N} \right) (L - z) z 0.5 \right\} \quad (6.1)$$

where:

hz = height of watertable above any given position on x axis (m);

$H_1$  = height of left most point of ellipse (m);

$H_2$  = height of right most point of ellipse (m);

L = length of profile (m);

z = position on x-axis;

$K$  = hydraulic conductivity ( $\text{m day}^{-1}$ );

$N$  = precipitation ( $\text{m day}^{-1}$ ).

Through variation of the value representing  $N$ , the Dupuit approximation can factor in interception and runoff losses. For example, if interception was measured to be 10 %,  $N$  would be decreased by 10 %. Selection of values to represent Dupuit parameters, and interception and runoff losses, is discussed in Section 6.4.4.2

The version of the Dupuit approximation used for this study is applied to situations where the ground surface is greater on one side of the profile than it is on the other (Figure 6.2). As the elevation at the foot of each flank varies around the base of Putauaki, this version of the Dupuit approximation for estimating the form of an asymmetrical watertable ellipse was best suited for this study (as opposed to a version which estimates the form of a symmetrical watertable ellipse). The Dupuit approximation was used to calculate a range of 11 watertable elevations from 0 – 100 % (in increments of 10 %) imitating a completely dry to completely saturated slope profile. A watertable elevation of 100 % was calculated by assuming a value for  $h_z$  equal to that of the maximum height of the slope profile ( $h_{z_{\max}}$ ). A watertable elevation of 90 % was then calculated assuming a value for  $h_z$  equal to 90 % of  $h_{z_{\max}}$ , while an 80 % watertable assumed an  $h_z$  value 80 % of  $h_{z_{\max}}$ . All watertable elevations from 0 – 100% were calculated using this approach allowing the sensitivity of the model to different watertable elevations to be investigated. Discussion of watertable elevations realistic for Putauaki is in Section 6.4.4.2.

### 6.3.5 FACTOR OF SAFETY

Galena<sup>TM</sup> assesses the stability of a slope in the terms of a factor of safety,  $F$ , where:

$$F = \frac{\text{sum of resisting forces}}{\text{sum of driving forces}} \quad (6.1)$$

When the forces driving stability are exactly equal to the forces resisting stability  $F = 1.0$ ; where  $F < 1.0$  the slope is in a condition for failure; where  $F > 1.0$  the slope is likely to be stable. An accurate understanding of the parameters controlling slope stability can never be known precisely, thus  $F$  quoted to one decimal place is generally suitable (Selby 1993).

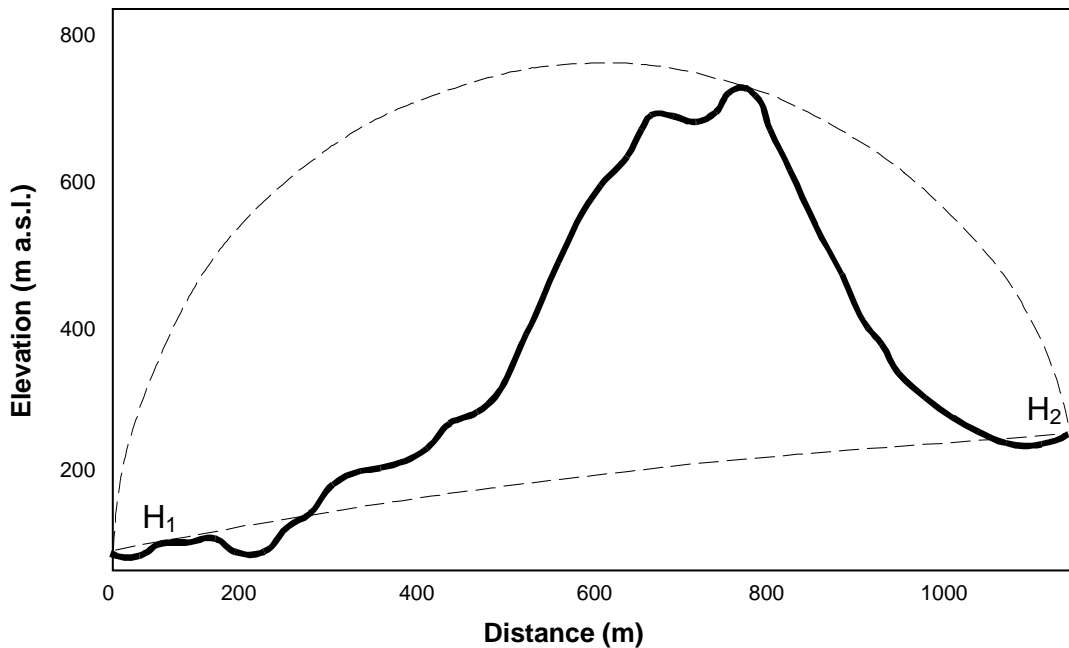


Figure 6.2 – Schematic illustrating the Dupuit approximation for estimating the form of an asymmetrical watertable. This version of the equation is applied to situations whereby the watertable elevation on either side of the profile is at different heights ( $H_1$  and  $H_2$ ). Upper and lower dashed lines represent watertable elevations of 100 % and 0 % respectively. Bold line represents profile of run-line 4 – 4a.

### 6.3.6 FAILURE SURFACE

In this study, failure surfaces were defined using the parameters ‘x-left, x-right and radius’. This describes the x co-ordinate for the left and right intercepts of the failure surface with the slope surface, together with a radius (Figure 6.3).

Perhaps the most powerful feature of Galena<sup>TM</sup> is its ability to carry out multiple analyses which quickly locate the failure surface with the minimum  $F$  ( $FS_{min}$ ). Multiple analyses operate on the basis of an initial failure surface to which the operator assigns ‘range’ and ‘trial’ restraints in the form of x-left, x-right and radius. Range restraints represent the extent of the area of interest around the

initially defined failure surface. For example, a range of 200 m assigned to a failure surface x-right value of 1200 m, would span 100 m either side of the x-right failure surface position (analysing the interval from 1100 – 1300 m). Trial positions define the coverage of the range. Continuing with the example above, defining 21 trial positions for x-right will cause Galena™ to generate 21 trial failure surfaces between 1100 and 1300 m. Each trial position will be at an interval of 10 m (21 x 10 divisions).

This process of trial failure surfaces was only described for x-right. The total number of trial failure surfaces generated during a multiple analysis will be the product of the three trial position values; x-left, x-right and radius. If trial positions of 11, 21 and 5 are entered for x-left, x-right and radius respectively, a total of 1155 trial surfaces will be generated for a single multiple analysis ( $5 \times 21 \times 5 = 1155$ ).

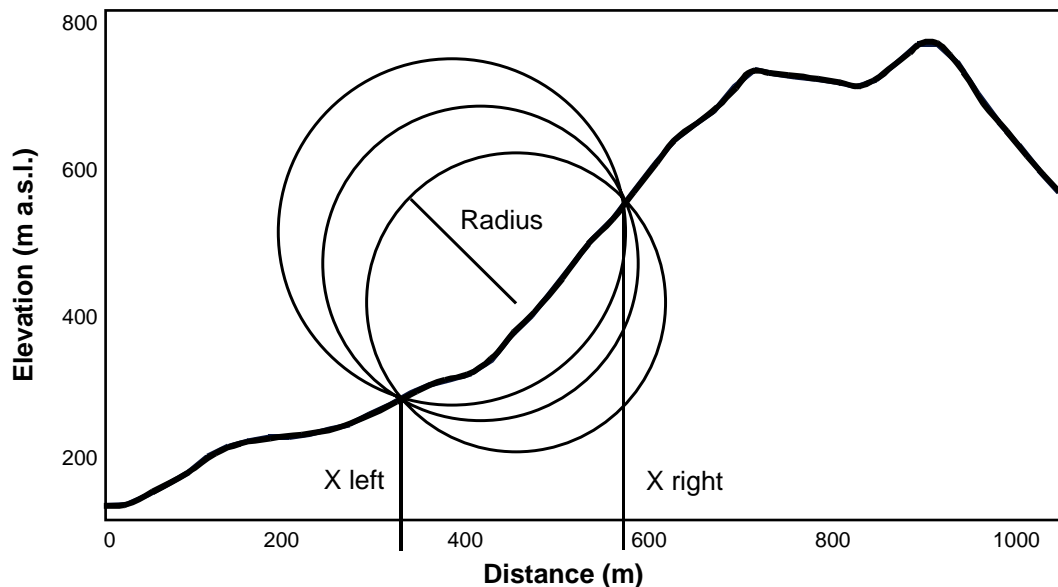


Figure 6.3 – Schematic illustrating how Galena™ models failure surfaces using x-left, x-right and radius parameters. This describes the x co-ordinate for the left and right intercepts of the failure surface with the slope surface, together with a radius. Shown are three different failure surfaces utilising the same x left and x-right co-ordinates. The radius is the differentiating factor. Bold line represents profile 4.

When Galena™ analyses a slope profile and locates  $FS_{min}$ , it is necessary to check the x-left, x-right and radius of  $FS_{min}$  to confirm that its position within the slope

profile has not been restricted by the range restraints. If for example, x-left of the initial failure surface was defined as 500 m with a restraint of 600 m (analysing an interval of 200 – 800 m) and  $FS_{min}$  returned with an x-left of 200 m, the restraints are restricting the position of  $FS_{min}$ . This means  $FS_{min}$  is inadequate. Numerous failure surfaces were analysed with varying range and trial restraints. Those  $FS_{min}$  which were not restricted by range restraints, and represented the largest scale of failure, were selected as finalised  $FS_{min}$  for the slope profile being considered ( $F_{min}$ ). Note the difference between  $FS_{min}$  (failure surface with the lowest F) and  $F_{min}$  (failure surface with the lowest F and representing the largest scale of failure). A slope profile can have numerous  $FS_{min}$  but only one  $F_{min}$ .

### 6.3.7 ANALYSIS METHOD

Two variations of the Bishop Simplified method for circular failures were incorporated into this study to analyse the slope profiles; multiple and single. Under conditions of average watertable elevation, the Bishop Simplified multiple method was used to determine an  $F_{min}$  for each slope profile as outlined in Section 6.3.6. Once  $F_{min}$  was determined, the Bishop Simplified single method was used to calculate F for each slope profile. The Bishop Simplified single method accepts failure surfaces in the same form as the Bishop Simplified multiple; x-left, x-right and radius. However, restraints cannot be applied meaning the modelled failure surface is that which is entered, in this case  $F_{min}$ .

## 6.4 MODEL CONSTRUCTION

### 6.4.1 SLOPE PROFILES

As explained in Section 3.2.2, run-lines (representing the path of each slope profile) were drawn digitally onto a DEM of Putauaki, after which an AML was used to record height points along each run-line in the form of x (horizontal distance along the run-line) and y (elevation) co-ordinates. An initial run-line trending approximately east-west was positioned, after which successive run-lines were positioned, each trending approximately 35° in a clockwise direction from the previous run-line. Five run-lines in total were drawn, dividing Putauaki into 10 similar sized segments. The position of each run-line is illustrated in Figure 6.4. The x/y co-ordinate pairs recorded for each slope profile are presented in Appendix Q. All five run-lines were positioned so as to intersect one another at

the volcano summit (Figure 6.4). Placement of fewer run-lines would restrict representative modelling of the flanks of Putauaki, while the placement of more run-lines would have required a greater degree of analysis than the time period of this study allowed. Each of the five run-lines was then divided into two slope profiles so that both profiles could be modelled rising to the right (Figure 6.5). Thus, a total of 10 slope profiles were constructed. As shown in Figure 6.5, each run-line was not divided exactly in half. This was to allow for failure surfaces to potentially involve failure of a large portion of the volcano summit. As run-lines were not divided exactly in half, slope profiles originating from the same run-line show a degree of overlap.

Each slope profile inherited the number of the run-line from which it originated. For example, slope profiles 4 and 4a were generated from run-line 4 – 4a.

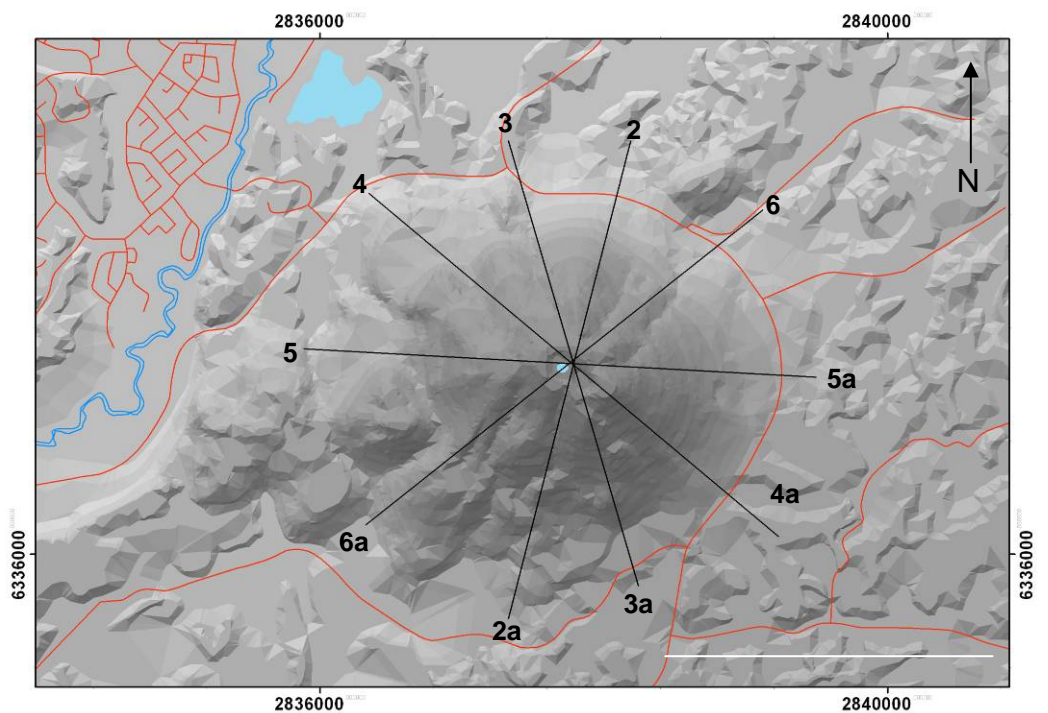
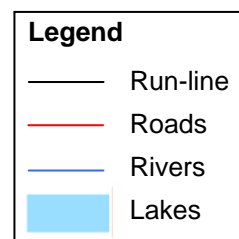


Figure 6.4 – DEM indicating location of run-lines. Numbers indicate run-line number. White line represents 2 km.



### 6.4.2 STRATIGRAPHY

At this stage, the topography of 10 slope profiles has been defined; however, definition of the material profiles (stratigraphy) of each profile is still required. In Chapter 4, approximate boundaries of each lithotechnical unit were mapped in plan view (Figure 4.15). Using GIS, each of the five run-lines were overlaid onto Figure 4.15, allowing the path of each slope profile to be viewed relative to the location of each lithotechnical unit (Figure 6.6). This provided an insight into the subsurface stratigraphy that may be expected for each slope profile. Further clues as to the stratigraphy of each profile were provided by geomorphic mapping, and an understanding of the age, nature, and succession of each lithotechnical unit, as discussed in Chapter 4.

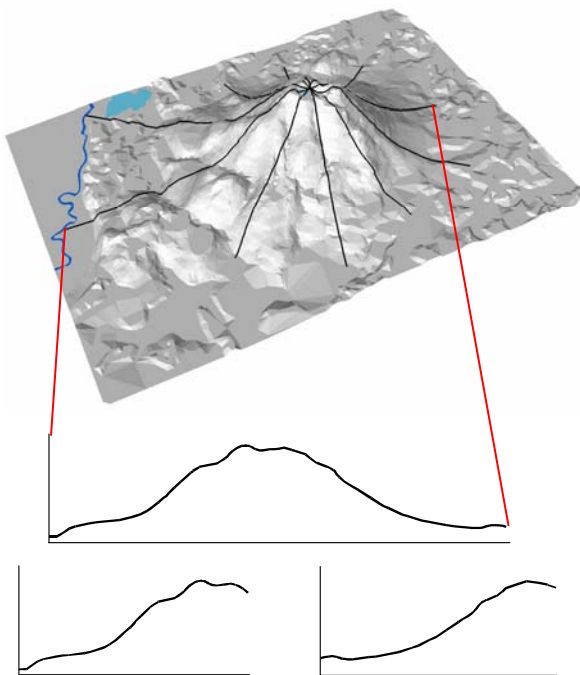


Figure 6.5 – Schematic illustrating the division of run-lines into slope profiles. Each run-line was divided in two producing a total of 10 slope profiles. This allows each slope profile to be modelled rising to the right in Galena™. Note that although only one run-line is shown as being divided in two, all five run-lines were divided. Slope profiles shown in figure pullout are those of run-line 5 – 5a.

Stratigraphy for all 10 slope profiles was initially hand sketched. In order to add the hand sketched stratigraphy into Galena™, it must be in the form of x/y co-ordinate pairs as explained in Section 6.3.3. Converting hand sketched stratigraphy into x co-ordinates involved measuring the horizontal distance along the run-line to the point where the lithotechnical unit in question intercepted the run-line. Elevation above sea level of the lithotechnical unit (y co-ordinate) was

based on inferred thickness of each respective unit. Appendix Q presents the x/y co-ordinate pairs for each lithotechnical unit present within each slope profile. It is important to remember that stratigraphic profiles must be defined in as simple a manner as possible, not only to aid Galena™ in processing, but also as any detailed stratigraphy of materials would be unsubstantiated. Figures 6.7a – c shows all 10 slope profiles and their associated stratigraphy.

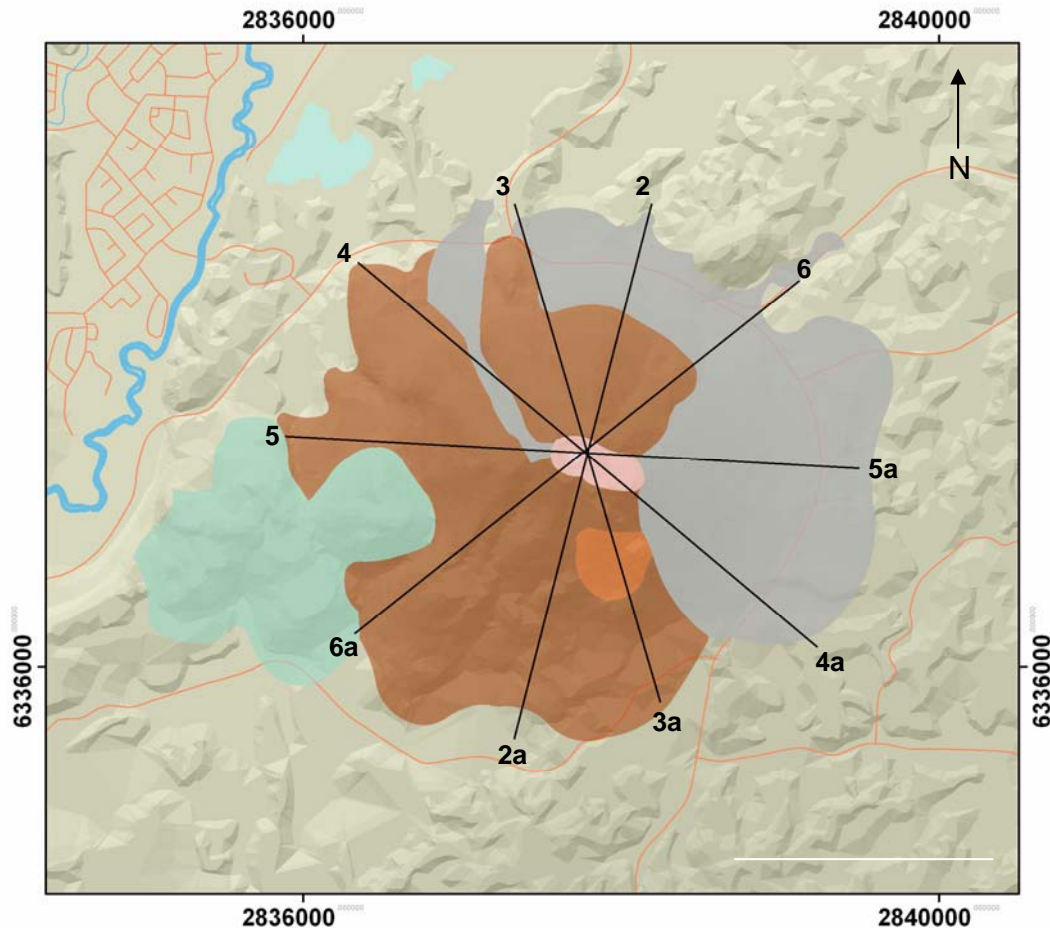
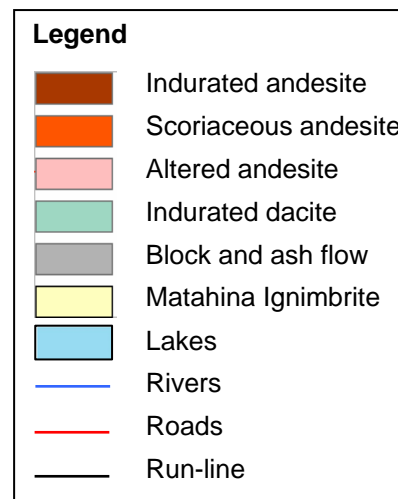


Figure 6.6 – DEM indicating location of run-lines relative to the boundaries of each lithotechnical unit. Boundaries of lithotechnical units are defined in Chapter 4. Numbers indicate run-line number. White line represents 2 km.



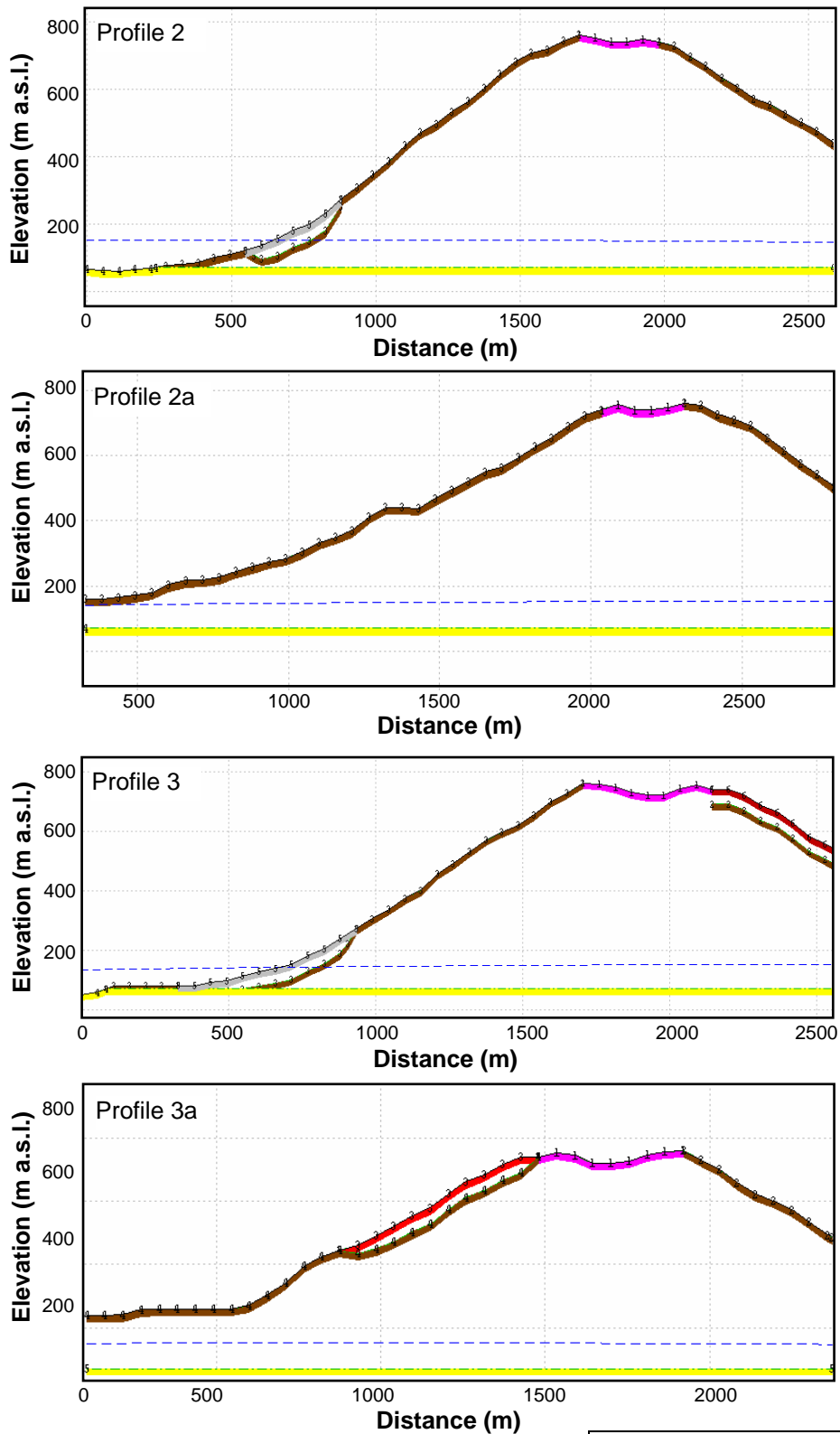
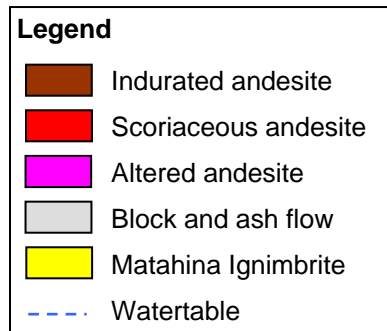


Figure 6.7a – Galena™ models of slope profiles 2, 2a, 3, and 3a showing subsurface stratigraphy. All slope profiles are shown with a watertable elevation of 20%.



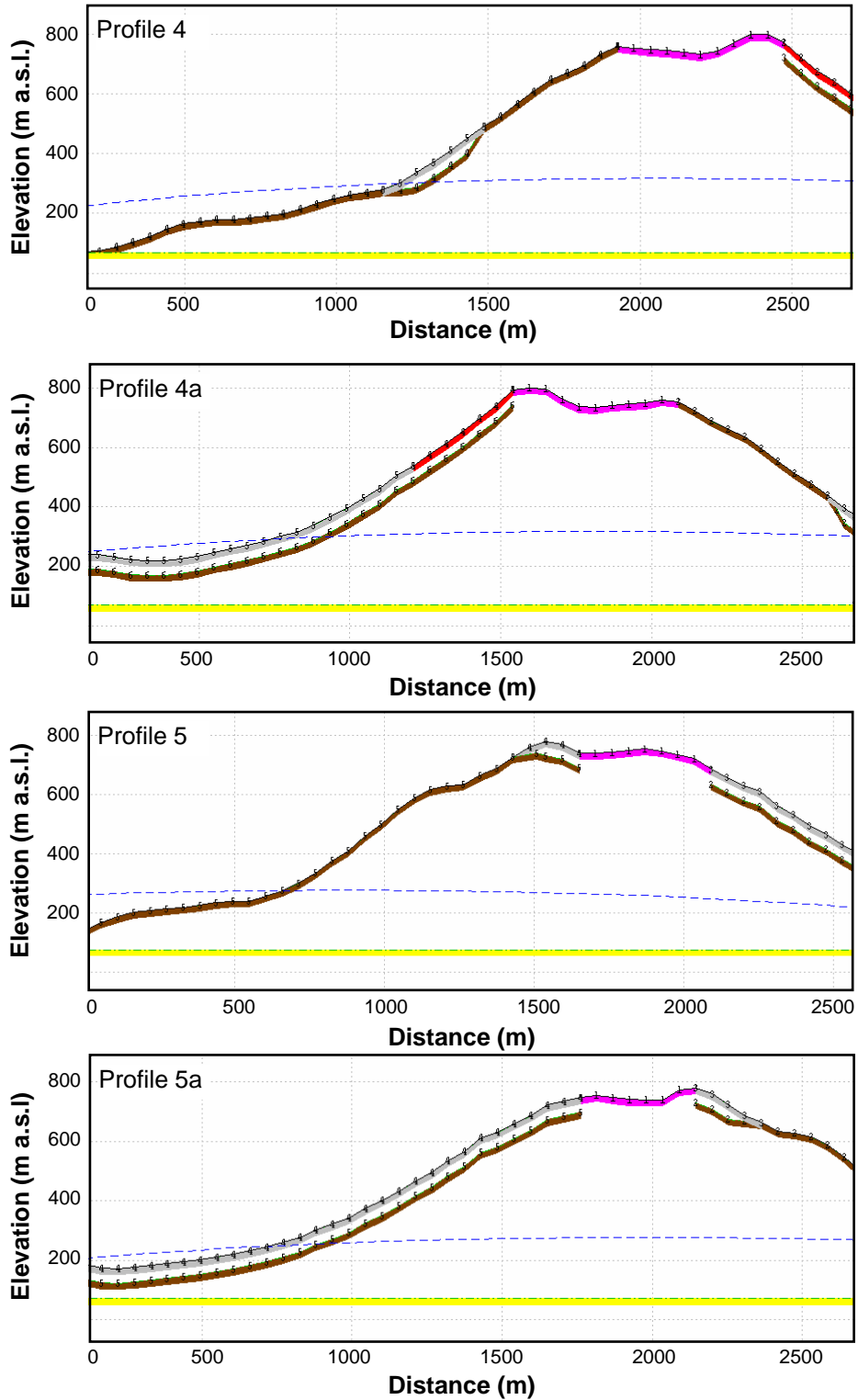


Figure 6.7b – Galena™ models of slope profiles 4, 4a, 5, and 5a showing subsurface stratigraphy. All slope profiles are shown with a watertable elevation of 20 %. Model legend is same as that for Figure 6.7a

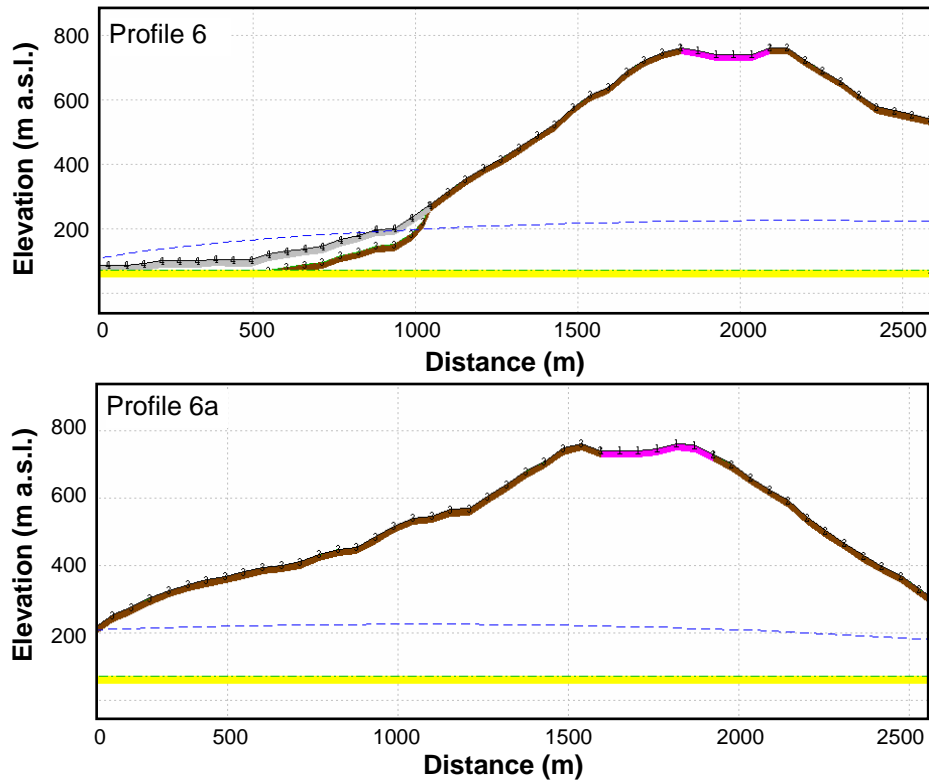


Figure 6.7c – Galena™ models of slope profiles 6 and 6a showing subsurface stratigraphy. All slope profiles are shown with a watertable elevation of 20 %. Model legend is same as that for Figure 6.7a

### 6.4.3 WATERTABLE

Once subsurface stratigraphy of all 10 slope profiles was defined, the final stage in constructing each profile is defining watertable positioning. In Section 6.3.4, the Dupuit approximation for estimating the elevation of an asymmetrical watertable was presented, along with the parameters required for its implementation,  $H_1$ ,  $H_2$ ,  $L$ ,  $N$  and  $K$ . The parameters  $N$  and  $K$  are defined in Section 6.4.4.2.  $H_1$ ,  $H_2$  and  $L$  were defined in this study as follows.

$H_1$  and  $H_2$  represent the height of the left and right most points of the watertable ellipse respectively. The absence of surface water in the down-slope direction of each slope profile made it difficult to infer the height of the watertable, and therefore difficult to infer  $H_1$  and  $H_2$ . The exception to this was profiles 4 and 5 which overlook the Tarawera River which most likely represents the true height of the watertable at that location. For these two slope profiles,  $H_2$  was interpreted as the height of the Tarawera River directly down-slope of each profile (Figure 6.8).

For the relatively flat lying landscape surrounding Putauaki, the watertable is likely to be close to the ground surface. Thus,  $H_1$  and  $H_2$  for the remaining eight slope profiles were interpreted as the ground surface at each end of the slope profile's respective run-line (Figure 6.8). The end of each run-line also marks the approximate edge of Putauaki based on the lithotechnical units identified in Chapter 4.

In the Dupuit approximation,  $L$  represents the length of the watertable ellipse. For this study  $L$  was simply calculated as the horizontal distance between  $H_1$  and  $H_2$  for each run-line

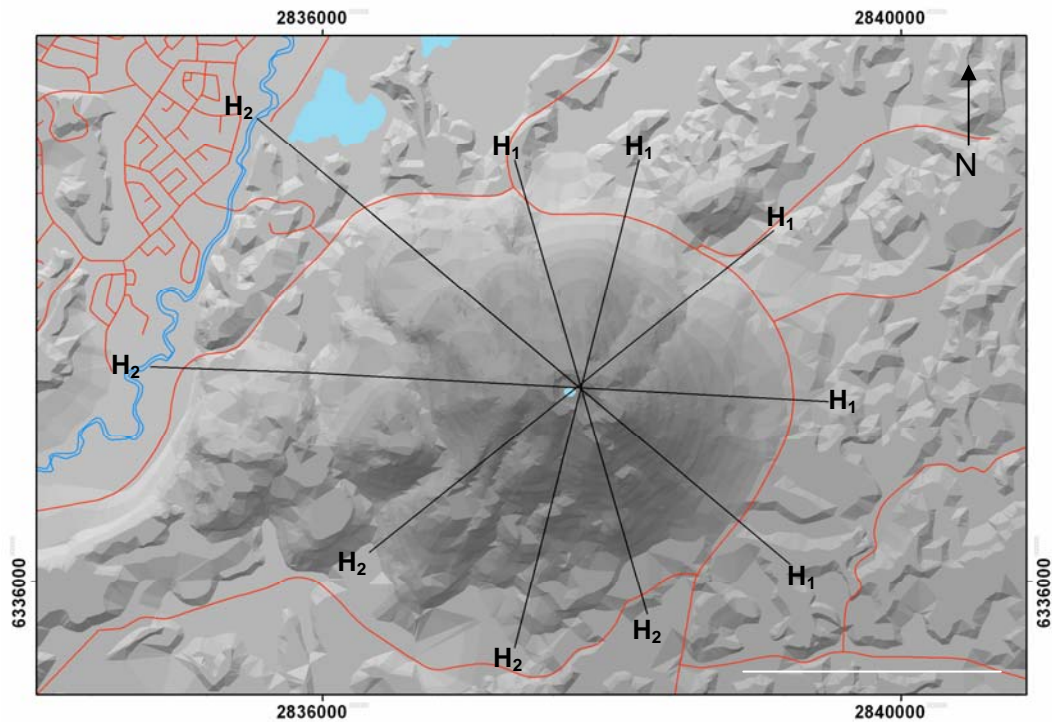


Figure 6.8 – Location of  $H_1$  and  $H_2$  parameters for each slope profile.  $H_1$  and  $H_2$  were interpreted as the heights at each end of the profile's respective run-line. Map legend is same as that for Figure 6.4. White line represents 2 km.

#### 6.4.4 SENSITIVITY ANALYSIS

Many factors are known to influence the stability of volcano slopes including volcanic activity, earthquake forces, hydrothermal alteration of rock masses, accumulation of eruptive products, and watertable elevation (Voight & Elsworth

1997; Hürlimann *et al.* 2000). The sensitivity of each slope profile was assessed in relation to earthquake forces, watertable elevation, and D.

#### 6.4.4.1 EARTHQUAKE FORCES

Galena<sup>TM</sup> simulates earthquake forces through the generation of a destabilising horizontal force “g” times the weight of the assumed failure mass. Interestingly, one of the strongest earthquake forces in New Zealand history was recorded during the Edgecumbe earthquake of 1987 (Lowry *et al.* 1989; McVerry *et al.* 1989). Seismic records and isoseismal mapping of this event indicate that Putauaki, lying 25 km south of the earthquake epicentre, was subject to earthquake forces of up to 0.33 g (Lowry *et al.* 1989). The historically high earthquake forces associated with the Edgecumbe earthquake suggest that while a future earthquake may generate forces close to 0.33 g, a seismic event whereby this intensity is exceeded seems unlikely. Voight & Elsworth (1997) identify earthquake forces of 0.1 – 0.2 g as representing sizeable volcanic earthquakes, while Hürlimann *et al.* (2000) stated that earthquake forces of 0.3 g represent moderate or even strong earthquakes.

Galena<sup>TM</sup> models of each slope profile were constructed to simulate earthquake forces ranging from 0 – 0.2 g (in 0.05 g increments), and 0.2 – 0.4 g (in 0.1 g increments). This totalled seven different earthquake forces, ranging from the equivalent of no earthquake force to strong earthquake forces.

#### 6.4.4.2 WATERTABLE ELEVATION

As described in Section 6.3.4, a range of watertable elevations representing a completely dry to fully saturated profile were modelled for each slope profile. This produced 11 possible watertable elevations for each slope profile. While it is important to see the influence of changing watertable on slope stability, it is equally important to know which watertable heights are realistic of Putauaki and which are not.

The annual precipitation for Kawerau is approximately 1.76 m (Tomlinson & Sanson 1994). Following Swanson *et al.* (1987) and Chang (2003), forest interception approximates 20 % of precipitation, while ground infiltration is stated

by Bradshaw (2004) as being approximately 20 %. Decreasing annual precipitation by 20 % accounts for interception losses ( $1.76 \text{ m} - (1.76 \text{ m} \times 0.2) = 1.41 \text{ m yr}^{-1}$ ). By calculating 20 % of  $1.41 \text{ m yr}^{-1}$ , an approximate ground infiltration value of  $0.28 \text{ m yr}^{-1}$  results. This value is substituted for N in the Dupuit approximation. An average hydraulic conductivity of fractured andesite has been estimated by Lee *et al.* (2004) to be  $53.6 \text{ m yr}^{-1}$  which represents K in the Dupuit approximation. Assuming these values, the Dupuit approximation calculates an asymmetrical watertable elevation of 10 %, 17 % and 15 % for slope profile pairs 4 – 4a, 5 – 5a and 6 – 6a respectively. The maximum height of these watertable elevations are equivalent to approximately 250 m a.s.l. (profiles 4 – 4a), 230 m a.s.l. (profiles 5 – 5a), and 190 m a.s.l. (profiles 6 – 6a). Note the estimated watertable elevation is the same for each slope profile pair as they originate from the same run-line, and thus both assume the same  $H_1$ ,  $H_2$  and L values. For example, slope profiles 4 and 4a both originate from run-line 4 – 4a. The relatively low watertable elevations calculated from the Dupuit approximation offer an explanation as to why geomorphic description of Putauaki (Chapter 4) showed little evidence of seepage faces or surface water. If seepage faces were expected on Putauaki, the maximum elevation at which they would most likely be found would be 250 m a.s.l. For most slope profiles, 250 m a.s.l. coincides with the lower flank (Figure 6.9).

Based on Dupuit approximated watertable elevations, a relatively low watertable elevation of 15% (approximately 220 m a.s.l.) is seen to be realistic for Putauaki.

#### 6.4.4.3 DISTURBANCE FACTOR

At present, the effects of D are little understood, other than to say increasing D results in decreasing rock strength (Wyllie & Mah 2004). In Section 5.2.5.1, it was concluded that a range of D values from 0 – 1.0 (in increments of 0.1) will be used to calculate the mass strength of each lithotechnical unit. This results in a range of 11 possible strengths for each unit. To account for this range of strengths, 11 Galena<sup>TM</sup> models of each slope profile were produced, each containing a different set of strength parameters for the various lithotechnical units.

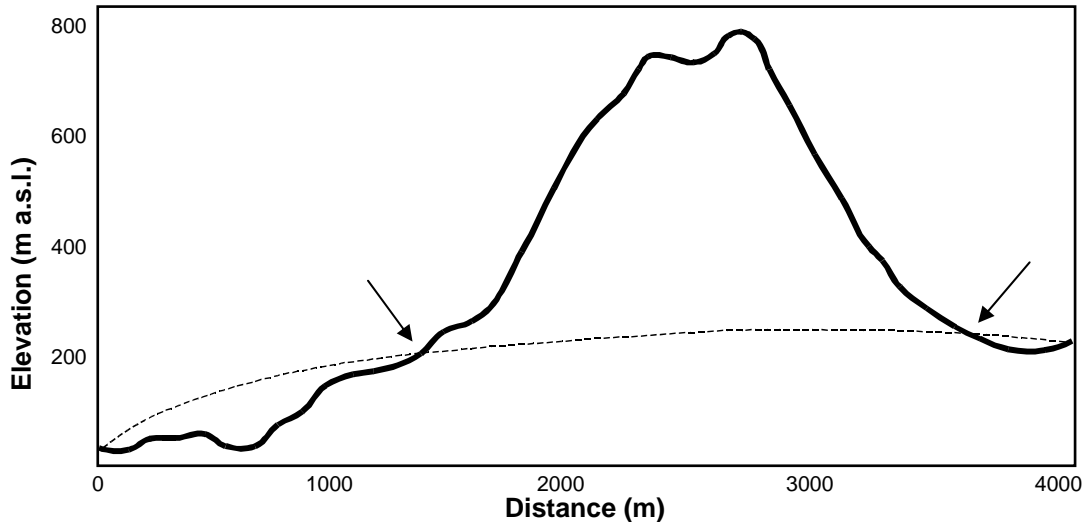


Figure 6.9 – Realistic watertable elevation for Putauaki is estimated to be 15 % (dashed line). For most slope profiles, a watertable of this elevation lays approximately 230 m a.s.l. coinciding with the lower flank. Assuming a 15 % watertable elevation, arrows indicate the maximum elevation at which seepage faces would be expected. Bold line represents profile of run-line 4 – 4a.

#### 6.4.5 A POSSIBLE 8,470 COMBINATIONS

The slope surface and stratigraphy of 10 slope profiles was defined. Using the Dupuit approximation, a range of watertable elevations from 0 – 100% slope saturation (in 10% increments) was calculated for each slope profile. Seven earthquake forces ranging from 0 – 0.4 g were applied to each slope profile for all 11 waterable elevations. Strength parameters of each lithotechnical unit were varied depending on D which ranged from 0 – 1.0 (in 0.1 increments). For each slope profile, this produced a possible 847 combinations of earthquake forces, watertable elevation and D (7 earthquake forces x 11 watertable elevations x 11 D values). This required that 847 Galena<sup>TM</sup> models be constructed for each slope profile. This resulted in the construction of a total of 8,470 Galena<sup>TM</sup> models (10 profiles x 847).

### 6.5 STABILITY OF SLOPE PROFILES

Galena<sup>TM</sup> provides a two dimensional interpretation of slope stability. The user can obtain a good measure of the length of a failure surface directly from Galena<sup>TM</sup>. However, at best, only a rough approximation of the average depth of the failure surface is possible, and the third dimension (in the case of Galena<sup>TM</sup> a failure surface width) is absent, making it difficult to calculate an area or volume

of material associated with any particular failure surface. Adding to the uncertainty is the great variability associated with the widths of failure surfaces. For example, the width of the large La Orotava landslide on Tenerife, Canary Islands, exceeds 10 km (Hürlimann *et al.* 2004), whereas the Shiidomari landslide located in Sado Island, Japan, exhibited a width of only 400 m (Ayalew *et al.* 2005). These two examples support the statements of De Silva *et al.* (1993) and Siebert (1996) when they noted that the widths of failure surfaces perpendicular to the breached direction can vary from < 1 km to > 10 km, including anywhere from < 15 – 120° of the edifice in plan view.

As this study lacks an indication as to the width of a potential failure surface, the stability of each slope profile has been categorised based on the approximate area (or segment area) of their respective  $F_{\min}$  as apparent in Galena™. Segment area is calculated using chord length and segment height as shown in Figure 6.10. In Galena™, chord length can be easily quantified with reasonable precision, measured as the straight line distance between the uppermost and lowermost points of  $F_{\min}$  (Figure 6.10). Segment height can be measured as the maximum depth of  $F_{\min}$ , determined in this study as the maximum depth with which  $F_{\min}$  is present below the slope surface at any one point.

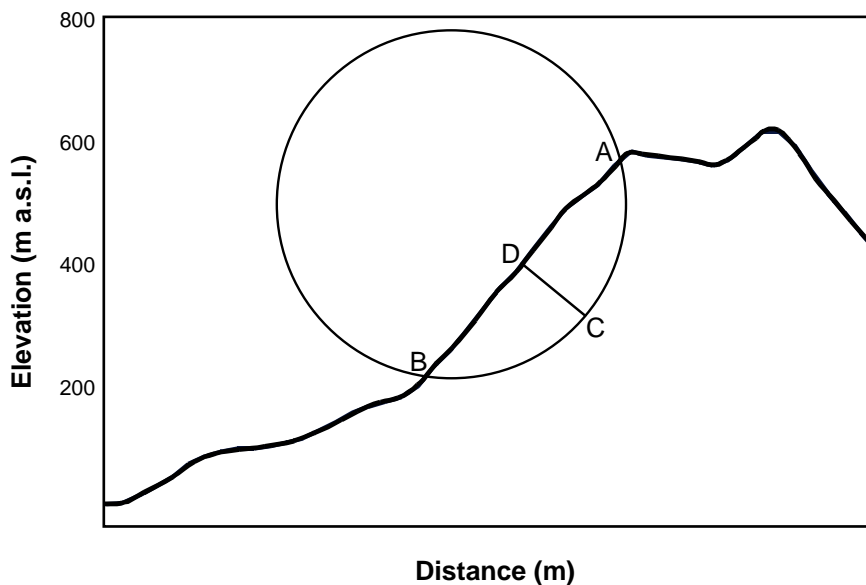


Figure 6.10 – Calculation of the segment area of  $F_{\min}$ . Arc AB represents  $F_{\min}$ . Chord length is measured as the straight line distance between the uppermost and lowermost points of  $F_{\min}$  (straight line distance from A – B). Segment height is measured as the maximum depth of  $F_{\min}$  (distance from C – D). Bold line represents profile 4.

Using the procedures explained in Sections 6.3.6 and 6.3.7,  $F_{\min}$  was defined for all 10 of the slope profiles. Appendix Q presents x/y co-ordinates for  $F_{\min}$  of each slope profile. Using chord length and segment height, the approximate area of  $F_{\min}$  for each slope profile was calculated (Table 6.1). Based on the area of a slope profile's respective  $F_{\min}$ , slope profiles are seen to exhibit two very distinct scales of failure; small scale failures ( $< 0.1 \text{ km}^2$ ), and large scale failures ( $> 0.1 \text{ km}^2$ ). Those slope profiles exhibiting small and large scale failures are illustrated in Figures 6.11 and 6.12a – c respectively.

Table 6.1– Chord length, segment height and approximate area of  $F_{\min}$  for slope profiles showing small and large scale failure.

Slope profile	$F_{\min}$		
	Chord length (m)	Segment height (m)	Area ( $\text{km}^2$ )
2	390	20	$5.21 \times 10^{-3}$
<b>Small scale failure</b>	2a	605	$1.21 \times 10^{-2}$
	3	333	$5.57 \times 10^{-3}$
	3a	155	$1.04 \times 10^{-3}$
4	1328	100	$1.02 \times 10^{-1}$
4a	1322	180	$1.61 \times 10^{-1}$
<b>Large scale failure</b>	5	1579	$1.27 \times 10^{-1}$
	5a	1289	$1.13 \times 10^{-1}$
	6	2000	$2.14 \times 10^{-1}$
	6a	1338	$1.08 \times 10^{-1}$

While the categorising of  $F_{\min}$  based on length and maximum depth does not provide a failure volume, it still clearly illustrates the varying scales of failure exhibited by each slope profile (small and large scale failures).

### 6.5.1 SMALL SCALE FAILURES

Stability analysis of profiles 2, 2a, 3, and 3a identified an  $F_{\min}$  associated with small scale failure only (Figure 6.11). Raising the watertable and increasing earthquake forces merely lowered  $F$  while maintaining a small scale failure. The run-lines representing these four slope profiles are orientated approximately north-south; a direction perpendicular to that of the migration of volcanic activity for Putauaki (as proposed by Nairn (1995)). Voight & Elsworth (1997) suggest

that flanks of the volcanic edifice perpendicular to the migration of volcanic activity are more likely to fail due to dilational effects of magmatic intrusions (Section 2.3.3). This does not seem to be the case for Putauaki, these flanks exhibiting only small scale failure.

Flank morphology may be influential in producing small scale failure for profiles 2 and 3a. Profile 2 exhibits failure which is restricted to a small bulge situated mid-slope, while  $F_{\min}$  of profile 3a is restricted to a localised increase in slope angle (Figure 6.11). Failure on profile 3 is initiated at the toe of the slope where there is a lithology change from medium strong indurated andesite, to the loosely packed, very weak block and ash flow (Figure 6.11). It is likely that the intact strength of the block and ash flow is insufficient to withstand the normal load produced by the indurated andesite lying up-slope.  $F_{\min}$  for profile 3 is restricted in depth as it forms in a shallow, surficially deposited unit, and restricted in length as it lies close to the toe of the slope. Failure of profile 2a is interesting for the fact that it displays a small bulge mid-slope, very similar to that of profile 2 (which exhibited failure restricted to the bulge). However, failure of profile 2a is restricted to up-slope of this bulge, the bulge almost acting as a toe to the failure surface (Figure 6.11).

Relative to large scale failures, the impacts associated with small scale failures are minimal. For this reason, further stability investigations were carried out on those profiles involving potential large scale failure only. The remainder of this chapter will discuss those slope profiles which exhibited potential large scale failure.

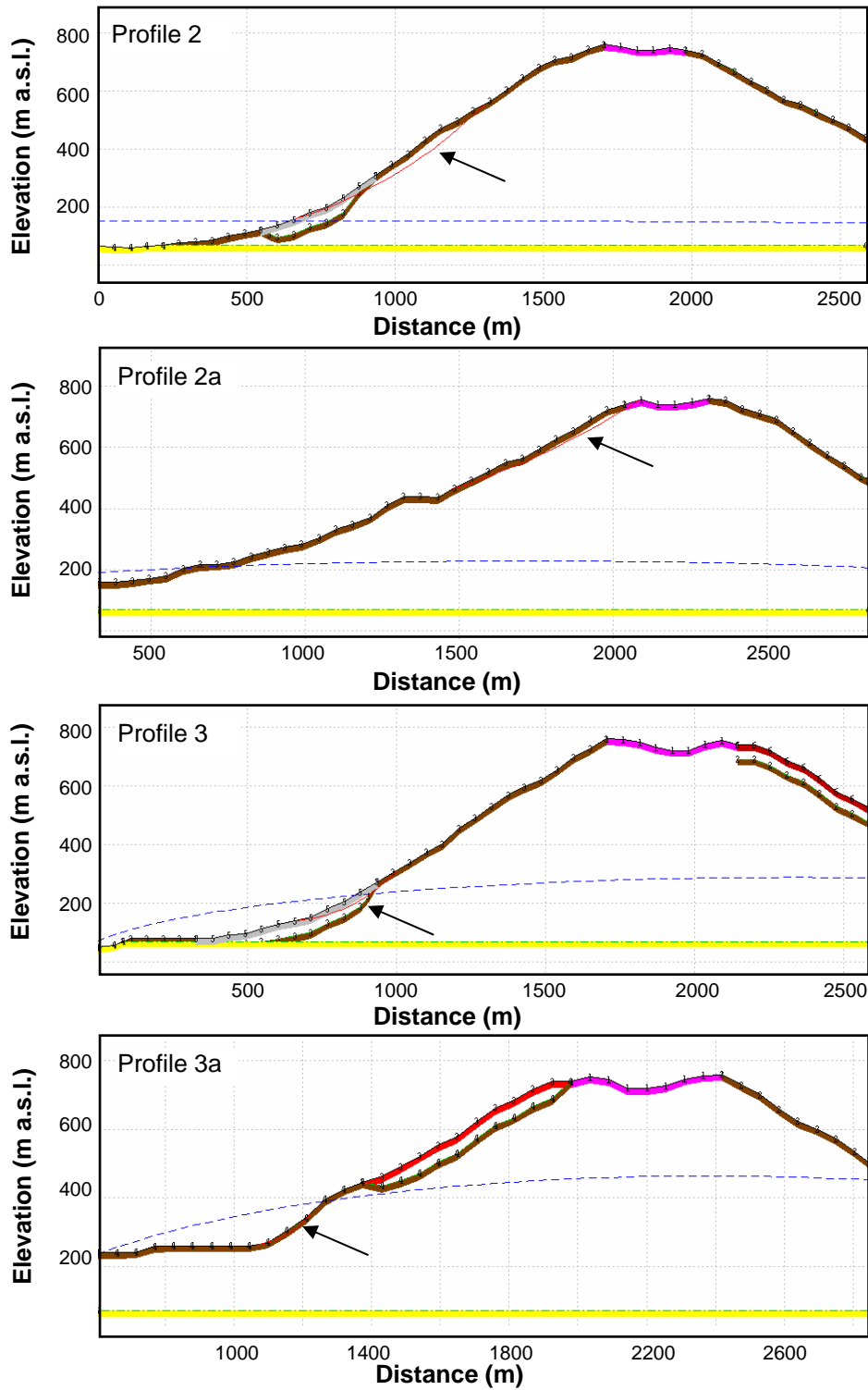
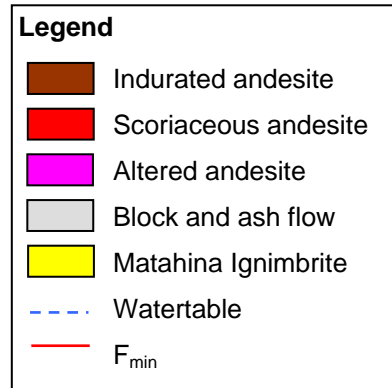


Figure 6.11 – Galena™ models of slope profiles 2, 2a, 3 and 3a showing position of  $F_{min}$ . All four of these profiles exhibited only small scale failure. All slope profiles are shown with a watertable elevation of 20 %. Arrow indicates location of failure scarp for small scale failure.



## 6.5.2 LARGE SCALE FAILURES

### 6.5.2.1 CONDITIONS OF FAILURE GRAPHS

Stability analysis of profiles 4, 4a, 5, 5a, 6, and 6a identified an  $F_{\min}$  associated with large scale failure (Figures 6.12a and b). For each of these six slope profiles, a ‘conditions of failure’ graph was constructed. For this study, the aim of a conditions of failure graph is to portray the effect that different combinations of earthquake force, watertable elevation and D have on F of a slope profile. It is a simple way to visualise which combinations promote an unstable slope, and which combinations promote a stable slope.

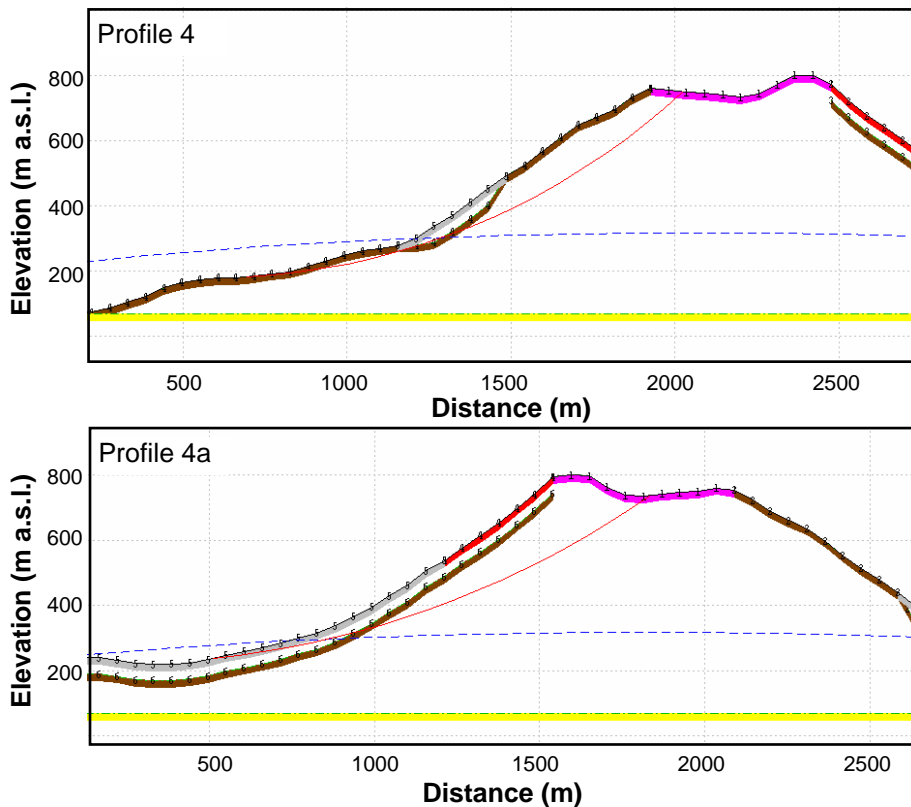


Figure 6.12a - Galena™ models of slope profiles 4 and 4a showing position of  $F_{\min}$ . Both of these profiles exhibited large scale failure. All slope profiles are shown with a watertable elevation of 20 %. Model legend is same as that for Figure 6.11.

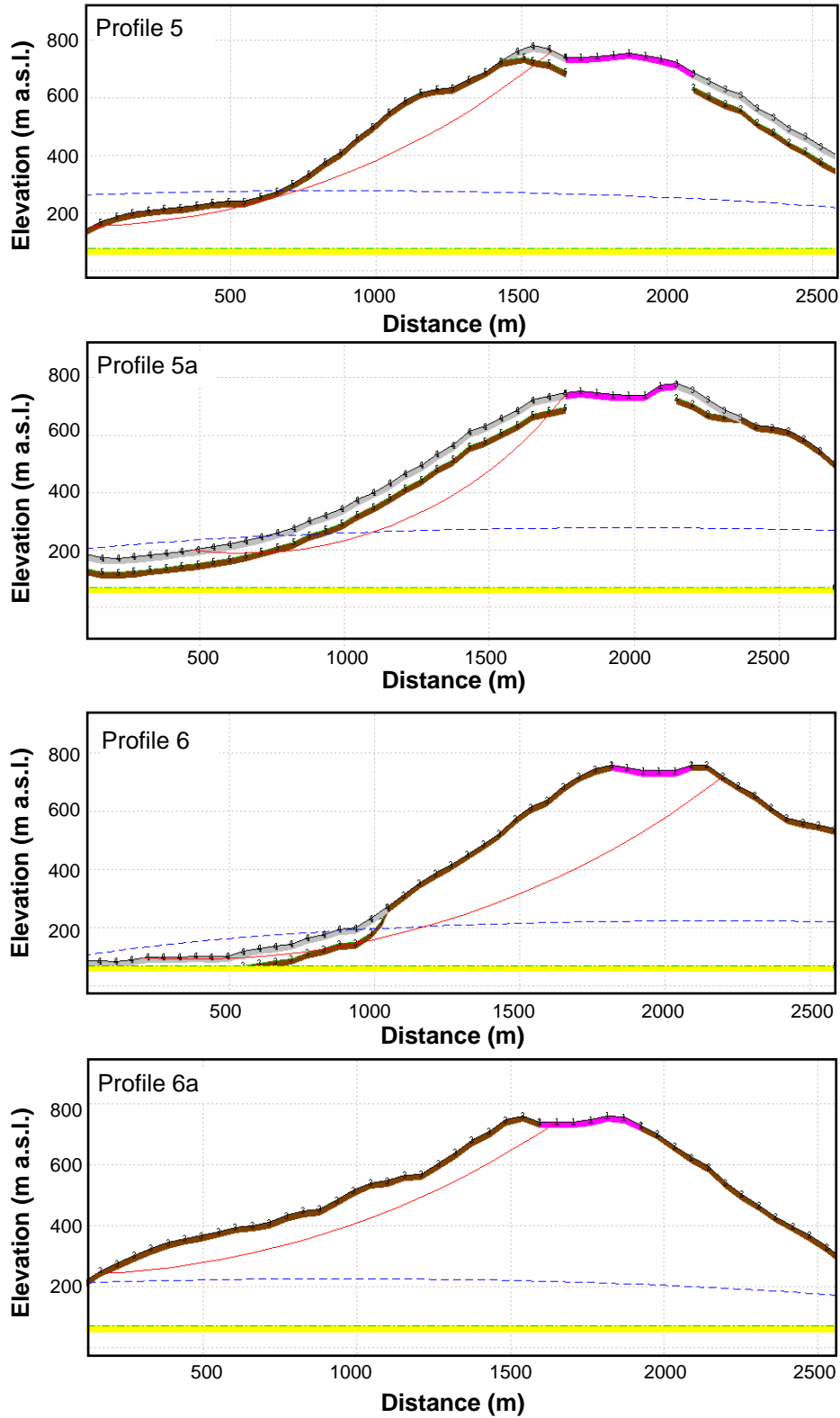


Figure 6.12b - Galena™ models of slope profiles 5, 5a, 6, and 6a showing position of  $F_{min}$ . All four of these profiles exhibited large scale failure. All slope profiles are shown with a watertable elevation of 20%. Model legend is same as that for Figure 6.11.

In Section 6.4.5, it was stated that for each slope profile, a total of 847 different combinations of earthquake force, watertable elevation and D were modelled for in Galena™. Each of these models generated an F value, full details of which are presented in Appendix R. The conditions of failure graphs are based totally on F values, thus in order to construct one of these graphs, it is first necessary to organise the F values. For each slope profile, the 847 F values calculated were divided into 11 primary groups based on watertable elevation (0 – 100 %). Each primary group contains 77 F values ( $847 \div 11$ ). F values within each primary group were then further divided into 11 secondary groups based on D (D ranging from 0 – 1). Each secondary group contains seven F values ( $77 \div 11$ ), one for each earthquake force modelled (0 g to 0.4 g).

The next step was to plot, for each earthquake force, the trend of F against an increasing watertable elevation for D values of 0 – 1 (Appendix R). Presenting trends for all 11 values of D (0 – 1 in 0.1 increments) would provide an excess of information on one graph. However, by plotting D = 0, 0.5 and 1.0, trends over the range of D values remain apparent while maintaining the clarity of the graph (Figure 6.13).

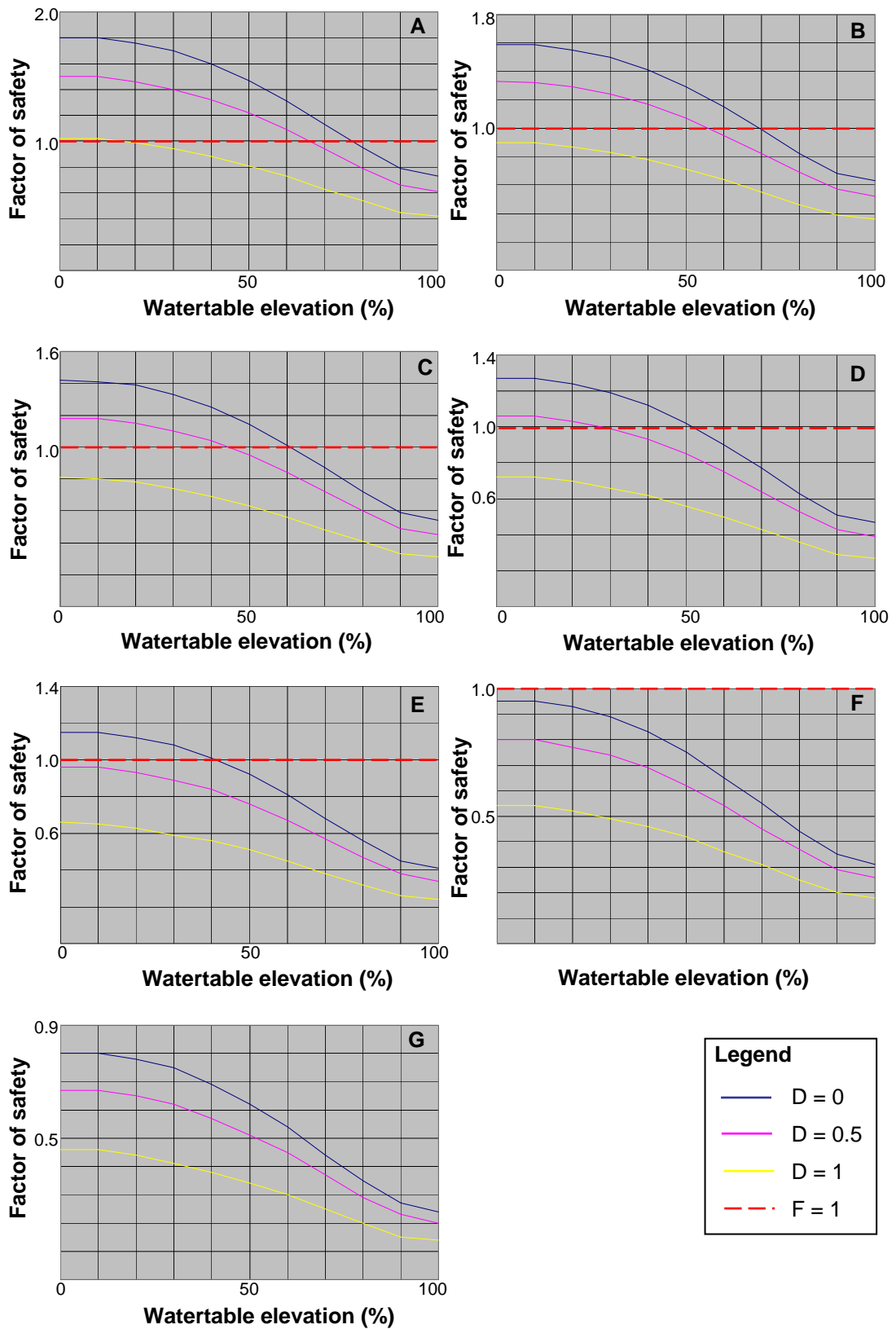


Figure 6.13 – Graphs of F (y-axis) against watertable elevation (x-axis) at earthquake forces ranging from 0 – 0.2 g in 0.05 g increments (graphs A – E), and 0.2 – 0.4. g in 0.1 g increments (graphs E – G). Watertable elevation is measured in % slope saturation. Graphs correspond to profile 4a. F = 1.0 represented by red dashed line.

A value of  $F < 1.0$  suggests a slope is in a condition for failure while an  $F > 1.0$  suggests a slope is likely to be stable. A value of  $F = 1.0$  marks the boundary between an unstable slope and a stable slope. By interpreting the graphs presented in Figure 6.13, it is possible to locate the combination of earthquake force, watertable elevation and  $D$ , which result in  $F = 1.0$ . For example, in Figure 6.13, graph A shows that for an earthquake force of 0 g and a  $D$  of 0.5, a watertable elevation of approximately 65 % will produce an  $F$  value of 1.0. Interpreting graph B, it can be seen that for an earthquake force of 0.05 g and a  $D$  of 0.5, a watertable elevation of approximately 55 % will produce an  $F$  value of 1.0. Knowing the combinations resulting in  $F = 1.0$  for each slope profile, is the prerequisite for constructing a conditions of failure graph. At this point it is important to note that the process explained thus far in Section 6.4.4, will provide the prerequisite information to construct a conditions of failure graphs for one slope profile only. This process must be carried out six separate times for each slope profile in order to produce conditions of failure graphs for all six slope profiles.

The conditions of failure graphs for profile 4, 4a, 5, 5a, 6, and 6a, are presented in Figures 6.14a and b. The conditions of failure graphs position watertable elevation on the x-axis and earthquake force on the y-axis. For  $D = 0, 0.5$  and 1, three separate lines are plotted representing the various combinations of earthquake force and watertable elevation which result in  $F = 1.0$  for the respective level of  $D$ . The area above each line represents combinations of earthquake force and watertable elevation which promote conditions for failure ( $F < 1.0$ ) for that level of  $D$ , while the area beneath each line represents the combination of earthquake force and watertable elevation which promote a stable slope ( $F > 1.0$ ). The 'realistic' line overlaid on these graphs indicates the boundary between earthquake forces and watertable elevations seen to be realistic for Putauaki (to the left of the line), and those that are seen to be unrealistic for Putauaki (to the right of the line). Placement of this line is based on the discussions of Section 6.4.4.

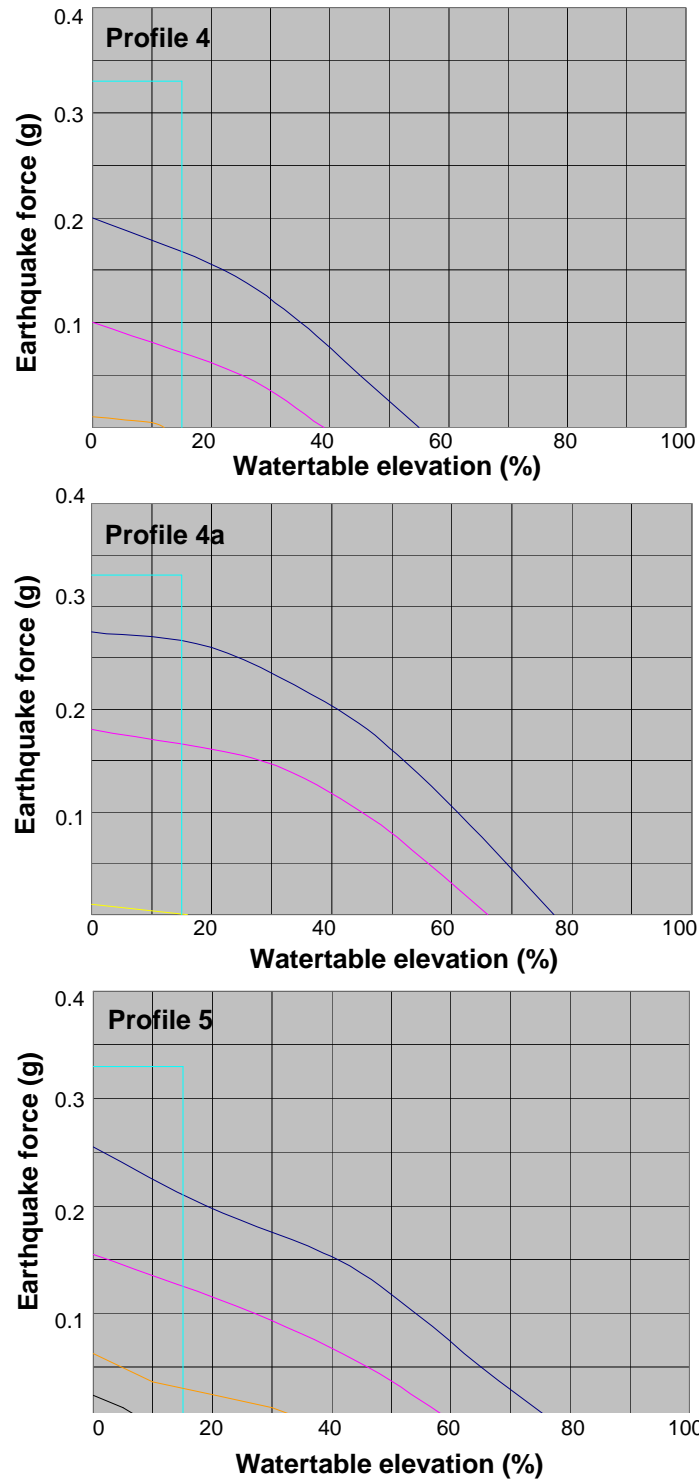


Figure 6.14a - Conditions of failure graphs for profiles 4, 4a, and 5. 'Realistic' line marks the boundary between combinations of earthquake force and watertable elevation realistic for Putauaki (to the left of the line) and combinations that are unrealistic for Putauaki (to the right of the line).



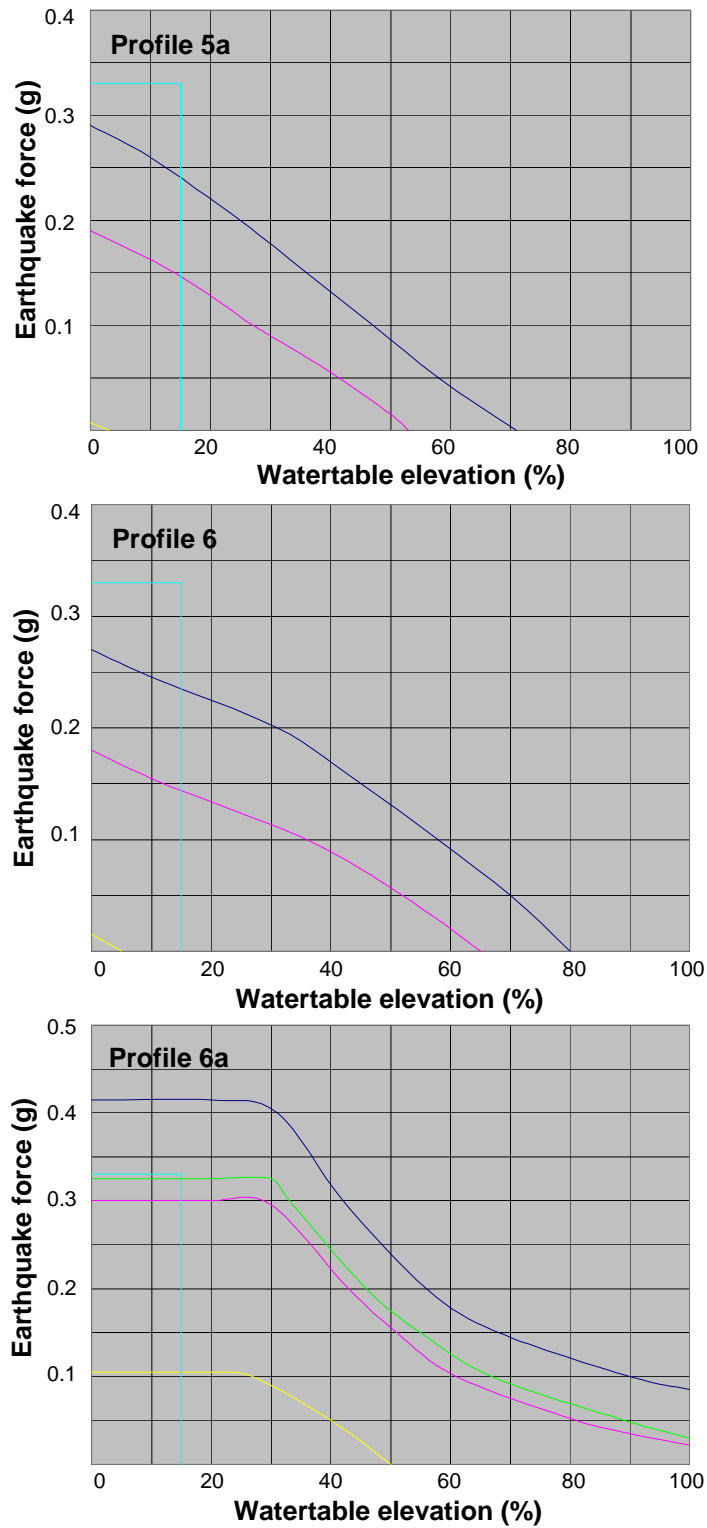


Figure 6.14b - Conditions of failure graphs for profiles 5a, 6 and 6a. 'Realistic' line marks the boundary between combinations of earthquake force and watertable elevation realistic for Putauaki (to the left of the line) and combinations that are unrealistic for Putauaki (to the right of the line). Graph legend same as that for Figure 6.14a.

The condition of failure graph for profile 4a for example (Figure 6.14a), shows that at  $D = 0$ , an earthquake force of approximately 0.275 g and watertable elevation of 0 % result in  $F = 1.0$ . Increasing earthquake force and/or watertable elevation from this point causes movement into the area of the graph above the  $D = 0$  line; the region of  $F < 1.0$  and conditions promoting an unstable slope. Alternatively, decreasing earthquake force and/or watertable elevation will cause movement into the area of the graph below the  $D = 0$  line; the region of  $F > 1.0$  and stable slope conditions (Figure 6.14a). For each line representing  $D$ , the zones above and below that line correspond to slope conditions which are unstable and stable respectively. As  $D$  increases, the critical earthquake force and watertable elevation required for unstable conditions decreases (Figure 6.14a). Continuing with the above example, it can be seen that the line representing  $D = 0$  plots partially to the left of the realistic line (Figure 6.14a). In other words, for this level of  $D$ , profile 4a is potentially unstable when exposed to combinations of earthquake force and watertable elevation seen to be realistic for Putauaki.

The conditions of failure graphs for profiles 4, 4a, 5, 5a, and 6 indicate that irrespective of  $D$ , there are realistic combinations of earthquake force and watertable elevation capable of producing an  $F < 1.0$  (Figures 6.14a and b). These slope profiles are therefore categorised as showing realistic conditions of failure. Alternatively, the conditions of failure graph for profile 6a indicates that for a  $D < 0.4$ , combinations of earthquake force and watertable elevation capable of producing an  $F < 1.0$ , must reach levels that are seen to be unrealistic for Putauaki (Figure 6.14b). This slope profile has been categorised as showing unrealistic conditions of failure. Those profiles that show realistic and unrealistic conditions of failure will be discussed in Sections 6.5.2.2 and 6.5.2.3 respectively.

#### **6.5.2.2. PROFILES SHOWING REALISTIC CONDITIONS OF FAILURE**

The conditions of failure graphs for profiles 4, 4a, 5, 5a, and 6 show that, irrespective of  $D$ , there are realistic combinations of earthquake force and watertable elevation capable of producing an  $F < 1.0$  (Figures 6.14a and b).

Based on Figures 6.14a and b and assuming a watertable elevation of 0 %, critical earthquake forces required to promote instability for varying levels of  $D$  are

shown for profiles 4, 4a, 5, 5a, and 6 (Table 6.2.) In the situation whereby watertable elevation exceeds 0 % (which is very likely as realistic watertable elevation is assumed to be 15 %), critical earthquake forces for each slope profile would be even lower. Of the five slope profiles, profile 4 appears the most unstable requiring an earthquake force of only 0.2 g to produce unstable conditions (Table 6.2; Figure 6.15a). The slope profile able to withstand the greatest earthquake force is that of profile 5a which shows a critical earthquake force of 0.29 g (for a watertable elevation = 0 % and  $D = 0$ ) (Table 6.2; Figure 6.14b). The higher critical earthquake force profile 5a is likely influenced by the fact that the  $F_{\min}$  is situated within both indurated andesite and the block and ash flow (Figures 6.12b). Indurated andesite exhibits one of the highest intact strengths of the six lithotechnical units identified on Putauaki, while the friction angle of the block & ash flow measures  $42.1^\circ$ , much  $> 32 - 36^\circ$ ; angles typical of the flanks of Putauaki (Chapter 5). If the high critical earthquake force of profile 5a is in fact a result of these two lithotechnical units, it then appears strange that profile 4, which exhibits an  $F_{\min}$  situated predominantly within indurated andesite (Figure 6.12a) shows the lowest critical earthquake force of 0.2 g. It is difficult to assume relationships solely between the stability of a slope profile and the intact strength of lithotechnical units. It is more a case of the combination of many factors, such as intact strength, rock mass characteristics, earthquake force, watertable elevation, unit weight and slope angle.

Table 6.2 - Critical earthquake force required to produce an  $F = 1.0$  for profiles 4, 4a, 5, 5a, and 6 at varying levels of  $D$  (assuming a watertable elevation = 0 %). N/A indicates that a slope profile cannot achieve stability for the respective combination of watertable elevation and  $D$ . Note that critical earthquake forces for all slope profiles are less than earthquake forces assumed to be realistic. In the situation whereby watertable elevation exceeds 0 %, the critical earthquake forces of each slope profile would be even lower.

Slope profile	Critical earthquake force (g)			Realistic earthquake force (g)	Realistic watertable elevation (%)
	D = 0	D = 0.5	D = 1.0		
4	0.2	0.1	N/A		
4a	0.275	0.18	0.01		
5	0.255	0.155	N/A	0.33	15
5a	0.29	0.19	0.007		
6	0.27	0.18	0.015		

The conditions of failure graph for profile 4a is interesting for the reason that the lines representing  $F = 1.0$  at different levels of  $D$  do not show a steady decline like the other four slope profiles (Figures 6.14a and b). Instead, they plot close to horizontal at low watertable elevations only beginning to decline at a watertable elevation of approximately 12 %. This is most likely a reflection of the position of  $F_{\min}$  within the slope profile. At a watertable elevation of  $< 12\%$ , the vertical height of the watertable is insufficient to impinge upon  $F_{\min}$  (Figure 6.15). As watertable elevation has  $< 12\%$  has little effect on the stability of profile 4a, and a watertable elevation  $> 15\%$  is deemed to be unrealistic, the stability of profile 4a is largely unaffected by changes in watertable elevation.

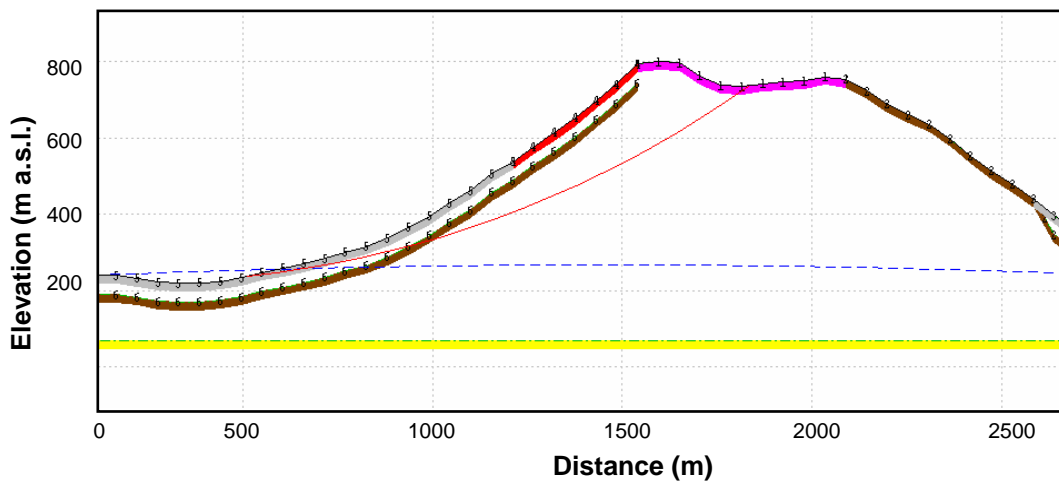
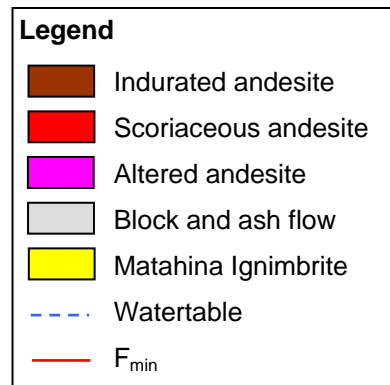


Figure 6.15 – Galena™ model of profile 4a indicating a 12 % watertable elevation. Note how watertable elevation must be  $> 12\%$  to impinge upon  $F_{\min}$ .



The conditions of failure graph for profile 4 shows that the line representing  $F = 1.0$  at a  $D$  of 1.0 does not plot on the graph (Figure 6.14a). A value of  $D = 0.8$  is the highest level of disturbance that manages to plot on this graph, meaning that as long as  $D$  is  $> 0.8$ , profile 4 cannot achieve stable conditions irrespective of

earthquake force and watertable elevation. Slope profile 5 shows similar characteristics being unable to achieve stable conditions at levels of  $D$  much  $> 0.9$  (Figure 6.14b). In Table 5.12, it was shown that when assuming a value of  $D = 1$ , the friction angle of all hard rocks was approximately  $22^\circ$ , much less than the average slope angle of Putauaki which approximates  $32 - 36^\circ$ . This perhaps explains why profiles 4 and 5 cannot achieve stability when  $D = 0$ . The fact that the other slope profiles (4a, 5a and 6) can achieve a level of stability when  $D = 1$  (Figures 6.14a and b), even though at this level of  $D$  the hard rock friction angle is much less than that of the slopes of Putauaki, may be partially due to the level of cohesion exhibited by each hard rock. Alternatively, this could be further evidence that it is the combination of many factors that influences the stability of slopes.

### 6.5.2.3 PROFILES SHOWING UNREALISTIC CONDITIONS OF FAILURE

As with the five slope profiles showing realistic conditions of failure, the conditions of failure graph for profile 6a shows that realistic earthquake forces and watertable elevations are required to promote instability for values of  $D > 0.4$  (Figure 6.14b). However, for values of  $D < 0.4$ , unrealistic combinations of earthquake force and watertable elevation must be achieved to promote slope failure (Table 6.3; Figure 6.14b). This sets profile 6a apart from the other five slope profiles which were, irrespective of  $D$ , all seen to be unstable when exposed to realistic earthquake forces and watertable elevations.

Table 6.3 – Critical earthquake force required to produce an  $F = 1.0$  for profile 6a at varying levels of  $D$  (assuming a watertable elevation = 0 %). Note that the critical earthquake force for profiles 6a at  $D = 0$  is greater than earthquake forces assumed to be realistic. In the situation whereby watertable elevation exceeds 0 %, the critical earthquake forces of each slope profile would be even lower.

Slope profile	Critical earthquake force (g)			Realistic earthquake force (g)	Realistic watertable elevation (%)
	D = 0	D = 0.5	D = 1.0		
6a	0.415	0.3	0.105	0.33	15

In Section 6.5.2.2, it was discussed how profile 4a appeared to be little affected by watertable elevations  $< 12\%$ . Profile 6a is similar in the sense that its conditions

of failure graph shows a relatively consistent  $F$  for watertable elevations  $< 25\%$  (Figure 6.14b). Once watertable elevation exceeds  $25\%$ , the lines representing  $F$  at different levels of  $D$  decrease with increasing watertable elevation. The explanation for this trend is thought to be similar to that proposed for profile 4a; that the watertable does not impinge upon  $F_{\min}$  until an elevation of  $25\%$  is achieved (Figure 6.16).

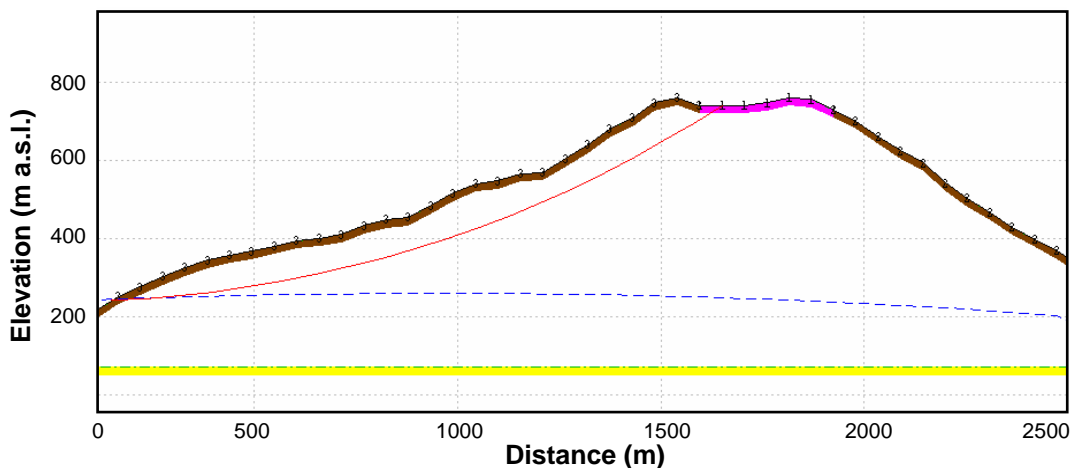


Figure 6.16 - Galena™ model of profile 6a indicating a  $25\%$  watertable elevation. Watertable elevation must be  $> 25\%$  to impinge upon  $F_{\min}$ . Graph legend same as that for Figure 6.15.

Figure 6.12b shows that aside from a central conduit of altered andesite which is inferred to be present in all slope profiles, profile 6a consists entirely of indurated andesite. The high intact rock strength of indurated andesite could explain the high level of stability exhibited by profile 6a.

Interestingly, the lines representing  $F = 1.0$  on the conditions for failure graph for profile 6a, all show a concave nature (Figure 6.14b). This appears strange as the conditions of failure graphs for the other five slope profiles all show a convex (or linear in the case of 5a) nature (Figure 6.14a and b). One explanation could be due to the orientation of  $F_{\min}$  relative to watertable surface. For profile 6a, the depth below the slope surface of  $F_{\min}$  is greater in the lower parts of the slope than it is in the upper slope (Figure 6.12b). Compare this to the other five slope profiles which all show  $F_{\min}$  to lie at a greater depth in the upper parts of the slope profile (Figure 6.12a and b). In the case of profiles 4, 4a, 5, 5a, and 6, a  $10\%$

increase in watertable elevation in the upper parts of the slope profile will saturate a larger portion of  $F_{\min}$  than would a 10 % increase in watertable elevation in the lower parts of the slope profile. Profile 6a in contrast, would see saturation of a larger portion of  $F_{\min}$  for every 10 % increase in watertable elevation through the lower parts of the slope profile, than would be seen with a 10 % increase in watertable elevation in the upper parts of the slope. This trend is illustrated in Figure 6.17 and could explain the concave and convex form exhibited in conditions of failure graphs. The conditions of failure graphs for profiles 4, 4a, 5, 5a, and 6 show a convex form (Figure 6.14a and b); the line representing  $F = 1.0$  decreasing much more rapidly at higher watertable elevations (where, relative to the lower part of the slope, a larger portion of  $F_{\min}$  is saturated for every 10 % rise in watertable elevation) (Figure 6.17). The conditions of failure graph for profile 6a is the opposite showing a concave form (Figure 6.14b); the line representing  $F = 1.0$  decreasing much more rapidly as watertable elevation saturates the lower parts of the slope (where relative to the upper part of the slope, a larger portion of  $F_{\min}$  is saturated for every 10 % rise in watertable elevation (Figure 6.17). The conditions of failure graph for profile 5a was noted as having a roughly linear form which is most likely due to the relatively consistent depth below the slope surface of the  $F_{\min}$  (Figures 6.12b and 6.14b).

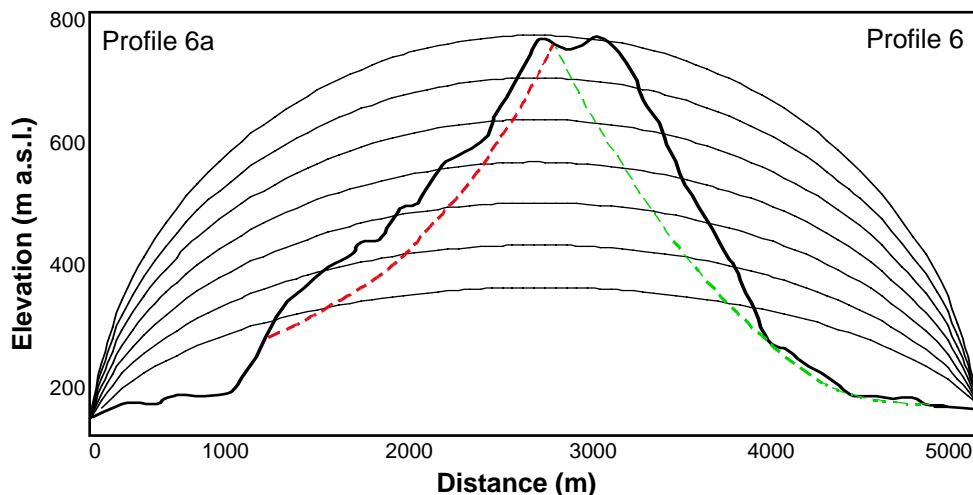


Figure 6.17 – Profile of run-line 6 – 6a with watertable heights ranging from 30 % (lowermost ellipse) to 90 % (uppermost ellipse) in 10% intervals.  $F_{\min}$  of profile 6 and 6a indicated by the green and red dashed line respectively.

## 6.6 SUMMARY AND CONCLUSIONS

Ten slope profiles of the flanks of Putauaki were constructed in Galena<sup>TM</sup>. The sensitivity of each slope profile was assessed in relation to earthquake forces, watertable elevation and  $D$ .  $F_{\min}$ , representing the failure surface with the lowest factor of safety and largest scale of failure, were defined for each slope profile. Based on  $F_{\min}$ , slope profiles were seen to exhibit two distinct categories of failure; small scale failures (involving  $< 0.1 \text{ km}^2$  of material as exhibited by profiles 2, 2a, 3, and 3a), and large scale failures (involving  $> 0.1 \text{ km}^2$  of material as exhibited by profiles 4, 4a, 5, 5a, 6, and 6a).

Conditions of failure graphs were constructed for each slope profile which was found to exhibit potential large scale failure. These graphs portrayed the influence that various combinations of earthquake force, watertable elevation and  $D$  may have on slope stability. They also highlighted which combinations of these three parameters are realistic and unrealistic for Putauaki. Based on the conditions of failure graphs, it was concluded that profiles 4, 4a, 5, 5a, and 6 showed potential for failure under realistic conditions (earthquake forces  $< 0.33 \text{ g}$  and/or watertable elevations  $< 15 \%$ ), while profile 6a showed potential for failure under unrealistic conditions (earthquake forces  $> 0.33 \text{ g}$  and/or watertable elevations  $> 15 \%$ ). The combinations of earthquake force, watertable elevation and  $D$  necessary to promote instability of each slope profile are summarised in Table 6.4.

In Section 6.4.4.1, it was discussed how the Edgecumbe earthquake of 1987 produced earthquake forces of up to  $0.33 \text{ g}$  as measured 25 km north of Putauaki. Based on the conditions of failure graphs constructed in this chapter, an earthquake force of this intensity would promote instability for profiles 4, 4a, 5, 5a, and 6. The fact that there was no report of slope failure on the scale of that modelled in this study suggests one of two possibilities.

Firstly, the Galena<sup>TM</sup> models constructed may overestimate the influence of those factors which promote slope instability. If this is the case, slope profiles would be able to maintain stable slopes even when exposed to earthquake forces and watertable elevations which the conditions of failure graphs suggest should promote instability. Reasons as to why the models may underestimate slope

stability are likely associated with the material properties of the hard rock lithotechnical units. Strength parameters of the hard rock units were calculated based on surface rock mass strength measurements. Due to surface relaxation and weathering of a rock unit, measurement of surface mass strength will underestimate mass strength of the rock unit as a whole. Underestimating rock mass strength will influence final stability analysis of slope profiles. It is also likely that the assumptions involved in construction of Galena<sup>TM</sup> models will influence final stability. For instance, the actual form of the watertable surface (estimated in this study using the Dupuit approximation for an asymmetrical ellipse) may not match that of an asymmetrical ellipse. Alternatively, unit weights of each lithotechnical unit may not be representative of the rock mass as a whole. As Galena<sup>TM</sup> simulates earthquake forces through the generation of a destabilising horizontal force “g” times the weight of the assumed failure mass, inconsistencies in unit weight data may produce earthquake forces which are unrepresentative of the real situation.

The second possibility is that while the Edgecumbe earthquake may have produced earthquake forces of 0.33 g, watertable conditions and/or D may not have been appropriate to produce combinations leading to failure of the volcano slopes. It is likely; however, that the Edgecumbe earthquake may have resulted in weakening of the volcano edifice thereby lowering its ability to withstand such strong earthquake forces in the future. This means that the conditions of failure graphs do represent Putauaki adequately at present.

Conditions of failure graphs for profiles 4 and 5 indicated that under conditions of  $D > 0.8$  and  $D > 0.9$  respectively, neither slope could achieve stability irrespective of earthquake forces and watertable elevation. For profile 6a, conditions of failure graphs indicated that given a value of  $D < 0.4$ , unrealistically high earthquake forces and watertable elevations were required to promote instability. The level of disturbance to which the rock masses of Putauaki have been exposed is likely to vary throughout the edifice making it difficult to assign a single D value to represent Putauaki. If a single D value was to be selected, it would most likely lie between  $D = 0.4$  and  $D = 0.8$ ; a range by which all slope profiles are currently stable, but when exposed to realistic earthquake forces and watertable elevations, exhibit the potential to become unstable. Thus, this study argues that an

intermediate D value of 0.6 is most realistic for Putauaki. Geotechnical studies of jointed lavas at other volcanoes have determined similar D values of 0.7 (White Island, New Zealand (Moon *et al.* 2005)) and 0.6 (Stromboli Island, Italy (Apuani *et al.* 2005)).

Table 6.4 – Conditions promoting failure for slope profiles showing potential for large scale failure.

Profile	D	Earthquake force (g)	Watertable elevation (%)
4	0	Moderate earthquake forces (0.2 – 0.16 g)	Increasing watertable elevation decreases critical earthquake force
	0.5	Low earthquake forces (0.1 – 0.07 g)	
	0.8	Very low earthquake forces (< 0.01 g). No earthquake force required if watertable elevation > 12%	
	> 0.8	Stability unachievable irrespective of earthquake force and/or watertable elevation	
4a	0	High earthquake forces (0.275 – 0.26 g)	A watertable elevation less than 15% has little effect on instability
	0.5	Moderate earthquake forces (0.18 – 0.165 g)	
	1	Very low earthquake forces (0.01 – 0.0 g). No earthquake forces required if watertable elevation > 15%	
5	0	High earthquake forces (0.255 – 0.21 g)	Increasing watertable elevation decreases critical earthquake force
	0.5	Moderate earthquake forces (0.15 – 0.12 g)	
	0.9	Very low earthquake forces (< 0.023 g). No earthquake force required if watertable elevation > 9%	
	> 0.9	Stability unachievable irrespective of earthquake force and/or watertable elevation	
5a	0	High earthquake forces (0.29 – 0.24 g)	Increasing watertable elevation decreases critical earthquake force
	0.5	Moderate earthquake forces (0.19 – 0.15 g)	
	0.1	Very low earthquake forces (< 0.007 g). No earthquake force required if watertable elevation > 3%	
6	0	High to moderate earthquake forces (0.27 – 0.235 g)	Increasing watertable elevation decreases critical earthquake force
	0.5	Moderate earthquake forces (0.58 – 0.45 g)	
	0.1	Very low earthquake forces (< 0.015 g). No earthquake force required if watertable elevation > 5%	
6a	< 0.4	Unrealistically high earthquake forces (0.415 g)	A watertable elevation less than 15% has no effect on instability
	0.5	Very high earthquake forces (0.3 g)	
	0.1	Moderate earthquake forces (0.15 g)	

# CHAPTER 7

# *RISK ANALYSIS*

---

## **7.1 INTRODUCTION**

The central aim of this research was to assess the stability of Putauaki and analyse the risk associated with collapse of the volcanic edifice. In order to achieve this aim, four objectives were defined:

- 1) geomorphological and geotechnical mapping;
- 2) determination of strength parameters for each lithotechnical unit;
- 3) production of stability models; and
- 4) analysis of the risk associated with volcanic landslide from Putauaki.

This chapter will in turn summarise the results attained for objectives (1) – (3), after which the final objective (4) will be discussed.

## **7.2 GEOMORPHOLOGY AND GEOLOGY**

Objective one: *to construct a geomorphic and geological map of Putauaki establishing structure and field geotechnical properties of individual lithotechnical units.*

Geomorphic mapping (Figure 4.1) shows that the landscape surrounding Putauaki, representing the eroded upper surface of the Matahina Ignimbrite, is strongly dissected. A strong south-west to north-east tendency is apparent within the dissection pattern of the landscape. To the north-west of the volcano lies a deeply incised major alluvial valley marking the present day flow path of the Tarawera River. The approximate circumference and total volume of Putauaki is 10 km and 1.61 km<sup>3</sup> respectively. Geomorphic investigations found no evidence of past landslides (deposits and/or failure scarps) from Putauaki.

Putauaki consists of two primary features; Main Cone and Main Dome (Figure 4.2). The summit of Main Cone stands 821 m a.s.l. displaying slope angles ranging from 32 – 36°. Its eastern flank is characterised by a non-dissected, draped appearance while the north, south and west flanks portray an irregular topography of young valleys and ridges. Main Cone shows little evidence of significant erosion. Two small craters (one which is permanently infilled by a cool water lake) are present at the summit of Main Cone. Main Dome is situated at the base of the western flank of Main Cone. The summit of Main Dome reaches 420 m a.s.l. Slope angles of Main Dome approximate 24°. A crater is not present on Main Dome, nor is there any evidence of significant erosion.

Rock mass descriptions were carried out at a total of 33 sites on Putauaki. Tabulating the key features of rock mass descriptions for each site allowed definition of six lithotechnical units consisting of both hard rocks (indurated andesite, scoriaceous andesite, altered andesite and indurated dacite) and soft rocks (block and ash flow, and the Matahina Ignimbrite). Typical rock mass characteristics for each of these lithotechnical units are presented in Table 43. Correlation of each lithotechnical unit to its respective site location allowed the location and boundaries of each lithotechnical unit to be inferred (Figure 4.15).

### **7.3 GEOTECHNICAL PROPERTIES**

*Objective two: to determine the geotechnical properties of each lithotechnical unit identified using field and laboratory strength tests.*

The methods used to determine the geotechnical properties of each lithotechnical unit varied depending on whether the unit is categorised as a hard or soft rock. Geotechnical properties of hard rocks were obtained through a variety of methods including rock mass classification schemes (RQD, RMR and modified GSI), measurement of rock mass strength, Schmidt hammer tests, scanline surveys of discontinuity condition, point load testing, and bulk density and porosity measurements. Many of the above methods were inappropriate for the soft rocks due to their weak nature and lack of discontinuities. Geotechnical properties of soft rocks were therefore assessed through measurement of rock mass strength, direct shear strength tests, and bulk density measurements.

Hard rock intact strength was described using UCS,  $m_i$ , GSI and D, input variables required by RocLab<sup>TM</sup> to calculate Hoek-Brown, and equivalent Mohr-Coulomb parameters. Soft rock intact strength was described using the Mohr-Coulomb failure criterion ( $c$  and  $\phi$ ). The intact strength of the hard rocks was measured as  $15 \pm 1$  MPa (altered andesite),  $25 \pm 5$  MPa (scoriaceous andesite),  $44.7 \pm 0.9$  MPa (indurated dacite), and  $60 \pm 4$  MPa (indurated andesite); a range much lower than expected for lithologies of this type. This is most likely a result of the low unit weights (especially in the case of scoriaceous and altered andesite) and relatively high porosities exhibited by the hard rocks. The intact strength of the block and ash flow was measured as  $c = 0$  MPa and  $\phi = 42.1$ . The low  $c$  of this deposit most likely reflects the fact that it is a granular material, dominated by frictional behaviour. As a result,  $\phi$  of the block and ash flow is high, comparable with that of the upper range of published values. The intact strength of the Matahina Ignimbrite is  $c = 1.4 \times 10^{-3}$  MPa and  $\phi = 41.7^\circ$ . While  $\phi$  exceeds published ranges by only  $1.74^\circ$ , the value for  $c$  is much lower than published values. The high variability of ignimbrite deposits as a whole may explain the measured intact strength of the Matahina Ignimbrite.

A complete summary of geotechnical properties for each lithotechnical unit is presented in Table 5.12.

## 7.4 GALENA MODELLING

Objective three: *to produce stability models of Putauaki determining likelihoods of collapse.*

Using ArcGIS<sup>TM</sup>, five run-lines representing the paths of five topographical profiles were produced. Each run-line was divided in two producing a total of 10 slope profiles. Galena<sup>TM</sup> models each slope profile two dimensionally positioning horizontal distance along the run-line on the x-axis and elevation on the y-axis. Subsurface stratigraphy for each slope profile was inferred based upon evidence from geomorphic mapping, and an understanding of the age, nature, and succession of each lithotechnical unit as discussed in Chapter 4. Intact strength parameters defined in Chapter 5 for each lithotechnical unit were entered into Galena<sup>TM</sup> as material properties. For each slope profile, the Bishop Simplified

multiple method for circular failure was applied to identify the failure surface with the lowest factor of safety. The failure surface which showed the lowest factor of safety and represented the largest scale of failure, was selected to be the final failure surface on which stability assessment for that slope profile was based ( $F_{\min}$ ). Using the Bishop Simplified single method for circular failures, Galena<sup>TM</sup> assessed the sensitivity of  $F_{\min}$  to earthquake force, watertable elevation, and D.

It was determined that as a group, the 10 slope profiles showed the potential for two different scales of failure; small scale failures ( $< 0.1 \text{ km}^2$  of material), and large scale failure ( $> 0.1 \text{ km}^2$  of material). Four slope profiles showed potential for small scale failure (profiles 2, 2a, 3, and 3a) while the remaining six profiles showed potential for large scale failure (profiles 4, 4a, 5, 5a, 6 and 6a). Due to the greater vulnerability associated with large scale failures relative to small scale failures, stability assessment proceeded with those profiles showing potential for large scale failure only. For each of the six slope profiles showing potential for large scale failure, conditions of failure graphs were constructed to portray the effect that different combinations of earthquake force (ranging from 0 – 0.4 g), watertable elevation (ranging from 0 – 100 % slope saturation) and D (ranging from 0 – 1) may have on the stability of the slope. The conditions of failure graphs also identify those combinations which are deemed to be realistic for Putauaki and those combinations deemed to be unrealistic. Based on published literature, realistic levels of earthquake force and watertable elevation as defined in this study are 0.33 g and 15 % respectively.

The conditions of failure graph for profiles 4, 4a, 5, 5a, 6, and 6 indicated that irrespective of the level of D, realistic combinations of earthquake force and watertable elevation are capable of promoting an unstable slope. Conditions of failure graphs for profiles 4 and 5 indicated that under conditions of  $D > 0.8$  and  $D > 0.9$  respectively, neither slope could achieve stability. The conditions of failure graph for profile 6a indicated that at a  $D < 0.4$ , unrealistic combinations of earthquake force and watertable elevation must be achieved to promote an unstable slope. Based on these observations, it is argued that a D values 0.6 is representative of Putauaki. The fact that Putauaki has not undergone large scale

failure to date suggests that the constructed models overestimate the influence of those factors which promote slope instability.

## **7.5 RISK ANALYSIS**

Objective four: *based on the mapping and modelling above, analyse the risk posed to surrounding communities associated with a volcanic landslide from Putauaki.*

The remainder of this chapter will be directed towards analysing the risk associated landslide run-out from Putauaki. Methods of estimating landslide run-out distance are discussed, after which the influence of topography on landslide run-out distance and flow path will be addressed. Estimated depths of landslide deposits are estimated. In conclusion, the impacts associated with landslides sourced from Putauaki are discussed, after which the risk posed by a landslide from each slope profile will be categorised.

### **7.5.1 ESTIMATION OF LANDSLIDE RUN-OUT DISTANCE**

An essential part of risk analysis involving volcanic landslides is anticipation of the likely run-out distance and flow path of failed material. Many methods have been used for forecasting landslide run-out including coefficient of friction calculations (ratio of fall height to travel distance, or H/L ratios) (Sousa & Voight 1995; Vallance *et al.* 1995; Ui *et al.* 2000; Siebert 2002) and scale modelling of physical substances (Clague & Denlinger 1994; Keller *et al.* 1998; Pudasaini *et al.* 2005). Iverson *et al.* (1997) designed a method for delineating lahar hazard zones in valleys which involves using simple equations to calculate the inundated valley cross-sectional area and planimetric area as functions of lahar volume. However, as the mobility of lahars far exceeds that of dry landslides, there is difficulty extending this method to landslides sourced from Putauaki.

Recently, numerical methods have become popular in the prediction of run-out for their ability to provide insight into the complex physical processes involved in the mobility and emplacement of volcanic landslides (Legros 2001; Pitman *et al.* 2003; Pudasaini *et al.* 2005). However, while many studies involving numerical models identified mechanisms that are important in some specific landslide

events, the lack of a widely recognised universal approach means the debate over the prediction of landslide run-out continues.

The scope of this research does not extend as far as to account for numerical or scale modelling of landslide run-out. H/L ratios; however, as measured from the top of the prefailure surface to the distal end of the landslide deposit (Figure 7.1), are easily obtained, require few assumptions and have been used as a first approximation of likely travel distance for landslide risk assessment purposes (Siebert 2002). This study will incorporate H/L ratios to estimate potential run-out distances of landslides sourced from Putauaki. It is important to note that while H/L ratios are a proven simple means with which to estimate run-out, recent examples in the international literature of applying H/L ratios to landslide run-out are rare, most likely a result of the increasing use of numerical models.

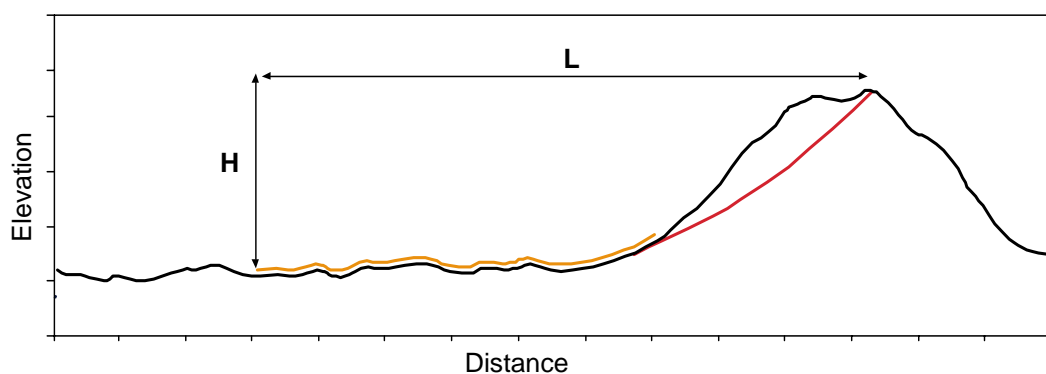


Figure 7.1 – Schematic representation of the procedure used to calculate the H/L ratio of a potential landslide. H/L ratios are calculated as the distance from the top of the prefailure surface to the distal end of the landslide deposit. Red line represents failure surface. Brown line represents landslide deposit.

#### 7.5.1.1 SELECTION OF H/L RATIO

A relationship between H/L ratio and failure volume of volcanic landslides has been noted by Siebert (2002) (Figure 7.2). Prefailure, the precise volume of material associated with a landslide is not readily determined. Galena models do not help this situation as failure surfaces are only modelled in two dimensions (length and depth below surface). Further difficulty arises from the fact that morphology of failure surfaces varies widely, and as a result so too does failure volume. A constant trend; however, is that failure scarps of volcanic landslides

are larger in the direction of the breach (length) than they are in width (Siebert 1984). In Chapter 6, the approximate area of  $F_{\min}$  was calculated based on chord length (the straight line distance between the uppermost and lowermost points of  $F_{\min}$ ) and segment height (the maximum depth with which  $F_{\min}$  is present below the slope surface at any one point) (Table 6.1; Figure 6.10). Using the approximate areas of  $F_{\min}$ , and assuming a failure plane width no greater than its length (or chord length) (as suggested by Siebert (1984)), an approximate maximum failure volume can be inferred for  $F_{\min}$  of each slope profile (Table 7.1). Based on Figure 7.2, these inferred maximum failure volumes correlate to an H/L ratio of approximately 0.12.

Thus, in the case of Putauaki, an H/L ratio of 0.12 would represent a maximum run-out (or worst case scenario) as it assumes a maximum volume. The question to then ask is what H/L ratio is suitable to predict minimum run-out?

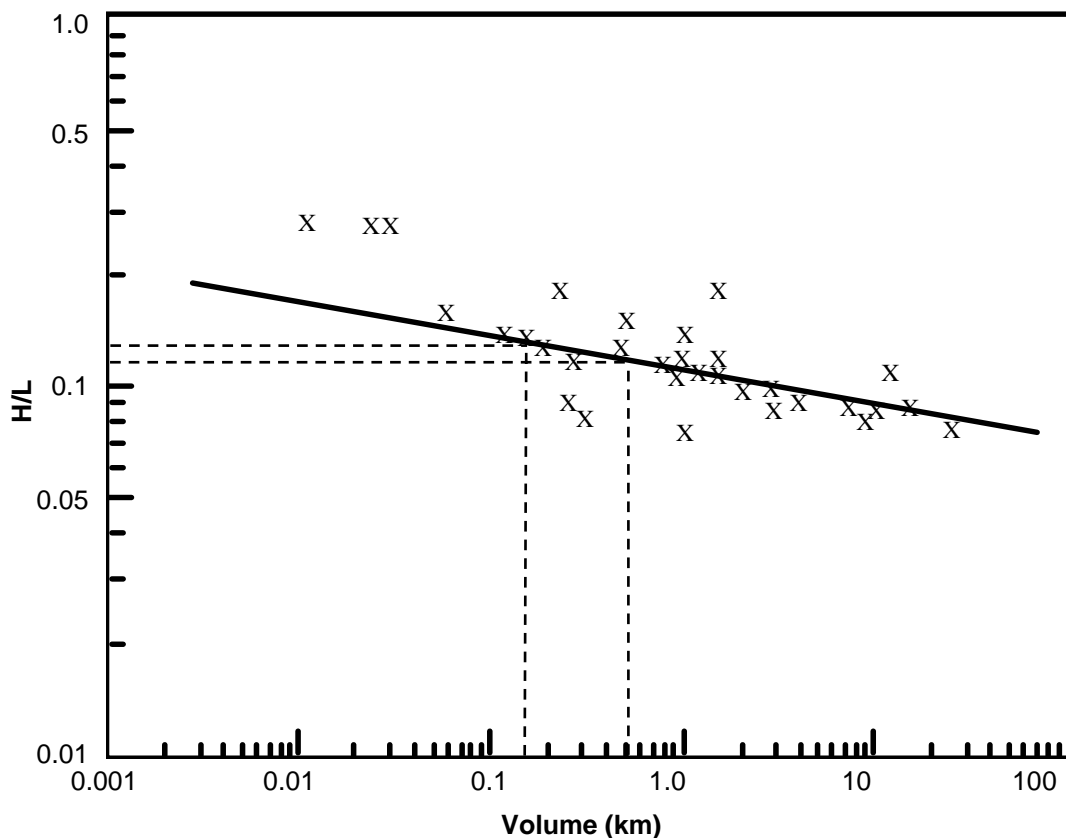


Figure 7.2 – Log-log relationship between ratio of fall height (H) and travel distance (L) to volume of debris-avalanche deposits ( $n = 32$ ). Dashed lines indicate approximate range of H/L ratios applicable for landslides sourced from Putauaki. Sourced from Siebert (1984).

It is reported that, in general, the maximum failure volume of subaerial volcanoes does not exceed 10 % of the edifice volume (Figure 7.3), thus for simplicity Siebert (1996) categorised volcanic landslides as belonging to one of two size classes; large volume landslides  $> 1 \text{ km}^3$  (sourced from volcanic edifices  $> 10 \text{ km}^3$ ), or small volume landslides  $< 1 \text{ km}^3$  (sourced from volcanic edifices  $< 10 \text{ km}^3$ ). Putauaki fits into the latter category of small volume landslides as the volume of its edifice is approximately  $1.61 \text{ km}^3$  (Duncan 1970).

For small volume landslides, a value for H (fall height) can be inferred from the difference between the summit of a failure surface and an arbitrary distance 10km in the direction of failure (the average travel distance for small volume landslides) (Siebert 1996). However, prefailure a value for L (travel distance) is unknown. Potentially, values for L may be based on past landslides from the volcano. Geomorphic mapping shows this is not a valid option for Putauaki. Alternatively, Siebert (1996) showed that H/L ratios for small volume Quaternary landslides range from 0.09 – 0.18. Applying an H/L ratio of 0.18 would estimate a realistic minimum run-out whereas application of an H/L ratio of 0.09 would calculate a realistic maximum run-out. In fact, an H/L ratio of 0.09 would suggest a greater maximum run-out than the H/L ratio 0.12 calculated previously in Section 7.5.1.1.

Table 7.1 – Approximate area, chord length, maximum width and maximum volume of  $F_{\min}$  for slope profiles 4, 4a, 5, 5a, and 6. The width of  $F_{\min}$  cannot exceed its length thus a maximum width can be inferred. Using average area, and maximum width of  $F_{\min}$ , an approximate maximum failure volume can be inferred for  $F_{\min}$ .

Profile	Area ( $\text{km}^2$ )	Chord length (km)	Maximum width (km)	Maximum volume ( $\text{km}^3$ )
4	0.102	1.33	$< 1.33$	0.14
4a	0.161	1.32	$< 1.32$	0.21
5	0.127	1.58	$< 1.58$	0.20
5a	0.113	1.29	$< 1.29$	0.15
6	0.214	2.00	$< 2.00$	0.43
6a	0.108	1.34	$< 1.34$	0.14

The H/L ratio of 0.12 (proposed previously in Section 7.5.1.1 to represent maximum run-out for a landslide sourced from Putauaki), is based on approximate

maximum volumes. Alternatively, the H/L ratio of 0.09 proposed by Siebert (1996), is based on data from a catalogue of around 200 landslides. Evidence supporting the selection of H/L ratio of 0.09 to represent maximum run-out for a small volume landslide is therefore much greater than the evidence supporting selection of an H/L ratio of 0.12. Thus, to reflect a worst case scenario, maximum run-out was calculated using an H/L ratio of 0.09.

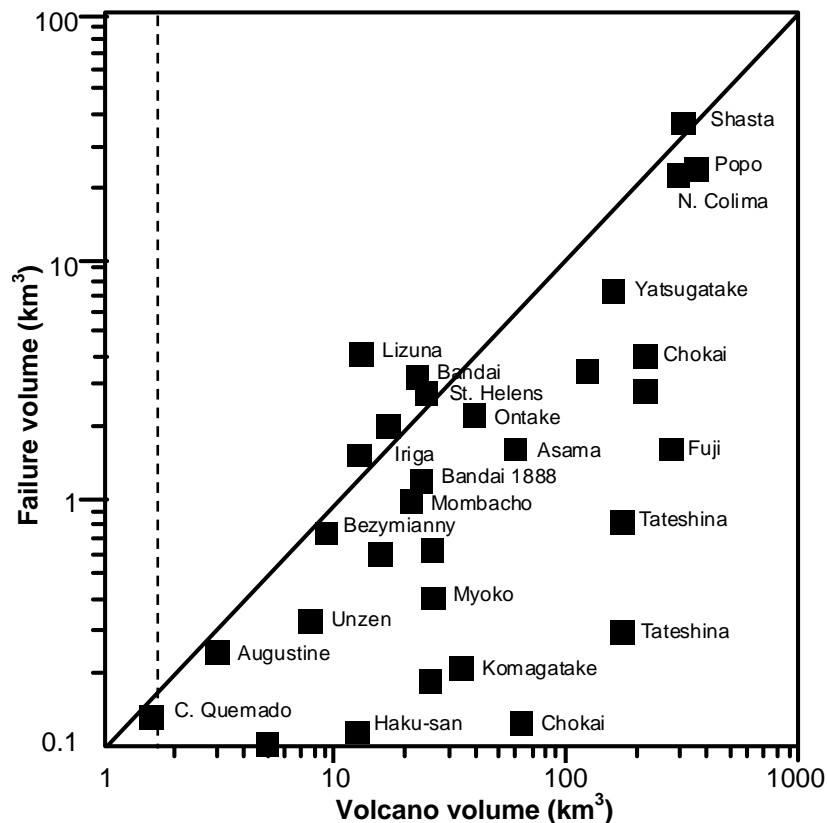


Figure 7.3 – Volume of prefailure edifice compared to collapse volume. Dashed line represents approximate volume of Putauaki edifice. Diagonal line represents 1:10 ratio of failure volume to volcano volume, otherwise interpreted as a failure volume 10 % of the volcano volume. Precise volumes are difficult to obtain, and failure of more than 10% of the edifice is possible. Sourced from Siebert (1984).

For each slope profile, a value to represent H was measured and incorporated with H/L ratios of 0.09 and 0.18 to calculate maximum and minimum run-out distances respectively (Table 7.2). Predicted maximum and minimum run-out distances are illustrated in Figure 7.4.

Table 7.2 – H/L estimates of maximum ( $L_{\max}$ ) and minimum ( $L_{\min}$ ) run-out of landslides sourced from each slope profile. ‘Elevation 10 km from failure surface summit’ is measured in the down-slope direction of collapse.

Profile	A = Elevation of failure surface summit (m)	B = Elevation 10km from failure surface summit (m)	A - B = H (m)	H/L = 0.09	H/L = 0.18
				$L_{\max}$ (km)	$L_{\min}$ (km)
4	750	160	590	6.56	3.28
4a	740	120	620	6.89	3.44
5	770	190	580	6.44	3.22
5a	750	220	530	5.89	2.94
6	750	10	740	8.22	4.11
6a	750	120	630	7.00	3.50

### 7.5.1.2 TOPOGRAPHICAL EFFECTS ON LANDSLIDE RUN-OUT

Predicting landslide run-out using H/L ratios provides a predicted travel distance of failed material moving down-slope in a direct line from the failure scarp (Figure 7.4). However, it is expected that the likely travel path of a landslide will not be in a direct line from its failure source, but rather be directed by the twists and curves of the complicated surface topography over which it is flowing (Crosta *et al.* 2004; Pudasaini *et al.* 2005). The effect that the topography surrounding Putauaki may have on the run-out of a landslide must be addressed.

It seems fair to suggest that landslides are likely to travel down major valleys away from the volcano (Siebert *et al.* 1987), perhaps an important point when acknowledging the strongly dissected landscape surrounding Putauaki. It has also been suggested that the cross sectional geometry of the channel close to run-out zones will have an effect on landslide run-out (Clague & Denlinger 1994). Undoubtedly the role of vertical accelerations in debris run-up will be important in determining which features of the landscape will direct the flow and which will be inundated (Iverson *et al.* 1997). Whether these factors will increase or decrease landslide run-out, and to what scale, is a question that is difficult to quantify. Traditionally, an understanding of topographical effects on landslide run-out involved review of historical records as well as field identification of run-out and inundation limits of historic events. More recently, physical and numerical models have been applied to the situation with the general consensus

being that additional work is required to find solutions that satisfy the complex field situation (Gray *et al.* 1998; Crosta *et al.* 2003; Crosta *et al.* 2004). Neither review of historical records nor modelling of run-out distances are valid options for this research.

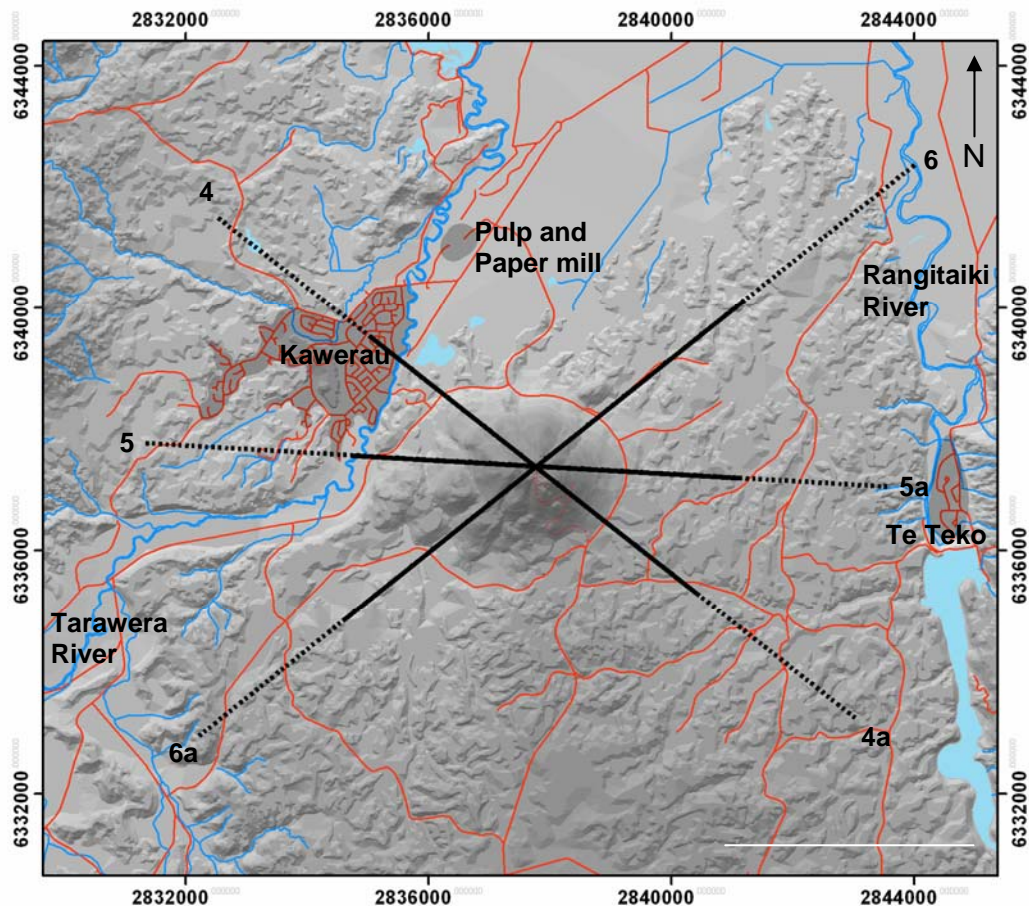
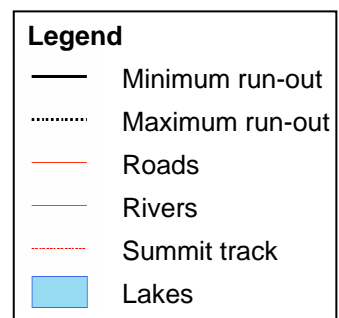


Figure 7.4 – DEM illustrating predicted maximum and minimum run-out distances of landslides sourced from each slope profile. Run-out predicted using H/L ratio. Numbers represent respective slope profile. White line represents 4 km.



In determining landslide run-out zones, two assumptions have been made. Firstly, it is assumed that potential landslides will follow what Parry *et al.* (2002) refer to as a ‘credible flow path’, or a general downhill path followed by surface water.

For example, a landslide flow path down a major ridge line, rather than descending into the catchment on either side of the major ridge line, would not be credible. Secondly, maximum and minimum run-out distances as predicted by H/L ratios of 0.09 and 0.18 respectively have been assumed (Table 7.2). While it is likely that run-out distance may vary along a tortuous channel, a lack of models and past landslide deposits means the scale to which run-out may vary is unknown.

Positioning of each run-out zone was undertaken in ArcGIS<sup>TM</sup>. Importing a pre-existing NZMS 260 1:50,000 dataset for contours (20 metre intervals) into GIS aided interpretation of the most credible flow path for a landslide sourced from Putauaki. It is accepted that landslides are predominantly gravity driven; therefore it may be assumed that debris will generally be transported in a down-slope direction. Contour lines adjoin points of equal elevation, thus it is possible for debris run-out to parallel a contour representing the same elevation at which run-out is occurring. However, debris is unlikely to be transported up-slope of a contour. If at any time run-out is found to be up-slope of a contour 'x', debris will proceed down-slope to contour 'x' after which they will parallel contour 'x' until the time comes again where by run-out is found to be up-slope of a contour.

This approach is illustrated in Figure 7.5. It can be seen how debris sourced from a landslide occurring at location 'A' is up-slope of the 80 m contour. Debris will travel down-slope to the 80 m contour after which the path of debris will parallel the 80 m contour for a short distance. At location 'B', the run-out path of debris is found to be up-slope of the 60 m contour. Debris will therefore travel down-slope to the 60 m contour, after which debris will parallel the 60 m contour. At location 'C' debris is found to be up-slope of the 40 m contour. Run-out will therefore travel down-slope to the 40 m contour, after which run-out will parallel the 40 m contour till the time comes whereby run-out is found to be up-slope of the 20 m contour (location 'D'). The run-out zone for each slope profile was mapped using this approach. The length of minimum and maximum run-out zones for each slope profile correlates to the approximate distance predicted by  $L_{\min}$  and  $L_{\max}$  for the profile in question (Table 7.2).

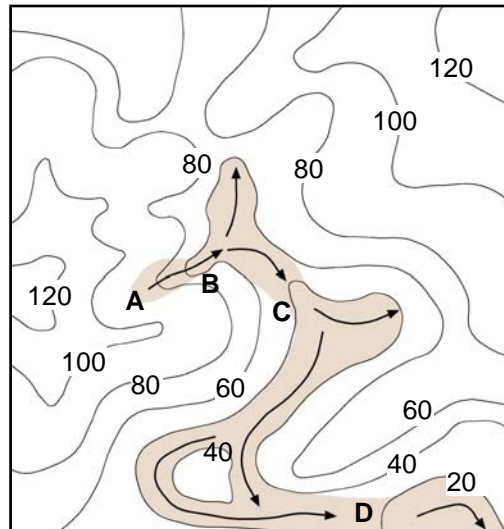


Figure 7.5 – Schematic representation of the procedure used to position landslide run-out zones (brown shaded region). Numbers refer to contour elevations. Arrows represent direction of run-out. Locations A, B, C and D relate to discussions in Section 7.5.1.2

Assuming credible flow paths and H/L ratios of 0.09 and 0.18, maximum and minimum run-out zones have been determined (Figure 7.6). The origin of each run-out zone represents the lower end of the respective failure surface. Run-out zones can be categorised into one of three groups; those that are to the south-west, east or north-west of Putauaki. The risks associated with each of these run-out zones will be analysed in Section 7.5.3.

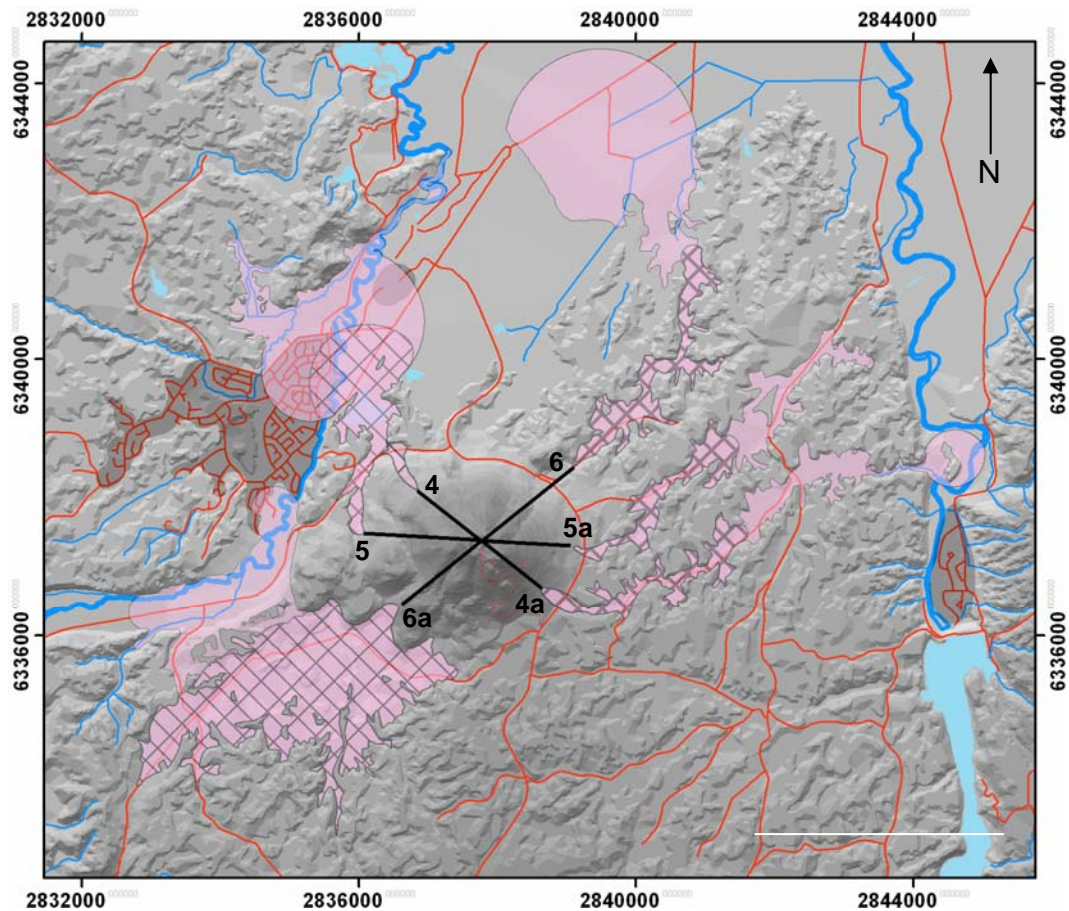


Figure 7.6 – DEM illustrating predicted maximum (pink zone) and minimum (pink hatched zone) run-out zones of landslides sourced from each slope profile. Run-out zones predicted using H/L ratio and the ‘credible flow path’ concept. Numbers indicate respective slope profiles and run-out zones. White line represents 4 km. Map legend is same as that for Figure 7.4.

### 7.5.2 ESTIMATION OF LANDSLIDE RUN-OUT DEPTH

In Table 7.1, maximum failure volumes for each slope profile were presented. Positioning of run-out zones was undertaken in ArcGIS™, therefore an ‘apparent’ (or planimetric) area of each run-out zone can be easily measured. A VBA (visual basic for applications) statement located in the help menu of ArcGIS™ was used to calculate the apparent area of each run-out zone. By using the maximum failure volumes presented in Table 7.1, and the apparent area of each run-out zone as measured in GIS, an average depth of run-out debris can be calculated for each run-out zone (Table 7.3). It is important to note that the average depths presented in Table 7.3 assume a maximum failure volume.

Table 7.3 – Estimated depths of landslide deposits sourced from each slope profile. Depths assume maximum volumes presented in Table 7.1. Bracketed values represent minimum run-out zones. All values in km.

<b>Profile</b>	<b>Maximum volume (km<sup>3</sup>)</b>	<b>Apparent area of run-out zone (km<sup>2</sup>)</b>	<b>Average depth (m)</b>
4	0.14	5.26 (1.9)	27 74
4a	0.21	2.24 (0.85)	94 247
5	0.20	5.36 (2.01)	37 100
5a	0.15	1.68 (0.77)	89 195
6	0.43	6.85 (1.18)	63 364
6a	0.14	8.76 (5.99)	16 23

### 7.5.3 RISK ANALYSIS

#### 7.5.3.1 SOUTH-WESTERN RUN-OUT ZONE: PROFILE 6a

Profile 6a represents the south-west flank of Putauaki. The topography to the south-west of Putauaki is dissected; however, dissection is subdued offering little lateral confinement in the form of major valleys and/or ridges. In the event of a landslide from profile 6a, landslide debris would most likely expand laterally. Lateral expansion of debris may potentially limit down-slope run-out distance, making it difficult to estimate a total travel distance. Thus, while run-out distance is calculated based on H/L ratio which assumes flow in a straight line down-slope of the failure surface, lateral expansion of landslide debris means the run-out zone illustrated in Figure 7.7 most likely overestimates the size of the area affected.

Figure 7.7 shows how landslide debris sourced from profile 6a will initially be contained within an area of subdued dissection, essentially infilling the depression. Assuming landslide debris exceeds minimum predicted run-out, failed debris will follow the most credible flow path and be redirected into the Tarawera River valley, after which run-out will be directed predominantly down-river to the north (Figure 7.7). Based on the widely spaced contour lines of the Tarawera River valley (showing a slight up-slope angle), the momentum of run-

out is expected to deposit an initial lobe of debris a short distance up-river (Figure 7.7). The Tarawera River valley may act to laterally confine debris, potentially increasing landslide run-out. However, lateral expansion in the early stages of run-out may lessen this effect. In the event of maximum run-out, only the most distal regions of landslide debris are predicted to reach the eastern extent of Kawerau Township (Figure 7.7). At this point it is appropriate to reiterate that run-out zones for profile 6a most likely overestimate the size of the area affected.

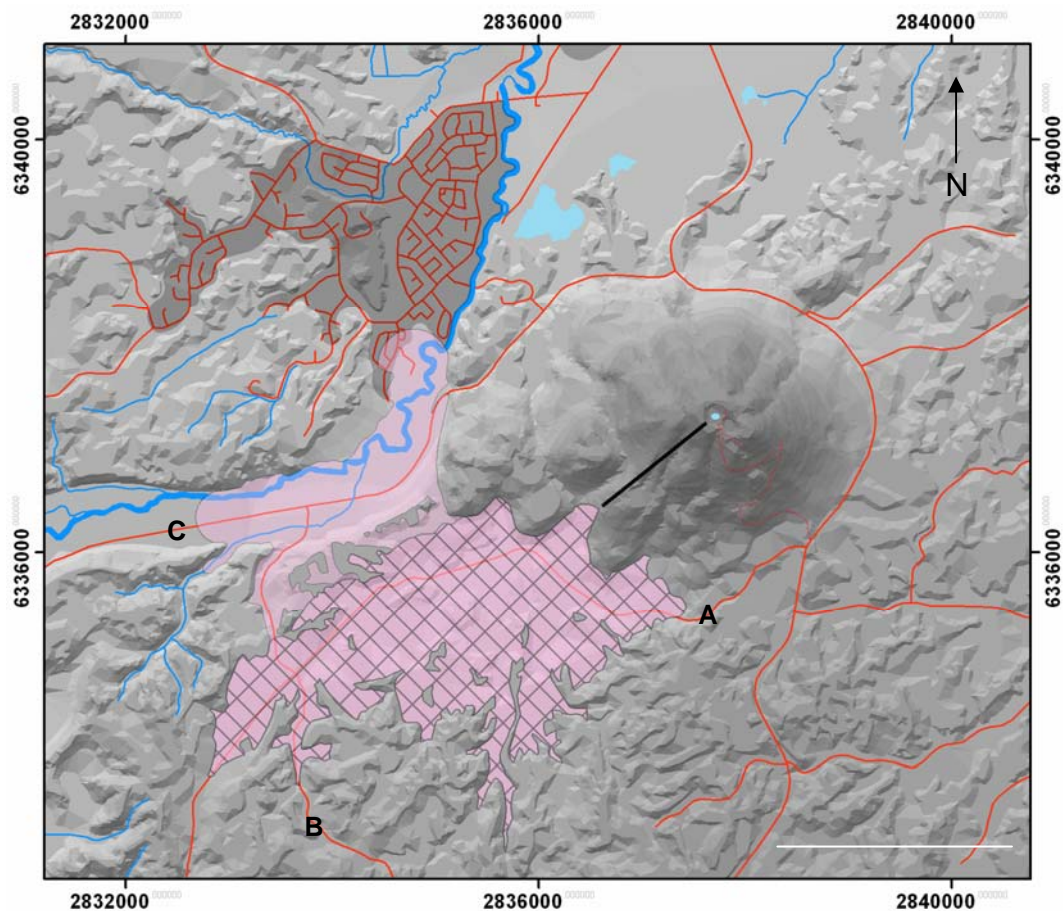


Figure 7.7 -- DEM illustrating maximum (pink zone) and minimum (pink hatched) run-out zones sourced from profile 6a. 'A' represents Putauaki Road. 'B' represents Centre Road. 'C' represents Tarawera Road. Black line represents failure surface of profile 6a. White line represents 2 km. Map legend is same as that for Figure 7.4.

While landslide run-out is unlikely to reach Kawerau Township, deposition of debris into the Tarawera River would undoubtedly pose secondary impacts to areas down-river, namely Kawerau Township and the Tasman Pulp and Paper mill, both of which are located on the low lying alluvial plains of the Tarawera

River valley. Secondary impacts include partial or total damming of the Tarawera River and associated flooding, subsequent failure of the debris dam, river diversion, and increased sedimentation down-river.

At present, land lying in the south-west run-out zone is predominantly used for forestry operations. Major forestry roads in this area include Putauaki Road and Centre Road (Figure 7.7). These roads are private access only; locked gates restrict public thoroughfare. However, the layout of forestry operations varies over time meaning so too does the degree to which a landslide may impact upon an area. Deposition of debris will also affect Tarawera Road; a relatively busy public access (by permit) road leading to Lake Tarawera, Tarawera Falls and popular lakeside camping locations. Tarawera Road is also a main transit route for forestry vehicles. A small risk may be posed to hunters working in the area.

When analysing the risk associated with a landslide sourced from profile 6a, an important fact to acknowledge is that in Chapter 6, conditions of failure graphs indicated that an earthquake force of at least 0.415 g (much > 0.33 g, the maximum intensity deemed to be realistic for Putauaki) is required to create unstable slope conditions (Figure 6.12b). Also it is noted that the run-out zone for profile 6a likely overestimates the size of the area affected. Add to this the fact maximum and minimum run-out from profile 6a will produce landslide deposits 16 and 23 m deep respectively (the shallowest depths of all run-out zones) (Table 7.3), and a potential landslide from profile 6a can be categorised as posing a relatively low risk.

#### **7.5.3.2 EASTERN RUN-OUT ZONES: PROFILES 4a, 5a AND 6**

Profile 6 represents the north-east flank of Putauaki. Landslide debris sourced from profile 6 would be well confined laterally, with run-out zones following the paths of major valleys (Figure 7.8). In the event that landslide debris attains only minimum predicted run-out, debris would be laterally confined within a valley for the entirety of its journey. In comparison, in the event that landslide debris attain maximum predicted run-out, the distal region of run-out would likely reach the Tarawera River valley, with a lobe of debris flowing out onto the alluvial plains.

While run-out may reach the Tarawera River Valley, debris is unlikely to be deposited into the Tarawera River (Figure 7.8).

Profiles 4a and 5a represent the south-east and eastern flanks of Putauaki respectively. As with profile 6, run-out from profiles 5a and 4a is largely confined laterally by major valleys (Figure 7.8). The entirety of the run-out zone for profile 5a shows lateral confinement irrespective of minimum or maximum predicted run-out. Similarly, the run-out zone for profile 4a is largely confined, the exception being the distal extent of run-out which is seen to enter the Rangitaiki River valley. If run-out was to reach the Rangitaiki River valley, a small amount of debris would be deposited in the river. The effects of this would be similar to those discussed for profile 6a in relation to the Tarawera River (Section 7.5.3.1); however, in the case of the Rangitaiki River, no townships or roads are present down-river. The township of Te Teko lays up-river of where debris is expected to enter the river valley. Thus the debris lobe is not expected to reach Te Teko. As lateral expansion of debris is largely restricted to these three slope profiles, a run-out closer to that of maximum predicted run-out may be more realistic.

McKee Road runs adjacent to the base of the eastern flanks of Putauaki (Figure 7.8). This road represents a main access route to and from the Pulp and Paper mill for logging trucks and forestry vehicles. Ideally, access to McKee Road is restricted; however, public vehicles often travel this road. Power lines supplying power to Kawerau Township and the Pulp and Paper mill run roughly adjacent to McKee Road. In a scenario where a landslide from any one of profiles 6, 5a or 4a attains only minimum predicted run-out, debris would still overrun McKee Road and the power lines by approximately 3.5 km (Figure 7.8).

Potentially, the distal ends of run-out zones for profiles 6 and 4a may infringe upon public access roads (such as Kawerau Road), as well as numerous farming and lifestyle blocks (especially in the case of profile 6). Debris would have to travel close to maximum predicted run-out for this to occur. A more likely scenario is for run-out to pose a risk to forestry roads. Numerous forestry roads are present in the run-out paths of these three profiles (such as Matata East Road),

the greatest potential impact being from the run-out zone of profile 4a which is seen to follow the same route as Redwood and McCrackens Roads (Figure 7.8). Profile 4a is also seen to be the only profile for which a landslide would destroy parts of the summit vehicle access track (Figure 7.8). This may pose problems for accessing telecommunication towers positioned at the summit of Main Cone.

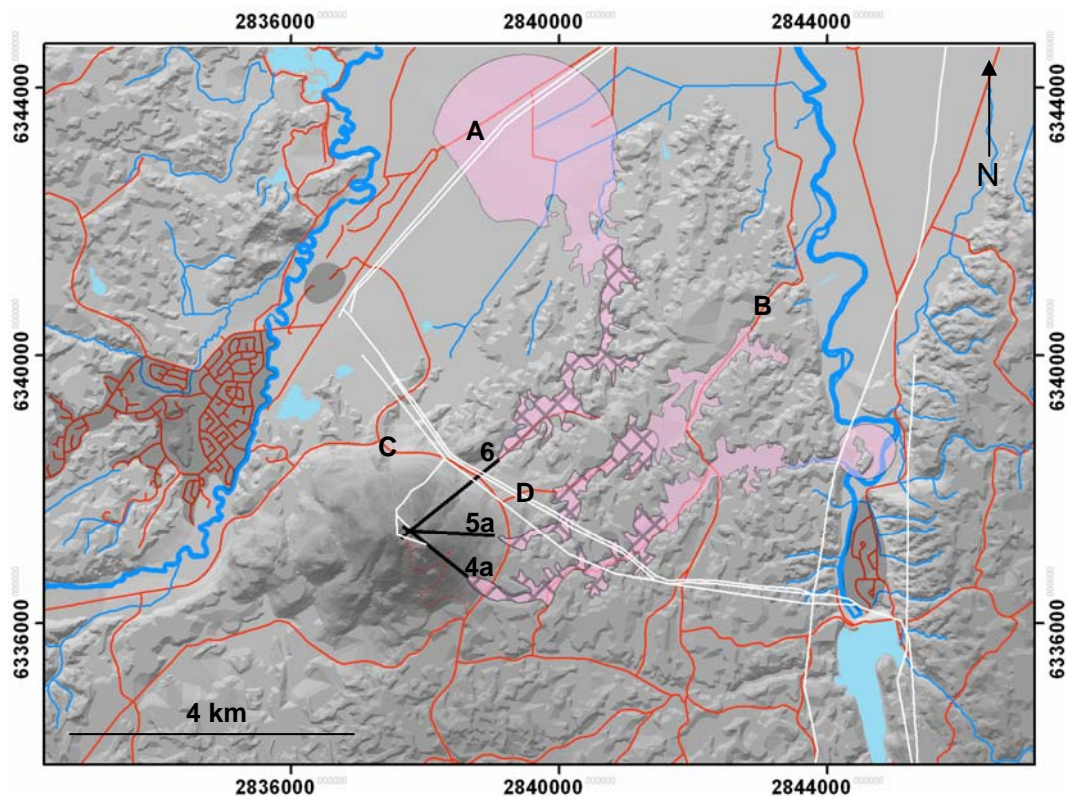


Figure 7.8 – DEM illustrating maximum (pink zone) and minimum (pink hatched) run-out zones sourced from profiles 4a, 5a and 6. ‘A’ represents Kawerau Road. ‘B’ represents McCracken Road. ‘C’ represents McKee Road. ‘D’ represents Matata East Road. Black lines represent failure surfaces of profiles 4a, 5a and 6 as labelled. White lines represent power lines. Map legend is same as that for Figure 7.4.

The risk associated with landslides from profiles 6, 5a and 4a has been categorised as relatively moderate. Justification of this categorisation is the suggestion that a landslide from any one of these slope profiles has the potential to not only pose a risk to private access forestry roads, but also inundate regularly travelled roads (McKee and Kawerau Roads) and disrupt local power supplies. While landslide debris sourced from these three profiles results in the thickest deposits of all six profiles (Table 7.3), the absence of any townships in the direct run-out zone limits the impact associated with these deposits.

### 7.5.3.3 NORTH-WESTERN RUN-OUT ZONES: PROFILES 4 AND 5

Profiles 4 and 5 represent the north-west and western flanks of Putauaki respectively. The failure scarps of these two slope profiles are situated on two different flanks; however, run-out zones of each profile are seen to merge at the base of the north-west flank (Figure 7.9). From this point on, landslide debris sourced from the two separate slope profiles follow identical run-out paths. Run-out from profiles 4 and 5 is laterally confined only in the early stages of flow, the majority of the run-out zone creating a laterally expanding debris out-flow lobe into the Tarawera River valley (Figure 7.9). H/L ratios predict that maximum run-out distances for profiles 4 and 5 differ by no more than 120 m (Table 7.2). The effect 120 m may have on a laterally expanding run-out lobe is presumed to be small given the precision of the H/L ratio. Thus, while run-out zones for these two slope profiles initiate at separate locations, once the separate flow paths have merged, the two run-out zones are treated as one.

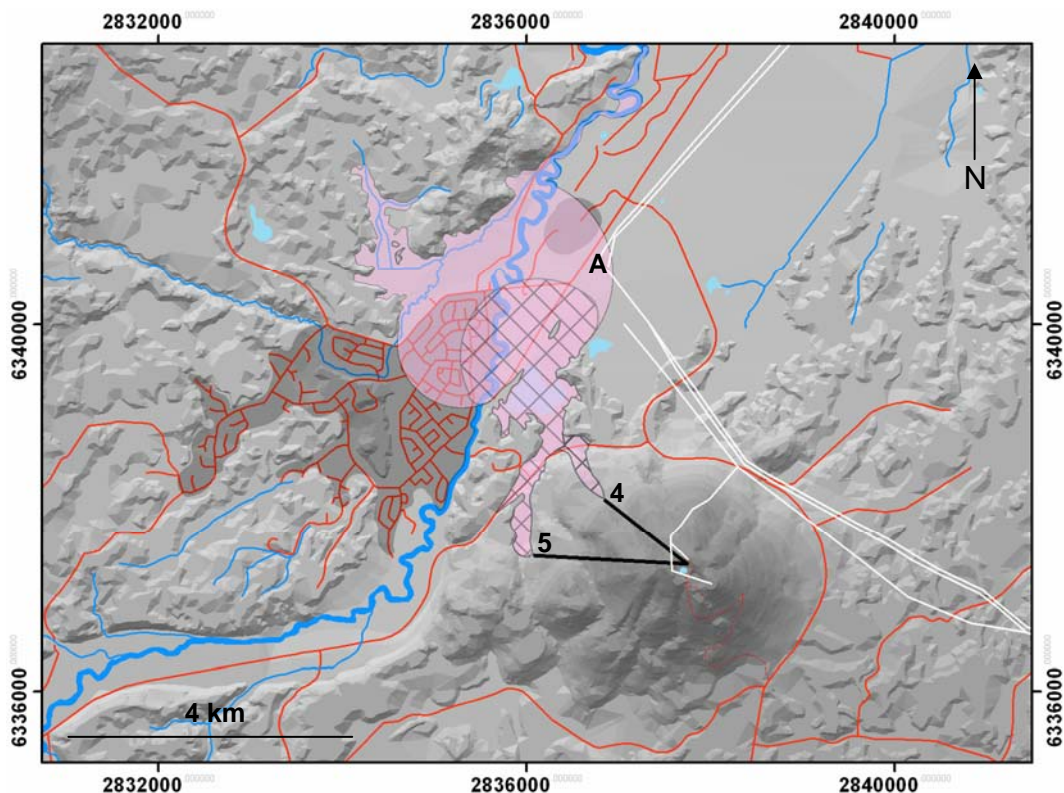


Figure 7.9 – DEM illustrating maximum (pink zone) and minimum (pink hatched) run-out zones sourced from profiles 4 and 5. ‘A’ represents power substation. Black lines represent failure surfaces of profiles 4 and 5 as labelled. White lines represent power lines. Map legend is same as that for Figure 7.4.

Landslides sourced from these two slope profiles are unique in the sense that they are the only landslides to exhibit run-out zones which encroach upon a large part of Kawerau Township and the pulp and paper mill. In fact, a landslide achieving only minimum predicted run-out will be sufficient to inundate the north-east parts of Kawerau Township and the south-west parts of the adjacent pulp and paper mill (Figure 7.9). If landslide run-out were to exceed minimum predicted run-out (which is very likely), the risk posed to Kawerau Township and the pulp and paper mill would be much greater with maximum run-out inundating approximately 25 % of the township, the entire pulp and paper mill and a local power substation (Figure 7.9).

Also unique to these two profiles is how minimum run-out zones reach a major river valley and associated river channel (in this case the Tarawera River valley). This is not seen for any other minimum run-out zones which all stop short of major river channels (Figure 7.6). The impacts associated with the deposition of debris into the Tarawera River are discussed in Section 7.5.3.1. Other impacts associated with landslides sourced from profiles 4 and 5 include disruption to Tarawera and McKee Roads. The impact upon forestry activities would be limited.

The key factor influential in the categorisation of the risks associated with a landslide from profiles 4 or 5 is the location of Kawerau Township and the pulp and paper mill. The risks associated with landslides from alternative slope profiles include debris infringing upon major river channels, regularly used transport routes and forestry activities. However, run-out zones of profiles 4 and 5 represent the only instance whereby landslide debris is likely to inundate parts of Kawerau Township and the pulp and paper mill. While the predicted thickness of landslide deposits sourced from profiles 4 and 5 were second and third lowest of all six profiles (approximately 32 m and 87 m thick for maximum and minimum run-out respectively), deposits of these depths would undoubtedly have an impact on Kawerau Township and the pulp and paper mill. Also, the critical earthquake force required to promote an unstable slope for profile 5 was 0.255 g, the second lowest critical earthquake force for all six slope profiles (Figure 6.14a).

It therefore seems appropriate to categorise the risk associated with a landslide from profiles 4 and 5 as relatively high.

## 7.6 SUMMARY

An essential part of risk analysis involving volcanic landslides is anticipation of the likely run-out distance and flow path of failed material. H/L ratios, as measured from the top of the prefailure surface to the distal end of the landslide deposit, are a proven simple means with which to estimate landslide run-out. This study incorporated H/L ratios, as well as the credible flow path concept (interpreted as the general downhill path followed by surface water), to define run-out zones for six potential landslides sourced from the flanks of Putauaki. The risk posed by these landslides was subsequently analysed and categorised.

Impacts identified include partial inundation of Kawerau Township by landslide debris, obstruction of the Tarawera River and regularly travelled roads, flooding; damage of power supplies to Kawerau Township and the pulp and paper mill, and disruption to forestry operations.

Risk categories ranged from relatively low to relatively high (Table 7.4). The run-out zone of a landslide sourced from profile 6a has the potential to enter the Tarawera River channel and affect public access and major forestry roads (Table 7.4). The conditions required to promote a landslide from this slope profile are; however, unrealistic, thus supporting a risk categorisation of relatively low. Landslides from profiles 4a, 5a and 6 have been categorised as posing a moderate risk due to their potential to inundate public access and major forestry roads, local power supplies and major river channels (Table 7.4). Landslide run-out zones from profiles 4 and 5 both showed potential to reach the Tarawera River channel, inundate public access and major forestry roads, and disrupt local power supplies. However, the fact that landslide debris is most likely to inundate the north-east parts of Kawerau Township and south-west parts of Tasman Pulp and Paper mill, is good justification for a relatively high risk categorisation. Based on the risk categories assigned to each slope profile, Figure 7.10 presents a final risk analysis map for landslides sourced from Putauaki.

Table 7.4 – Summary of landslide risk categorisation for each slope profile.

Amenities	Slope profiles		
	South-western run-out zone:6a	Eastern run-out zones: 4a, 5a and 6	North-western run-out zones: 4 and 5
Townships	No direct effects. Potential secondary effects include flooding of Kawerau Township in the event of landslide debris damming or diverting Tarawera River	Not affected	Minimum run-out will inundate north-east parts of Kawerau Township. Maximum run-out will inundate Tasman Pulp and Paper mill
Major rivers	Maximum run-out will reach Tarawera River potentially damming or diverting river flow path	Maximum run-out will reach Rangitaiki River (profile 4a) potentially damming or diverting river flow path	Minimum run-out will reach Tarawera River potentially damming or diverting river flow
Major roads	Forestry	Minimum run-out will inundate Putauaki, Tarawera and Centre Roads	Minimum run-out will inundate McKee, Matata East (profile 6) and McCracken Roads (profile 4a)
	Public	Maximum run-out will inundate Tarawera Road (public access by permit)	Maximum run-out will inundate Kawerau Road (profile 6)
Power supply	Not affected	Minimum run-out will inundate power supply to Kawerau Township and Tasman Pulp and Paper mill. Putauaki summit track accessing communication towers will be affected (profile 4a)	Minimum run-out will inundate local power substation controlling power supply to Kawerau Township and Tasman Pulp and Paper mill
Probability of conditions promoting instability	Unlikely	Likely	Likely
<b>Risk category</b>	<b>Relatively low</b>	<b>Moderate</b>	<b>Relatively high</b>

The risk analysis provided by this study incorporated a qualitative viewpoint of landslide run-out, ranking risks from relatively low to relatively high. Ideally a more quantitative interpretation is desirable. This would most logically be based on landslide volume; which would give an indication of not only run-out distance but also inundation areas and depths. An approach incorporating three dimensional stability models (such as 3-dimensional limit equilibrium analysis or 3DEC) would offer insight into potential failure volumes; an aspect that was difficult to measure in this study. In addition to 3-dimensional stability models, numerical models of run-out motion would provide a greater level of certainty (relative to H/L ratios) in understanding run-out over complicated natural topography. It would be an approach such as this that would represent the next step in analysing the risk associated with a volcanic landslide from Putauaki.

# *REFERENCES*

---

- Apuani T, Corazzato C, Cancelli A, Tibaldi A 2005. Stability of a collapsing volcano (Stromboli, Italy): Limit equilibrium analysis and numerical modelling. *Journal of Volcanology and Geothermal Research* 144: 191 – 210.
- Ayalew L, Yamagishi H, Marui H, Kannoc T 2005. Landslides in Sado Island of Japan: Part I. Case studies, monitoring techniques and environmental considerations. *Engineering Geology* 81(4): 419 – 431.
- Beanland S 1995. The North Island dextral fault belt, Hikurangi Subduction Margin, New Zealand. Unpublished PhD thesis, Victoria University of Wellington, Wellington.
- Begét J, Kienle J 1992. Cyclic formation of debris avalanches at Mount St Augustine volcano. *Nature* 356: 701 – 704.
- Best MG, Christiansen EH 2001. *Igneous Petrology*. Massachusetts, Blackwell Science.
- Bieniawski ZT 1973. Engineering classification of jointed rock masses. *Transactions of the South African Institution of Civil Engineers* 15: 335 – 344.
- Bieniawski ZT 1989. *Engineering rock mass classifications: a complete manual for engineers and geologists in mining, civil and petroleum engineering*. New York, John Wiley and Sons.
- Bradshaw J 2004. Aspects of slope stability for White Island Volcano, New Zealand. Unpublished MSc thesis, University of Waikato, Hamilton.

- 
- Brady BHG, Brown ET 2004. Rock mechanics for underground mining. Boston, Kluwer Academic Publishers.
- Brown ET ed. 1981. Rock characterization testing and monitoring. Germany, Pergamon Press.
- Burns D, Farquhar G, Mills M, Williams A eds. 2005. Field description of soil and rock. New Zealand Geotechnical Society.
- Burt RM, Brown SJA, Cole JW, Shelley D, Waight TE 1998. Glass-bearing plutonic fragments from ignimbrites of the Okataina caldera complex, Taupo Volcanic Zone, New Zealand: remnants of a partially molten intrusion associated with preceding eruptions. *Journal of Volcanology and Geothermal Research* 84(3 - 4): 209 – 237.
- Capra L, Macías JL, Scott KM, Abrams M, Garduno-Monroy VH 2002. Debris avalanches and debris flows transformed from collapses in the Trans-Mexican Volcanic Belt, Mexico: behavior and implications for hazard assessment. *Journal of Volcanology and Geothermal Research* (113): 81 - 110.
- Carol LD 1998. Volcanology, petrology, and petrochemistry of Mt. Edgecumbe volcano, Bay of Plenty, New Zealand. Unpublished MSc thesis, Victoria University of Wellington.
- Cas RAF, Wright JV 1987. Volcanic successions: modern and ancient. London, Allen and Unwin.
- Cecchi E, van Wyk de Vries B, Lavest J 2005. Flank spreading and collapse of weak-cored volcanoes. *Bulletin of Volcanology* 67: 72 – 91.
- Chang M 2003. Forest hydrology: an introduction to water and forests. CRC Press.

- 
- Clague DA, Denlinger RP 1994. Role of olivine cumulates in destabilizing the flanks of Hawaiian volcanoes. *Bulletin of Volcanology* 56: 425 – 434.
- Cole JW 1981. Genesis of lavas of the Taupo Volcanic Zone, North Island, New Zealand. *Journal of Volcanology and Geothermal Research* 10: 317 – 337.
- Cole JW 1990. Structural control and origin of volcanism in the Taupo Volcanic Zone, New Zealand. *Bulletin of Volcanology* 52: 445 – 459.
- Cooke RU, Doornkamp JC 1990. *Geomorphology in environmental management*. 2nd Edition. Oxford, Clarendon Press.
- Crosta GB, Chen H, Lee CF 2004. Replay of the 1987 Val Pola Landslide, Italian Alps. *Geomorphology* 60: 127 – 146.
- Crosta GB, Imposimato S, Roddeman DG 2003. Numerical modelling of large landslides stability and runout. *Natural Hazards and Earth System Sciences* 3: 523 – 538.
- Davidson J, De Silva S 2000. Composite volcanoes. In: Sigurdsson H, Houghton B, McNutt SR, Rymer H, Styx J eds. *Encyclopedia of volcanoes*. San Diego, Academic Press.
- Day SJ 1996. Hydrothermal pore fluid pressure and the stability of porous, permeable volcanoes. In: McGuire WJ, Jones AP, Neuberg J eds. *Volcano instability on the Earth and other planets*. Geological Society of London, Special Publication 110.
- De Silva S, Davidson JP, Croudace IW, Escobar A 1993. Volcanological and petrological evolution of Volcan Tata Sabaya, S.W. Bolivia. *Journal of Volcanology and Geothermal Research* 55: 305 – 335.
- Deere DU 1964. Technical description of rock cores for engineering purposes. *Rock Mechanics and Engineering Geology* 1(1): 17 – 22

- Duncan AR 1970. The petrology and petrochemistry of andesite and dacite volcanoes in eastern Bay of Plenty, New Zealand. Unpublished PhD thesis, Victoria University of Wellington, Wellington.
- Eberhardt E 2003. Rock Slope Stability Analysis - Utilization of Advanced Numerical Techniques. University of British Columbia.
- Elsworth D, Voight B 1995. Dyke intrusion as a trigger for large earthquakes and failure of volcano flanks. *Journal of Geophysical Research* 100: 6005 – 6024.
- Francis PW, Wells GL 1988. Landsat Thematic Mapper observations of debris avalanche deposits in the Central Andes. *Bulletin of Volcanology* 50: 258 – 278.
- Franklin JA 1985. Suggested method for determining point load strength. *International Journal of Rock Mechanics & Mining Sciences* 22(2): 53 – 60.
- Galena 2003. Galena version 3 for Windows, slope stability analysis system users guide. Clover Technology Limited, Australia.
- Gamble JA 1993. Seafloor geology and petrology in the oceanic to continental transition zone of the Kermadec-Havre-Taupo Volcanic Zone arc system, New Zealand. *New Zealand Journal of Geology and Geophysics* 36: 417 – 435.
- Gamble JA, Wright IC 1995. The Southern Havre Trough geological structure and magma petrogenesis of an active backarc rift complex. In: Taylor B ed. *Backarc Basins: Tectonics and Magmatism*. New York, Plenum Press.
- Gray JMNT, Wieland M, Hutter K 1998. Gravity-driven free surface flow of granular avalanches over complex basal topography. *Proceeding of the Royal Society of London. Series A* 455: 1841 - 1874.

- Hajdas I, Lowe DJ, Newnham RM, Bonani G 2006. Timing of the late-glacial climate reversal in the Southern Hemisphere using high-resolution radiocarbon chronology for Kaipo bog, New Zealand. *Quaternary Research* 65: 340 – 345.
- Hoek E 1994. Strength of rock and rock masses. *International Journal of Rock Mechanics and Mining Sciences News Journal* 2(2): 4 – 16.
- Hoek E, Brown ET 1980. Empirical strength criterion for rock masses. *Journal of Geotechnical Engineering Division ASCE* 106(GT9): 1013 – 1035.
- Hoek E, Brown ET 1997. Practical estimates of rock mass strength. *International Journal of Rock Mechanics and Mining Sciences* 34(8): 1165 – 1186.
- Hoek E, Carranza-Torres C, Corkum B 2002. The Hoek-Brown Failure Criterion - 2002 Edition. *Proceedings of the 5th North American Rock Mechanics Symposium and 17th Tunneling Association of Canada Conference: NARMS-TAC.*
- Hoek E, Diederichs MS 2006. Empirical estimation of rock mass modulus. *International Journal of Rock Mechanics and Mining Sciences* 43: 203 – 215.
- Hoek E, Kaiser PK, Bawden WD 1995. *Support of Underground Excavations in Hard Rock.* Balkema, Rotterdam.
- Hoek E, Wood D, Shah S 1992. A modified Hoek-Brown criterion for jointed rock masses. *Proceedings of the Rock Characterisation Symposium for the International Society of Rock Mechanics, Eurock, British Geotechnical Society.*
- Hürlimann M, Garcia-Piera JO, Ledesma A 2000. Causes and mobility of large volcanic landslides: application to Tenerife, Canary Islands. *Journal of Volcanology and Geothermal Research* 103: 121 – 134.

- 
- Hürlimann M, Ledesma A, Martí J 1999. Conditions favouring catastrophic landslides on Tenerife (Canary Islands). *Terra Nova* 11(2/3): 106 – 111.
- Hürlimann M, Martí J, Ledesma A 2004. Morphological and geological aspects related to large slope failures on oceanic islands: The huge La Orotava landslides on Tenerife, Canary Islands *Geomorphology* 62(3 – 4): 143 – 158.
- Iverson RM, Reid ME, LaHusen RG 1997. Debris-flow mobilization from landslides. *Annual Review of the Earth and Planetary Sciences* 25: 85 – 138.
- Kahraman S 2001. Evaluation of simple methods for assessing the uniaxial compressive strength of rock. *International Journal of Rock Mechanics and Mining Sciences* 38: 981 – 994.
- Keady G 1990. The Dupuit approximation for the rectangular dam problem. *Journal of Applied Mathematics* 44(3): 243 – 260.
- Keller S, Ito Y, Nishimura K 1998. Measurements of the vertical velocity distribution in ping pong ball avalanches. *Annals of Glaciology* 26: 259 – 264.
- Legros F 2001. The mobility of long-runout landslides. *Engineering Geology* 63: 301 - 331.
- López DL, Williams SN 1993. Catastrophic volcanic collapse: relation to hydrothermal processes. *Science* 260: 1794 – 1796.
- Lowry MA, Ede SC, Harris JS 1989. Assessment of seismic intensities resulting from the 1987 Edgecumbe earthquake, New Zealand, and implications for modernising the intensity scale. *New Zealand Journal of Geology and Geophysics* 32: 145 – 153.

- McVerry GH, Cousins WJ, Hefford RT 1989. Ground-motion accelerograph records from the 1987 Edgecumbe earthquake, Bay of Plenty, New Zealand. *New Zealand Journal of Geology and Geophysics* 32: 155 – 166.
- Moon V 1993. Microstructural controls on the geomechanical behaviour of ignimbrite. *Engineering Geology* 35(1 - 2): 19 – 31.
- Moon V, Bradshaw J, Smith R, de Lange W 2005. Geotechnical characterisation of stratocone crater wall sequences, White Island Volcano, New Zealand. *Engineering Geology* 81: 146 – 178.
- Moore JG, Normark WR, Holcomb RT 1994. Giant Hawaiian landslides. *Annual Review of Earth and Planetary Sciences* 22: 119 – 144.
- Nairn IA 1995. The probability and likely effects of a future eruption at Mt Edgecumbe (Putauaki). Institute of Geological and Nuclear Sciences.
- Oguchi CT, Matsukura Y 1999. Effect of porosity on the increase in weathering-rind thicknesses of andesite gravel. *Engineering Geology* 55: 77 - 89.
- Palmer BA, Alloway BV, Neall VE 1991. Volcanic-debris-avalanche deposits in New Zealand: Lithofacies organisation in unconfined, wet avalanche flows. In: Fisher RV, Smith GA eds. *Sedimentation in volcanic settings*. Society for Sedimentary Geology Special Publication.
- Parry S, King JP, Franks CAM, Shaw R 2002. Guidelines for natural terrain hazard studies. Hong Kong, Geotechnical Engineering Office, Civil Engineering Department, Government of Hong Kong. Report no. 138.
- Pitman EB, Nichita CC, Patra A, Bauer A, Sheridan MF, Bursik M 2003. Computing granular avalanches and landslides. *Physics of Fluids* 15(12): 3638–3646.

- 
- Priest SD, Hudson JA 1976. Discontinuity spacings in rock. *International Journal of Rock Mechanics and Mining Sciences and Geomechanics Abstracts* 13(5): 135 – 148.
- Pudasaini SP, Wang Y, Hutter K 2005. Rapid motions of free-surface avalanches down curved and twisted channels and their numerical simulation. *Philosophical Transactions of the Royal Society of London Series A* 363: 1551 – 1571.
- Reid ME, Christian SB, Brien DL 2000. Gravitational stability of three-dimensional stratovolcano edifices. *Journal of Geophysical Research* 105(B3): 6043 – 6056.
- Selby MJ 1993. *Hillslope materials and processes*. 2nd Edition. Oxford, Oxford University Press.
- Siebert L 1984. Large volcanic debris avalanches: characteristics of source areas, deposits, and associated eruptions. *Journal of Volcanology and Geothermal Research* 22: 163 – 197.
- Siebert L 1996. Hazards of large volcanic debris avalanches and associated eruptive phenomena. In: R S, Tilling R eds. *Monitoring and Mitigation of Volcano Hazards*. New York, Springer.
- Siebert L 2002. Landslides resulting from structural failure of volcanoes. In: Evans SG, DeGraff JV eds. *Catastrophic landslides: Effects, occurrence, and mechanisms* Geological Society of America.
- Siebert L, Glicken H, Ui T 1987. Volcanic hazards from Bezymianny- and Bandai-type eruptions. *Bulletin of Volcanology* 49: 435 – 459.
- Simkin T, Siebert L 1994. *Volcanoes of the world*. Geoscience Press, Arizona.

- 
- Simoni A, Houlsby G 2006. The direct shear strength and dilatancy of sand-gravel mixtures. *Geotechnical and Geological Engineering* 24: 523 – 549.
- Smith GA, Lowe DR 1991. Lahars: volcano-hydrologic events and deposition in the debris flow-hyperconcentrated flow continuum. In: Fisher RV, Smith GA eds. *Sedimentation in volcanic settings* Society for Sedimentary Geology.
- Sonmez H, Gokceoglu C, Ulusay R 2004. Indirect determination of the modulus of deformation of rock masses based on the GSI system. *International Journal of Rock Mechanics and Mining Sciences* 41: 849 – 857.
- Sonmez H, Ulusay R 1999. Modifications to the geological strength index (GSI) and their applicability to stability of slopes. *International Journal of Rock Mechanics and Mining Sciences* 36: 743 – 760.
- Sousa J, Voight B 1995. Multiple-pulsed debris avalanche emplacement at Mount St. Helens in 1980: Evidence from numerical continuum flow simulations. *Journal of Volcanology and Geothermal Research*. 24: 227 – 250.
- Stevenson RJ 1986. The geotechnical properties of Minden rhyolite at Pauanui and Onemana, eastern Coromandel. Unpublished Msc thesis, University of Waikato, Hamilton.
- Stoopes GR, Sheridan MF 1992. Giant debris avalanches from the Colima Volcanic Complex, Mexico: Implications for long-runout landslides (>100 km) and hazard assessment. *Geology* 20: 299 – 302.
- Swanson RH, Bernier PY, Woodard PD eds. 1987. *Forest hydrology and watershed management*. Oxfordshire, United Kingdom, International Association of Hydrological Sciences.

- Thomas M, Petford N, Bromhead EN 2004. Volcanic rock-mass properties from Snowdonia and Tenerife: implications for volcano edifice strength. *Journal of the Geological Society, London* 161: 1 – 8.
- Tomlinson AI, Sanson J 1994. Rainfall normals for New Zealand for the period 1961 to 1990. Report no. 3. Wellington, National Institute of Water and Atmosphere.
- Ui T, Takarada S, Yoshimoto M 2000. Debris avalanches. In: Sigurdsson H ed. *Encyclopaedia of Volcanoes*. San Diego, Academic Press.
- Vallance JW 1999. Postglacial lahars and potential hazards in the White Salmon River system on the southwest flank of Mount Adams, Washington. U.S. Geological Survey Bulletin 2161: 1 – 55.
- Vallance JW, Siebert L, Rose WI, Giron J, Banks NG 1995. Edifice collapse and related hazards in Guatemala. *Journal of Volcanology and Geothermal Research* 66: 337 – 355.
- van Wyk de Vries B, Kerle N, Petley D 2000. A sector-collapse forming at Casita Volcano. *Geology* 28: 167 – 170.
- Voight B 2000. Structural stability of andesite volcanoes and lava domes. *Philosophical Transaction of the Royal Society A* 358: 1663 – 1703.
- Voight B, Elsworth D 1997. Failure of volcano slopes. *Géotechnique* 47(1): 1 – 31.
- Voight B, Janda RJ, Glicken H, Douglass PM 1983. Nature and mechanics of the Mount St Helens rockslide-avalanche of 18 May 1980. *Géotechnique* 33: 243 – 273.
- Watters RJ, Delahaut WD 1995. Effect of argillic alteration on rock mass stability. In: Haneberg WC, Anderson SA eds. *Clay and Shale Slope Instability*. Boulder, Colorado, Geological Society of America.

- 
- Watters RJ, Zimbelman DR, Bowman SD, Crowley JK 2000. Rock mass strength assessment and significance to edifice stability, Mount Rainier and Mount Hood, Cascade Range volcanoes. *Pure and Applied Geophysics* 157: 957 – 976.
- Wilson CJN, Houghton BF, McWilliams MO, Lanphere MA, Weaver SD, Briggs RM 1995. Volcanic and structural evolution of Taupo Volcanic Zone. *Journal of Volcanology and Geothermal Research* 68: 1 – 28.
- Wyllie DC, Mah CW 2004. *Rock slope engineering* 4th Edition. London, Spon Press.
- Zimbelman DR, Watters RJ, Bowman SD, Firth C 2003. Quantifying hazard and risk assessments at active volcanoes. *EOS, Transactions, American Geophysical Union* 84(23): 213 – 217.
- Zimbelman DR, Watters RJ, Firth IR, Breit GN, Carrasco-Nunez G 2004. Stratovolcano stability assessment methods and results from Citlaltepctl, Mexico. *Bulletin of Volcanology* 66(1): 66 – 79.